Lawrence Berkeley National Laboratory
Recent Work

Title
Intermediate-Scale Hydraulic Fracturing in a Deep Mine - kISMET Project Summary 2016: kISMET Project Summary 2016

Permalink
https://escholarship.org/uc/item/01n8b7tf

Authors
OLDENBURG, C.M.
DOBSON, P.F.
WU, Y.
et al.

Publication Date
2016-11-04

Intermediate-Scale Hydraulic Fracturing in a Deep Mine

kISMET Project Summary 2016

OLDENBURG, C.M.[1], DOBSON, P.F.[1], WU, Y.[1], COOK, P.J.[1], KNEAFSEY, T.J.[1], NAKAGAWA, S.[1], ULRICH, C.[1], SILER, D.L.[1][†], GUGLIELMI, Y.[1], AJO-FRANKLIN, J.[1], RUTQVIST, J.[1], DALEY, T.M.[1], BIRKHOLZER, J.T.[1], WANG, H.F.[2], LORD, N.E.[2], HAIMSON, B.C.[3], SONE, H.[3], VIGILANTE, P.[3], ROGGENTHEN, W.M.[4], DOE, T.W.[5], LEE, M.Y.[6], INGRAHAM, M.[6], HUANG, H.[7], MATTSON, E.D.[7], ZHOU, J.[7], JOHNSON, T.J.[8], ZOBACK, M.D.[9], MORRIS, J.P.[10], WHITE, J.A.[11], JOHNSON, P.A.[12], COBLENTZ, D.DD.[13], and HEISE, J.[14]

[1]Energy Geosciences Division, Lawrence Berkeley National Laboratory
[2]Department of Geoscience, University of Wisconsin-Madison
[3]Geological Engineering, University of Wisconsin
[4]Geology and Geological Engineering, South Dakota School of Mines & Technology
[5]FracMan Technology Group, Golder Associattes Inc.
[6]Sandia National Laboratories
[7]Idaho National Laboratory
[8]Energy and Environment Directorate, Pacific Northwest National Laboratory
[9]School of Earth, Energy, and Environmental Sciences, Stanford University
[10]Atmospheric, Earth, and Energy Division, Lawrence Livermore National Laboratory
[11]Lawrence Livermore National Laboratory
[12]EES-17, Geophysics Group, Los Alamos National Laboratory
[13]Earth and Environmental Sciences Division, Los Alamos National Laboratory
[14]Sanford Underground Research Facility

[†] Now at U.S. Geological Survey, Menlo Park, CA

DISCLAIMER

This document was prepared as an account of work sponsored by the United States Government. While this document is believed to contain correct information, neither the United States Government nor any agency thereof, nor The Regents of the University of California, nor any of their employees, makes any warranty, express or implied, or assumes any legal responsibility for the accuracy, completeness, or usefulness of any information, apparatus, product, or process disclosed, or represents that its use would not infringe privately owned rights. Reference herein to any specific commercial product, process, or service by its trade name, trademark, manufacturer, or otherwise, does not necessarily constitute or imply its endorsement, recommendation, or favoring by the United States Government or any agency thereof, or The Regents of the University of California. The views and opinions of authors expressed herein do not necessarily state or reflect those of the United States Government or any agency thereof or The Regents of the University of California.

ABSTRACT

In support of the U.S. DOE SubTER Crosscut initiative, we established a field test facility in a deep mine and designed and carried out in situ hydraulic fracturing experiments in the crystalline rock at the site to characterize the stress field, understand the effects of rock fabric on fracturing, and gain experience in monitoring using geophysical methods. The project also included pre- and post-fracturing simulation and analysis, laboratory measurements and experiments, and an extended analysis of the local stress state using previously collected data. Some of these activities are still ongoing. The kISMET (permeability (k) and Induced Seismicity Management for Energy Technologies) experiments meet objectives in SubTER's "stress" pillar and the "new subsurface signals" pillar. The kISMET site was established in the West Access Drift of the Sanford Underground Research Facility (SURF) 4850 ft (1478 m) below ground (on the 4850L) in phyllite of the Precambrian Poorman Formation. We drilled and cored five near-vertical boreholes in a line on 3 m (10 ft) spacing, deviating the two outermost boreholes slightly to create a five-spot pattern around the test borehole centered in the test volume 40 m below the drift invert (floor) at a total depth of ~1518 m (4980 ft). Laboratory measurements of core from the center test borehole showed P-wave velocity heterogeneity along each core indicating strong, fine-scale (~1 cm or smaller) changes in the mechanical properties of the rock. The load-displacement record on the core suggests that the elastic stiffness is anisotropic. Tensile strength ranges between 3–7.5 MPa and 5–12 MPa. Permeability measurements are planned, as are two types of laboratory-scale hydraulic fracturing experiments to investigate the importance of rock fabric (anisotropy and heterogeneity) on near-borehole hydraulic fracture generation. Pre-fracturing numerical simulations with INL's FALCON discrete element code predicted a fracture radius of 1.2 m for a corresponding injection volume of 1.2 L for the planned fractures, and negligible microseismicity. Field measurements of the stress field by hydraulic fracturing showed that the minimum horizontal stress at the kISMET site averages 21.7 MPa (3146 psi) trending approximately N-S (356 degrees azimuth) and plunging slightly NNW at 12°. The vertical and horizontal maximum stress are similar in magnitude at 42-44 MPa (6090-6380 psi) for the depths of testing which averaged approximately 1530 m (5030 ft). Hydraulic fractures were remarkably uniform suggesting core-scale and larger rock fabric did not play a role in controlling fracture orientation. Electrical resistivity tomography (ERT) and continuous active source seismic monitoring (CASSM) were carried out in the four monitoring boreholes during the generation of a larger fracture (so-called stimulation test) at a depth of 40 m below the invert. ERT was not able to detect the fracture created, nor did accelerometers placed in the West Access Drift, but microseismicity was detected for the first (deepest) hydraulic-fracturing stress measurement. The CASSM data have not yet been analyzed. Analytical solutions suggest that the fracture radius of the large fracture (stimulation test) was more than 6 m (20 ft), depending on the unknown amount of leak-off. The kISMET results for the stress state are consistent with large-scale mid-continent estimates of stress. Currently we are using the orientation of the stress field we determined to interpret a large number of borehole breakouts recorded in nearby boreholes at SURF to generate a more complete picture of the stress field and its variations at SURF. The efforts on the project have prompted recommendations for a host of additional follow-on studies that can be carried out at the kISMET site.

This page left intentionally blank.

EXECUTIVE SUMMARY

Introduction

Control of subsurface fluid flow requires engineering of subsurface permeability, which in turn relies on the ability to create and design fractures of desired size, aperture, orientation, and connectivity. The design and execution of effective fracture creation and fracture stimulation for enhanced geothermal systems (EGS) depend on knowledge of key properties such as stress state, rock structure and fabric, existing fractures, and permeability. The difficulty of characterizing these properties before and after stimulation in the deep subsurface results in incomplete knowledge of the effects of active fracturing and stimulation, thereby preventing development of advanced adaptive control of fractures for permeability management, a major goal of the U.S. DOE SubTER Crosscut initiative. Similarly, remote monitoring of microseismicity associated with fracturing and stimulation can result in uncertain event locations and low-resolution mapping of fracturing processes. Deep mine environments offer the possibility of detailed characterization and proximal monitoring of intermediate-scale hydraulic fracturing and fracture stimulation, which in turn provide high-resolution data sets for improved understanding of stimulation and related modeling and simulation developments and testing.

In order to address the challenges of subsurface energy-related processes involving fractures, fracturing, and permeability enhancement, earth scientists from several national laboratories and three universities have carried out a $1.35M project to develop a new underground facility called kISMET (permeability ($\underline{k}$) and $\underline{I}$nduced $\underline{S}$eismicity $\underline{M}$anagement for $\underline{E}$nergy $\underline{T}$echnologies) 4850 ft (1478 m) below ground at the Sanford Underground Research Facility (SURF) in Lead, South Dakota. The purpose of the new facility is to provide a test site for research on stress characterization, permeability enhancement, and induced seismicity in crystalline rock. Rocks at SURF comprise a sequence of intensely folded Precambrian metamorphic schists, phyllites, and amphibolites cut by a number of Tertiary rhyolite dikes. The kISMET experiments meet objectives in SubTER's "stress" pillar and in the "new subsurface signals" pillar through the testing of monitoring of fracturing by active seismic, electrical resistivity tomography (ERT), and passive microseismic approaches.

Following careful site selection in the spring of 2015 based on satisfying multiple practical and scientific criteria, we designed a borehole array for the selected site and contracted with First Drilling to drill and core five approximately vertical boreholes on 3 m (10 ft) spacing, one center borehole 100 m (328 ft) deep, and four surrounding boreholes 50 m (164 ft) deep. The four monitoring boreholes were instrumented with active seismic and electrical resistivity monitoring equipment, and accelerometers were placed in the 4850L drift for measuring induced microseismicity.

In mid-2016, we carried out predictive hydrogeomechanical modeling and simulation of fracture generation and energy release to aid in the design of the field experiments. Starting in August 2016, we carried out hydraulic fracturing-based stress measurements and stimulation that determined the stress field. In parallel, laboratory studies on core from the boreholes were initiated to measure key rock properties. Following the field testing, analytical solutions were applied using field data to estimate the sizes of fractures generated. Work is ongoing in the areas of laboratory measurements and experiments, and in analyzing previously collected data that can be used to estimate stress at the SURF site. This report summarizes the activities and findings of the kISMET project as of October 31, 2016.

Site-Selection and Site Infrastructure

Several criteria were used to locate the kISMET site, among which were preference for a single lithology and simple structure to avoid excessive heterogeneity and complexity, availability of key services such as ventilation, power, internet, and sufficient room for drilling and testing activities without impeding access in the drift for SURF operations. We also required a site at sufficient depth (thickness of overburden) to provide stress conditions representative of deep EGS sites, and we wanted to avoid local stress perturbations caused by drifts immediately above, below, or astride the site. On two scouting trips to SURF, we inspected several sites. One site stood out for its meeting all of the key criteria. The chosen kISMET site is in the West Access Drift on the 4850L in Poorman Formation phyllite in an area of double-rail track (extra wide drift) with no other drifts nearby.

We designed a five-borehole array consisting of four monitoring boreholes surrounding a central injection borehole in which stress measurements and stimulation would be carried out. A vertical orientation for the test borehole was chosen so it would align approximately with the σ_l principal stress direction which at this depth, 4850 ft (~1478 m), is approximately vertical due to overburden stress. In order to be drilled within the confines of the West Access Drift, we developed a drilling design in which the five boreholes are aligned in the drift with the outer-most boreholes drilled slightly deviated such that the four monitoring boreholes and central test borehole would form a five-spot configuration around a stimulation test volume at a completion depth of 50 m (164 ft). We decided to drill the central experimental borehole even deeper (100 m, or 328 ft) in order to provide space at depth to conduct the first stress measurements and test the equipment, thus reserving the shallower parts of the borehole to conduct the monitored fracturing experiments including the extended fracture test, also called the stimulation test. Borehole spacing was chosen on the basis of the desire for proximal monitoring of the initiation and growth of the hydraulic fractures, while not having the boreholes so close that the fractures would grow far beyond the monitoring boreholes of the test volume. The final decision was on borehole diameter with considerations including size of cores to be collected, flexibility in deploying existing monitoring and fracturing equipment rather than buying all new equipment, and ease of controlling the drilling in this foliated phyllite. Our final design called for four HQ (dia. = 3.78 inches, 96 mm) monitoring boreholes 50 m (164 ft) deep on 3 m (9.8 ft) spacing, and a central NQ (dia. = 2.98 inches, 75.7 mm) borehole, which was drilled to 100 m (328 ft) depth to provide extra test length for stress measurements and equipment shakedown. Bids from three drilling contractors were received and we selected First Drilling based on a combination of positive factors including cost, experienced drilling crew, and good recommendations.

A subcontract to SURF was established to install rock bolts and safety mesh, electrical power, internet, sump, fresh water supply, and access to a water disposal line, along with escort and logistical support for equipment transport from surface to the kISMET site. Approximately eight weeks were spent in preparing and approving documentation for safety, work procedures, and contracting. During this time, design, procurement, and testing of the fracturing and monitoring equipment were carried out. The First Drilling crew began mobilizing at Lead, SD, on June 13, 2016, and finished drilling and coring the final borehole on July 20, 2016. During drilling, intermediate gyro surveys were made to monitor the orientation of the boreholes, and a final survey was made at the bottom-hole locations at the end of drilling. There was 100% recovery of core, which consisted of banded and often tightly folded phyllite of the Poorman Formation. Only one small open fracture was observed during drilling. Each section of core was described and photographed at the site, and then stored in core boxes, which were transported to the surface for storage at the SURF core repository.

Borehole deviation was measured twice after drilling and coring were completed, once using a dedicated borehole deviation tool, and a second time using the integrated deviation sensors on the optical televiewer. The magnetic deviation data showed a maximum of ~6.5 m (21.3 ft) *XY* deviation relative to surface locations for the two outermost deviated boreholes (kISMET-001 and kISMET-005). The two inner vertical monitoring boreholes were shown to deviate less than 0.8 m (2.6 ft) from vertical. While the bottom of the central test borehole (kISMET-003) deviated roughly 6 m (19.7 ft) from vertical at 100 m

depth, the top 50 m of the borehole deviated only ~2 m (6.6 ft) from the vertical direction, creating a nominal five-spot pattern around the test volume at 50 m. Given the conditions, First Drilling did an excellent job in meeting our design for a five-spot pattern at 50 m depth in this challenging rock. After the field hydraulic fracturing and monitoring activities in August and September 2016, the boreholes were capped and covered with enclosures that can be walked on and driven over. Re-use of the kISMET site and its borehole array for geoscience studies is possible as-is. With additional cost for drilling out a stuck impression packer at 72 m (236 ft) depth in kISMET-003, the full length of the 100 m (328 ft) deep test borehole could be made available.

Laboratory Rock Core Studies

Laboratory core studies are aiming (1) to characterize the mechanical and hydrological properties of the rock (phyllite of the Poorman Formation) and (2) to examine the impact of the rock fabric and in situ stress anisotropy on hydraulic fracturing. The rock samples used in the laboratory experiments were obtained from core from the central test borehole, kISMET-003. For baseline rock property characterization tests, we used X-ray CT imaging and ultrasonic velocity measurements, followed by measurements of tensile strength and flow permeability. CT scans of core show well-developed laminations that are tightly folded; heterogeneity in rock fabric occurs even at the centimeter scale.

P-wave velocity was measured using a pair of narrow-band immersion transducers for a range of orientations and locations along the cores. For each core, the reference orientation was determined from the texture (foliation) on the surface of the cores. Cores exhibited very strong velocity anisotropy (as much as 15%) and a well-defined peak orientation, possibly resulting from rock foliation. Velocity changes (heterogeneity) along each core indicate strong, fine-scale (~1 cm or smaller) changes in the mechanical properties of the rock, possibly due to the well-developed foliation.

Using short disc-shaped samples of the core (dia. = 25.4 mm, thickness= ~10–13 mm), Brazilian disc tests were conducted. The objective of these measurements is to understand the impact of the foliation plane on the tensile strength, crack formation, and crack propagation behavior in the rock. The sample plugs have their plug-cylinder axis parallel to the foliation. The load-displacement record suggests that the elastic stiffness is anisotropic, especially in samples from core where the rock appears stiffest when loaded parallel to the foliation, consistent with the velocity measurements. Tensile strength is also strongly anisotropic for sample types where the rock is easier to split when loaded parallel to the foliation. Tensile strength ranges between 3–7.5 MPa and 5–12 MPa. The foliation, mostly defined by the alignment of phyllosilicate minerals, serves as a weak plane and seems to have influenced the fracture path of samples loaded diagonally relative to the foliation. Samples are planned to be scanned by X-ray CT imaging in order to characterize the morphology of the fractures created in these tests.

Despite the lack of open fractures and very low-permeability nature of Poorman phyllite at the kISMET site, leak-off of injected water into the rock matrix from induced fractures can potentially affect hydraulic fracture propagation. Therefore, we will be measuring permeability, including potential anisotropy of permeability, of the rock matrix as an important control on hydraulic fracturing. We will be using a special experimental setup at LBNL built for very tight, low-permeability rock involving a gas-pressure decay permeameter.

Two types of laboratory-scale hydraulic fracturing experiments are under way to investigate the importance of rock fabric (anisotropy and heterogeneity) on near-borehole hydraulic fracture generation. The first experiment will be conducted using bi-axially confined cylindrical rock cores at the University of Wisconsin-Madison. The objective of this experiment is to examine the effect of the rock fabric alone on fracture generation. Thick-wall cylinder fracturing tests will be performed in a conventional triaxial apparatus on 50–75 mm lengths of the core from the stimulation test zone with small boreholes of 1/8–3/8 inch (3.175–9.525 mm) diameter drilled parallel to the core axis for fluid injection. The samples will be subjected to a biaxial stress state with an isotropic stress comparable to kISMET in situ stress magnitudes.

Water will be injected at a constant flow rate to observe the breakdown pressure. Post-experiment samples will be observed either by X-ray CT or by slicing the samples in order to document the fracture geometry and to address the possibility that the foliation has affected the fracture geometry and/or the breakdown pressure. Differential stress magnitude, flow rate, and injected fluid viscosity are potential parameters that will be varied in the tests to help identify possible scale effects and aid comparison with field data.

The second experiment will be conducted at LBNL using cube-shaped samples subjected to triaxial stresses (principal stresses) that are close to the estimated in situ stresses. The objective of this experiment is to examine how the combined effect of rock fabric and stress anisotropy alters the hydraulic fracture generation compared to the fabric effect alone. Small-scale hydraulic fracturing experiments will be conducted using 1.5-inch (38.1 mm) cubes cut out of the NQ cores used in the X-ray CT imaging and ultrasonic velocity measurements. The experiments will use LBNL's true-triaxial loading frame including acoustic emission measurement capability. During the experiment, estimated anisotropic in situ stresses will be applied to a rock cube, which is cut so that the rock fabric is oriented in the desired direction with respect to the principal stress axes. Subsequently, fluid will be injected in a small-diameter (~1/8 inch diameter (3.175 mm)) analogue borehole to induce a hydraulic fracture. The injection pressure will be adjusted to determine the fracture re-opening pressure, which will be correlated to the applied minimum horizontal (around the borehole) stress in the experiment. After the experiment, the orientation and geometry of the induced hydraulic fracture will be examined either non-destructively using X-ray CT and/or ultrasonic waves, or destructively by slicing the rock cube. Results of ongoing and future laboratory experiments will be reported in conference proceedings and possibly journal articles.

Pre-Test Modeling and Analysis

An important part of the kISMET experimental design was the determination of the injection parameters (duration of injection at given flow rate) to produce hydraulic fractures with desired size ranges. A second objective of design calculations was to provide an initial conservative estimate of the magnitudes of potential seismicity induced by the hydraulic fracturing experiments under various injection scenarios. We used INL's FALCON coupled network flow and quasi-static discrete element model (DEM) to predict fracture size, breakdown pressure, fracture re-opening pressure, and energy released by fracturing. In the DEM method, the rock volume is represented by an assemblage of randomly generated, non-uniform-sized elements referred to as particles. The DEM lattice of particles is used to simulate mechanical deformation and fracture propagation. Each edge of the tetrahedra defining the lattice represents an elastic beam connecting two adjacent DEM particles. In a quasi-static DEM model with a mechanical load applied, particles will move and rotate into a new mechanical equilibrium via a numerical relaxation procedure. The elastic beams between two particles can be deformed and sustain increasing stretching and shearing forces. Once the shearing and stretching forces of a beam exceed some pre-defined threshold, that beam will break, mimicking a crack initiation, and the stress will be transmitted into neighboring beams which are likely to break sequentially, mimicking crack propagation. During each time step, this beam-breaking relaxation process is repeated a number of times until no more beams break at the given loading level. The hydraulic fracture propagation is treated here as a quasi-static process for computational efficiency. In order to account for the local mechanical heterogeneities due to variations of mineral fabrics, random perturbations can be added to the tensile strength, shear strength, and stiffness constant of individual beams. It turns out that the randomness of the beam mechanical strengths, together with the "disordered" DEM lattice, are critical for generating realistic fracture geometry and fracture patterns.

The Force-Displacement law is used to determine both the translational and rotational motion of each particle and the contact forces after particle displacement. Once a mechanical load is applied by the injection of fluid, an over-relaxation algorithm is used to relax the DEM network to a new state of mechanical equilibrium. If a beam reaches the failure criterion, it will be irreversibly removed from the

DEM network. In order to couple fluid flow with the DEM model while appropriately accounting for pressure dissipation due to flow along fractures and into the matrix due to leak-off, a conjugate flow lattice is constructed. Without any measurements of kISMET-specific rock properties (but using representative rock property values determined from previous geotechnical studies conducted at SURF), we estimated reasonable values for Young's modulus, Poisson's ratio, and tensile strength and ran a sample problem that behaved like a linear elastic solid before the load reached its peak failure value and failed suddenly. This simulated brittle behavior, typical for crystalline rocks, provided enough confidence for proceeding with design calculations. In future work, we plan to more formally calibrate the model using laboratory core test data.

In the design calculations, we used 118,634 DEM particles of variable sizes all randomly generated and packed into the model domain to form the DEM lattice and associated conjugate flow network. With overburden stress ($\sigma_{vertical}$) oriented in the Z-direction, we placed an open vertical borehole in the domain into which fluid is injected at 2 L/min (lpm). The permeability of the rock is set to 10 nanoDarcy (1.0×10^{-20} m^2), representing an ultralow-permeability formation. As the fluid injection starts, the pressure in the wellbore builds up (at ~35 seconds after injection starts, or equivalently, after ~1.17 L of injection have occurred) and becomes large enough to break the beams between DEM particles adjacent to the wellbore. This pressure is the breakdown pressure, which causes a nearly vertical fracture to propagate with a stable, reduced pressure called the propagation pressure. One important observation is that once the fracture starts to initiate, it will open up a crack with a relatively large radius initially, ~1.2 m, with an average aperture of ~2.0×10^{-4} m, similar to the values predicted by the analytical calculations presented in Chapter 7. Due to the local mechanical heterogeneity incorporated into the model, the initial crack does not assume an ideal bi-wing or penny shape, but rather it exhibits asymmetry. As more fluid is injected, the crack continues to propagate more or less along the horizontal maximum compressive stress direction (Y-axis in the simulation) and eventually grows into an approximate penny shape.

Addressing concerns of SURF management and physics experimentalists about induced seismicity, we used the results of the DEM numerical simulations to provide an estimate of the energy released during fracturing. Assuming each beam breakage is a single seismic event, and that all elastic strain energy stored in the beams prior to breaking is used in generating earthquakes, the DEM model provides a conservative estimate of the potential seismic magnitude. The largest energy release happens in the model at the initial fracture-opening stage, which has the most beam-breakage events. The total energy released during the 345 seconds of injection is 0.37 MJ, and the average released energy of each event is 96.9 J. This corresponds to events with magnitude of ~ -4 (too small to be any concern in terms of induced seismicity).

As an interesting potential confirmation that the FALCON coupled DEM network-flow model mimics important physics of hydraulic fracturing, we note that the simulated magnitude-frequency curve follows a power-law scaling behavior similar to the Gutenberg-Richter relation.

Stress Measurement and Stimulation

The main purpose of the kISMET project was to carry out hydraulic fracturing experiments at depths of approximately 5000 ft (1524 m) for determining the in situ stress field, for testing the creation of a larger fracture (stimulation), and for observing the effects of rock fabric on fracturing while monitoring the process using various geophysical approaches. Motivation for new measurements of the stress field at SURF arose from a long history of highly variable stress measurements, for which the source of variability was not well known and could be due to rock heterogeneity, anisotropy, or shortcomings of measurement techniques. In order to meet the SubTER goal of developing approaches to control fracturing at depth, further understanding of the effects of rock fabric, the stress field, and hydraulic fracturing processes is needed.

Characterization of the stress field at SURF began in the 1970's, when the site was an active gold mine, and continued ever since for satisfying the stress characterization needs for new mining excavations, and later for DUSEL and SURF cavern designs. A compilation of measurements with wide scatter was regressed to derive approximate equations for σ_v, σ_{HMax}, and σ_{Hmin} as a linear function of depth. The ratio of maximum-horizontal-to-vertical stress is between 0.6 and 0.9 and the ratio of minimum horizontal stress to vertical stress is between 0.36 and 0.6. More recent measurements provided stress values that ranged from close to 62 MPa (9000 psi) to 24 MPa (3500 psi) for the largest and smallest stresses, respectively, and were highly variable in both direction and magnitude depending on location and rock type at SURF.

Hydraulic fracturing has become a standard method for determining the in situ state of stress in rock masses for use in engineering design, and is one of the few methods available for testing in deep boreholes (Haimson, 1978). Although numerous past measurements of in situ stress have been made at SURF over the years, the present measurements are the first to be performed using hydraulic fracturing. The technology we used at kISMET utilizes a fast and continuous tool-tripping wireline hydraulic fracturing system for in situ stress measurements and fracture stimulation. The wireline hydraulic fracturing system consists of two major downhole tool assemblies: (1) a straddle packer assembly for fracture initiation and propagation (stimulation) within the selected test zone; and (2) an impression packer orienting tool assembly for fracture delineation. (We also retained the option of using acoustic televiewer logging for fracture delineation). In order to run hydraulic fracturing tests, hydraulic fluid pressure is generated by two pneumatic pumps (one for the packers and the other for the test zone between the packers). A flow meter is also employed to monitor the flow of water into (and out of) the test zone during (de) pressurization. The flow rate of the injection fluid into the fracturing test zone is monitored by a turbine flowmeter connected between the surface pump and the high-pressure tubing leading to the test zone. The packer and test-zone pressures as well as the flow rate are recorded simultaneously on a portable computer at 10 samples/s to allow statistical analysis for determining shut-in and fracture reopening pressures.

To perform a hydraulic fracturing stress measurement, a section of a borehole is hydraulically isolated using the flow rate-straddle packer assembly while fracturing fluid (water) is pumped at a low flowrate into the packed-off interval, gradually raising the pressure on the borehole wall until a fracture is initiated in the rock, indicated by a drop of the fluid pressure. Pumping is stopped allowing the test interval pressure to decay. Several minutes into the shut-in phase, the pressure is released and allowed to return to ambient conditions. The pressure cycle is repeated three times maintaining a similar flowrate. The key measures of breakdown, re-opening, and shut-in pressures are picked from the pressure–time record and used in the computation of the in situ stress.

The testing program was planned to include five hydraulic fracturing stress measurements at depths between 60 and 100 m (197 and 328 ft) in the central borehole kISMET-003. After testing in seven zones, the access to the borehole below approximately 72 m (236 ft) was lost due to a stuck impression packer, preventing characterization of fracture orientations for Tests 1 through 6. In order to make complete stress measurements in five intervals as planned, we turned focus to intervals above 72 m (236 ft) in depth including the stimulation test zone at 40.2 m (1518.6 m below ground surface), and turned to borehole televiewer logging as the way to delineate fracture orientations.

The stimulation test involved keeping the generated fracture open and propagating during a period of constant pressure and low flow rate. Following initiation of the hydraulic fracture as indicated by breakdown at 22.7 MPa (3291 psi), five stimulation cycles were conducted. The first two cycles were conducted with a relatively low flow rate of 0.48 lpm, while the next three cycles used a relatively high flowrate of 0.63 lpm. For each cycle, the steady-state pressures were achieved at 20.1-20.3 MPa (2914-2943 psi) and maintained for approximately 15 minutes in order to finish one round of ERT data acquisition; continuous active source seismic monitoring (CASSM) acquisition takes only ~20 sec.

The acoustic borehole televiewer (BHTV) was the backup strategy to the impression packer to delineate and orient hydraulic fractures. The BHTV was very successful compared with optical televiewer attempts, which could not distinguish the dark fractures from the surrounding dark rock. Pre- and post-test BHTV runs provided excellent images of the fractures we generated.

Test data quality was excellent with well-defined breakdown pressures and clear shut-in pressure signatures. The minimum horizontal stress (σ_{HMin}) values range from 20.0 to 24.1 MPa, averaging 21.7 MPa (3146 psi), approximately 51% of lithostatic stress. The values have a high level of consistency that is typical for hydraulic fracturing stress measurements in low-permeability, relatively uniform rock.

Maximum horizontal stress (σ_{HMax}) can be estimated if rock tensile strength is known, measurements of which are ongoing in the lab. Maximum horizontal stress can also be estimated from the difference between the breakdown pressure P_b achieved in the first pressure cycle, and the fracture reopening pressure P_r recorded in the second pressure cycle. The maximum horizontal stress values estimated in this way range from 38.7 to 48.2 MPa with an average of 44.1 MPa (6394 psi), close to the lithostatic stress. While there is uncertainty in this estimate of σ_{HMax}, it appears that at this depth, the vertical stress and maximum horizontal stresses are similar in magnitude which may be indicative of the cross-over from a tendency for strike-slip faulting at shallow crustal depths to a tendency for normal faulting at greater depth.

As for the stress directions, fractures created by hydraulic fracturing in homogeneous rock should align with the direction of the maximum horizontal stress (σ_{HMax}). We obtained fracture orientation information from the acoustic televiewer log. The analysis of the acoustic televiewer logs involved digitizing the fracture traces and importing them to an Excel spreadsheet, where they were fitted to sinusoidal traces of known orientation. The traces were all corrected for magnetic declination and represent orientations relative to true North. The quality and consistency of the fracture orientations mirror that of the shut-in pressures from the hydraulic fracturing. Overall the data set provides an excellent indicator of the minimum horizontal stress (σ_{HMin}) direction with a 356° trend and 12° plunge indicating fractures that are striking N86°E with a dip of 78° to the southeast. The fact that the fractures are not following foliation but have a non-vertical, though very steep, dip indicates that the principal stress may be inclined slightly off vertical. The uniformity of results across tens of meters of depth in the test borehole suggests that stress rather than rock fabric is controlling hydraulic fracture orientations.

Reviews of midcontinent stress measurements suggest a relatively uniform compressive stress field with a maximum horizontal stress (σ_H) oriented NE to ENE. Our measurements at kISMET are consistent with this general direction of the regional horizontal principal stresses (σ_H trending NE to ENE). The kISMET determination of average principal stress magnitudes of $\sigma_{Hmax} \approx \sigma_v \approx 2\sigma_{Hmin}$ is also in accord with the regional conditions.

Geophysical Monitoring and Analysis

Borehole logging and geophysical monitoring were conducted before, during, and after hydraulic fracturing stress testing and stimulation at kISMET to assess fracture geometry and the potential use of geophysical methods for near-real time monitoring of fracture generation and propagation. Mt. Sopris borehole acoustic televiewer, optical televiewer, and full waveform sonic logging were conducted focusing on the NQ (center) borehole. Electrical resistivity tomography (ERT) and continuous active source seismic monitoring (CASSM) were conducted in the monitoring wells (kISMET-001, -002, -004, and -005, aka K1, K2, K4, and K5) during the extended stimulation tests at ~40.2 m depth (132 ft) in the center borehole. Passive seismic micro-earthquake (MEQ) monitoring was conducted during all of the stress test and stimulation activities.

Crosswell ERT surveys were conducted to provide information concerning the geologic structure, fabric, and heterogeneity of the host rock, and to assess the capability of ERT to image the fracturing in near-real

time. Two electrode cables with electrode spacing of 1.6 m (5.25 ft) were used to collect crosswell imaging data separately between different well pairs across the kISMET test volume. With electrodes deployed in the K2-K4 well pair, crosswell ERT data sets were collected before and after stimulation operations using a survey configuration designed to optimize both spatial and temporal imaging resolution. With electrodes deployed in the K1-K5 well pair, additional crosswell ERT data sets were collected before, during, and after stimulation operations.

Baseline pre-stimulation data were inverted simultaneously in 3D including explicit modeling of boreholes in true dimension and with deviations, along with explicit modeling of borehole fluid conductivity. The baseline images revealed steeply dipping electrical conductivity variations consistent with the host rock structure and mineralogy at the site.

We used a computational mesh for ERT data inversion that accounted for borehole geometry variations. Within the boreholes, the starting model for the inversion was set to the assumed borehole-fluid conductivity, but this starting model fluid conductivity was allowed to be modified by the inversion subject to being smoothly varying within the borehole. Fluid conductivities were allowed to vary because water samples collected from each well and analyzed after the stimulation revealed significantly different fluid conductivity between wells (~500 to > 1000 µS/cm).

Time-lapse images from both the K1-K5 and K2-K4 planes were not able to distinguish the induced fracture, likely due to the combined effects of a relatively small fracture zone, changes in borehole fluid conductivity during the imaging campaign, and the geometry of the imaging planes with respect to the fracture zone.

ERT surveys have the potential to provide near-real time images of rock structure. We endeavored to test this possibility by sending collected data directly from the kISMET site via SURF's fast underground internet to PNNL where the data were inverted. With a 10-minute collection time and similar time for inversion at PNNL, the roundtrip collection-to-image time was around 20 minutes. We did not have time in the field to refine this workflow to demonstrate near-real time ERT, but this will be a priority in future ERT deployments. Measures that can be taken in the future to significantly improve fidelity of the ERT data include installation of electrodes on the outside of a PVC casing that is grouted into the monitoring boreholes in order to isolate CASSM from ERT while still allowing both approaches to be used simultaneously in one borehole.

Passive seismic monitoring using accelerometers located on concrete footings in the 4850L drift recorded continuously during hydraulic fracturing activities. Only the deepest hydraulic fracturing tests produced usable signals above background noise. For this test, the accelerometer recorded the breakdown event and subsequent fracture re-openings. Shallower hydraulic fracturing events did not produce signals discernable above the considerable noise of the pumps at the kISMET site. Future use of passive seismic monitoring should use borehole-based accelerometers to minimize noise from equipment in the drift.

CASSM data were also collected during the stimulation test. These data have not yet been processed as of the writing of this report.

Analytical Solutions for Estimating Fracture Size

The kISMET hydraulic fracturing experiments allowed determination of the magnitude and orientation of the minimum and maximum horizontal stresses (magnitude and orientation) at the kISMET site, but did not provide a direct measurement of fracture size. Assuming the penny crack conceptual model is appropriate for the hydraulic fracture generated in the kISMET Experiment 11 (stimulation test), we have used analytical equations along with data on injection flow rates and volumes to estimate fracture size. Using the field data, which showed a total fluid injection volume of 41.8 liters and total bleed-back over five cycles of -13.8 liters, the net fluid injection volume is 28.1 liters. Assuming no leak-off (zero rock permeability), all of the water goes into fracture creation, i.e., the fluid volume that is creating the

fractures is the net volume of injected water minus the bleed back. The analytical equations for this case suggest that the fracture expanded to a radius of 7.9 m (26 ft) through stimulation Cycles 2 to 6, with relatively small radial growth in the last cycle. The equation estimates that fracture aperture values grew from 4.3×10^{-5} m to 8.5×10^{-5} m (0.043 – 0.085 mm).

In order to estimate fracture size in the case on non-zero rock permeability, i.e., with leak-off, we considered bounding calculations that exploit two key assumptions. First, we assume that all fluid that was not recovered by the bleed-off disappeared as leak-off into the rock. Second, we assume that the fracture was created instantaneously and that leak-off volume permeated the rock over the full-size fracture-matrix interface. For the first assumption, we assume that the bleed-off volumes for each cycle represent the fluid that created fracture growth, the rest having been lost to matrix leak-off. Under this assumption, the estimated radius varies from 1.4 m (4.6 ft) in the initial stimulation to 5.7 m (18.7 ft) at the end of Cycle 6. These radius values are approximately 70% of those for the impermeable case, while the fracture surface areas are approximately 50% of the impermeable case.

The assumption that the water not recovered in bleed-off flowed into the rock as leak-off can be tested using a simple linear diffusion model of flow from the fracture to the rock assuming a constant fracture-matrix interfacial area. Assuming a reasonable value of non-zero matrix permeability, we find a close match between field data and the equation estimate for cycle time and fracture radius at around 75 minutes and 6 m (19.7 ft) radius, respectively. This corresponding leak-off estimate is 25.7 liters, which compares closely to the observed fluid loss of 28.1 liters. We caution that this agreement may be fortuitous given the considerable uncertainty in the hydraulic properties of the rock. Nonetheless, the magnitude of the possible leak-off volumes may be a bit surprising given the near-zero porosity and impermeable appearance of the core, but it may also be a good illustration of how a large surface area and injection pressure can offset a low permeability to create significant leak-off from fractures to matrix.

Site-Wide Stress Analysis

The kISMET project results provide a means to leverage the extensive site characterization effort that was carried out as part of the previous Deep Underground Science and Engineering Laboratory (DUSEL) program. In short, the very consistent and first-ever SURF hydraulic fracturing-based minimum horizontal stress measurements we made in the kISMET project provide the basis for the integrated interpretation of previous stress measurements. Previous overcoring methods for determining in situ stress have shortcomings due to the small scale of the strain on which the measurement is based and the variability in rock elastic properties (heterogeneity/anisotropy) assumed to relate stress to strain. Integrating hydraulic fracturing-based methods with borehole-breakout methods, as we are currently doing, overcomes some of these shortcomings and has become the standard for assessing in situ stress in oil and gas reservoirs. Borehole breakouts were logged in many of the sub-horizontal site characterization boreholes that were drilled for the DUSEL program. Two DUSEL boreholes, Boreholes J and D, are particularly relevant to integrated interpretation to complement both site-wide and kISMET-centric stress determination. The integrated analysis and interpretation we are currently undertaking of previous stress measurements is expected to provide a much fuller picture of the stress field and its variability at SURF.

Conclusions and Research Needs

The kISMET team carried out a successful program of drilling and coring, and subsequent hydraulic fracturing for determining the stress field, understanding the effects of rock fabric on fracturing, and gaining experience in monitoring the fracturing process. Laboratory measurements of core show strong effects of anisotropy. Laboratory-based permeability measurements are planned, as are two types of laboratory-scale hydraulic fracturing experiments to investigate the importance of rock fabric (anisotropy and heterogeneity) on near-borehole hydraulic fracture generation under controlled laboratory conditions. Pre-fracturing numerical simulations with INL's FALCON code predicted fracture radius values in good

agreement with analytical estimates, and negligible microseismicity as observed. Field measurements of the stress field by hydraulic fracturing showed that the minimum horizontal stress at the kISMET site averages 21.7 MPa (3146 psi) pointing approximately N-S (356 degrees azimuth) and plunging slightly NNW at 12°. Hydraulic fractures were remarkably uniform suggesting core-scale and larger rock fabric did not play a role in controlling fracture orientation. Monitoring using ERT and CASSM in the four monitoring boreholes, and passive seismic accelerometer-based measurements in the West Access Drift, were carried out during the long fracturing (stimulation) test. ERT was not able to detect the fracture created, while the accelerometers in the drift picked up only the fracturing signal from the first (deepest) hydraulic-fracturing stress measurement. The CASSM data have not been analyzed yet. Analytical solutions suggest fracture radius of the large fracture was more than 6 m (19.7 ft) depending on the unknown amount of leak-off. The kISMET results are consistent with large-scale mid-continent estimates of stress. Currently we are using the orientation of the stress field determined at kISMET to interpret large numbers of borehole breakouts recorded in nearby boreholes at SURF to generate a more complete picture of the stress field and its variations at SURF.

We have identified several follow-on research activities to address needs in the areas of site characterization, additional field tests, modeling refinements, and tests for improving geophysical monitoring.

TABLE OF CONTENTS

LIST OF FIGURES

LIST OF TABLES

ACRONYMS

3C	Three component
A/D	Analog-to-digital
BHTV	Borehole televiewer
CASSM	continuous active source seismic monitoring
DUSEL	Deep Underground Science and Engineering Laboratory
EGS	Enhanced geothermal system(s)
ERT	Electrical resistivity tomography
FWS	Full waveform sonic
GCS	Geologic carbon sequestration
HI	Hollow inclusion
INL	Idaho National Laboratory
ISRM	International Society of Rock Mechanics
kISMET	Permeability (k) and Induced Seismicity Management for Energy Technologies
L	Level, as in 4850L
LANL	Los Alamos National Laboratory
LBNL	Lawrence Berkeley National Laboratory
MSDS	Material safety data sheet(s)
MEQ	Micro-earthquake
MOU	Memorandum of understanding

PPE	Personal protective equipment
P-Q	Pressure-flow rate
SDSMT	South Dakota School of Mines and Technology
SNL	Sandia National Laboratories
SOP	Standard operating procedures
SubTER	Subsurface Technology and Engineering Research
SURF	Sanford Underground Research Facility
TOC	Top-of-casing
U.S. DOE	United States Department of Energy
VCR	Vertical crater retreat

NOMENCLATURE

A	Cross-section area of the elastic beam	m^2
b-value	Slope in Gutenberg-Richter relation (seismic b-value)	
$d_{i,j}^{\,0}$	Initial equilibrium (stress free) distance	m
D	Diameter of cross section in Eq. 3.1	mm
e	Elliptical radius	m
e_{max}	Aperture at the borehole wall	m
E	Young's modulus	GPa
F_{ij}	Force exerted on a node i by a neighboring node j	N
G	Shear modulus	GPa
H	Hydraulic head	m
I	Moment of inertia	kg m^2
k	Formation permeability	m^2
k_n	Normal force constant	N
k_s	Shear force constant	N
K	Hydraulic conductivity of the rock	m s^{-1}
K_{1C}	Fracture toughness	Pa m
M_0	Single moment tensor	N m
M_{ij}	Moment exerted on a node i by a neighboring node j	N m
M_w	Moment magnitude	-
$\vec{n}_{ij}$	Unit normal vector between elements i and j	-
p	Pressure	MPa
P_b	Breakdown pressure	MPa
P_0	Initial pressure	MPa
P_r	Re-opening pressure	MPa
P_{dpdt}	Derivative of shut-in pressure	MPa s^{-1}
P_{isip}	Instantaneous shut-in pressure	MPa
P_{peak}	Peak load in Brazilian test	MPa
p_{Pump}	Pump pressure	MPa
P_r	Reopening pressure	MPa

Q	Mass injection rate in Eq. 4.4	kg m^{-3} s^{-1}
Q	Volumetric flow rate per unit area in Eq. 7.4	m s^{-1}
Q_e	Effective fluid mass injected in Eq. 7.1	kg
r	Radial distance within the fracture	m
R	Total fracture radius	m
$\vec{s}_{i,j}$	Unit vector in shear direction between elements i and j	-
T	Thickness of sample in Eq. 3.1	mm
T	Rock tensile strength	MPa
Vp	P-wave velocity	m s^{-1}
Vs	S-wave velocity	m s^{-1}

Greek symbols

ε_c	Critical tensile strain	-
ζ	Porosity of the porous medium	-
η	Hydraulic diffusivity	m^2 s^{-1}
θ	Angle	degrees
μ	Dynamic viscosity	kg m^{-1} s^{-1}
ν	Poisson's ratio	-
ρ_f	Density of the injected fluid	kg m^{-3}
σ_{HMin}	Minimum horizontal stress	MPa
σ_{HMax}	Maximum horizontal stress	MPa
σ_1	Maximum principal stress	MPa
σ_c	Compressive strength	MPa
σ_T	Tensile strength	MPa
σ_h	Horizontal stress	MPa
σ_v, $\sigma_{vertical}$	Vertical stress	MPa
τ	von Mises failure criterion	-
ϕ_c	Critical rotation angle for beam breakage in Eq. 4.3	radians
ϕ_i	Rotation angle in frame of beam in Eq. 4.1	radians
Φ	Dimensionless variable in Eq. 4.2	-

1.   INTRODUCTION

Lead Authors: Curt Oldenburg and Pat Dobson

1.1   Motivation

The purposeful control of subsurface fluid flow requires engineering of subsurface permeability, which in turn relies on the ability to create and design fractures of desired size, aperture, orientation, and connectivity. For applications such as geothermal energy and oil and gas production, the reservoirs are deep and accessible only by long boreholes (wells). The efficiency of recovery of heat or hydrocarbons from these reservoirs is often assisted by stimulation, for example using hydraulic fracturing to enlarge and extend existing fractures, or to create new fractures to increase fluid flow. The design and execution of effective stimulation depends on knowledge of key properties such as stress state, rock structure and fabric, existing fractures, and permeability. Given the remote nature of the subsurface environment, it is very challenging to characterize these properties before and after stimulation (e.g., Dusseault, 2011). This situation results in incomplete knowledge of the effects of active stimulation as obtained from hydraulic testing and geophysical monitoring, thereby preventing development of advanced adaptive control of fractures for permeability management. Similarly, distant monitoring of microseismicity associated with stimulation can result in uncertain event locations and low-resolution mapping of dynamic fracture-tip propagation and hydroshearing processes. In contrast, deep mine environments offer the possibility of detailed characterization and proximal monitoring of intermediate-scale fracture stimulation, which in turn provides high-resolution data sets for improved understanding of stimulation and related model development and testing.

The response of a reservoir to hydraulic stimulation is dependent on rock properties, stress orientation, and the presence and orientation of preexisting fractures (Fig. 1.1). Fracturing is the key to enhancing permeability for subsurface energy applications in tight formations. For example, in enhanced geothermal systems (EGS), hydraulic fracturing or shearing of existing fractures is used to generate flow paths through which water can be injected and produced for energy extraction. Challenges in EGS include difficulty in estimating stress state, the frequency, magnitude, and temporal and spatial distribution of induced microseismic events, effects of heterogeneous rock properties (e.g., rock fabric and existing fractures), and the resulting low heat recovery due to non-optimal fracture networks (Grant and Garg, 2012). Zang et al. (2014) suggest that for crystalline rocks, tensile crack formation may dominate in the near-field area, while hydroshearing of existing fractures may be the dominant process farther away from the well bore. In oil and gas production, fracturing to enhance permeability in multiple stages along long horizontal wells in organic-rich source rocks can be influenced by rock fabric (e.g., Suarez-Rivera et al., 2013). Production from hydrocarbon wells is often dominated by a few fractures, resulting in poor zonal coverage (Warpinski et al., 2009). Finally, there is a need in many injection- and storage-related applications (e.g., geologic carbon sequestration (GCS), deep disposal of produced water, and compressed air energy storage) for enhancing and controlling permeability to improve injectivity around the well, and to reduce permeability of seals or cap rocks. All of these challenges can be addressed through greater knowledge of how stress state, rock fabric, existing fractures, and fracturing approach interact to affect permeability creation and associated microseismicity.
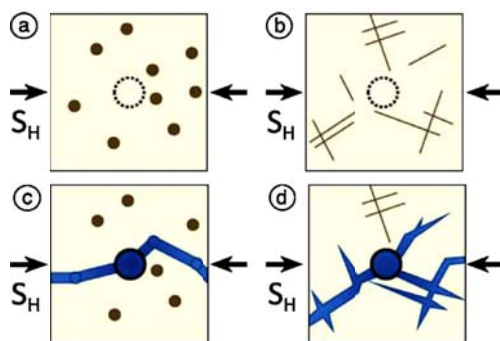
Figure 1.1. Schematic representation of potential response to hydraulic stimulation in geothermal
    reservoirs (Zang et al., 2014). Weaker sedimentary rocks (left column) and stronger crystalline
    rocks (right column) are displayed prior to (upper row) and after (lower row) hydraulic
    stimulation. Arrows indicate orientation of S_{HMax} (σ_{HMax}), and large circles depict location of
    stimulated borehole. Filled circles indicate open pores in sediments and lines indicate
    preexisting fractures. Fluid flow pathways following stimulation are highlighted in blue.

1.2   Overview of the kISMET Project

In order to address the common needs and challenges of subsurface energy-related processes involving
fractures, fracturing, and permeability enhancement, earth scientists from several national laboratories and
three universities have carried out a $1.35M project to develop a new underground facility at the Sanford
Underground Research Facility (SURF) in Lead, South Dakota (Heise, 2015). The purpose of the new
facility is to provide a test site for research on stress characterization, permeability enhancement, and
induced seismicity in crystalline rock. Under the name kISMET (permeability (k) and Induced Seismicity
Management for Energy Technologies), the facility is located on the 4850L of SURF (4850 ft (1478 m)
below ground surface) where numerous existing physics research facilities are currently operating.

The SURF site has been the subject of detailed geologic, hydrologic, and geomechanical studies (e.g.,
Carter et al., 2011; Ebenhack, 2013; Gage et al., 2014; Girard et al., 1997; Harms et al., 2010; Hart et al.,
2014; Murdoch et al., 2012; Roggenthen and Koch, 2013; Wang et al., 2007) that provide valuable
background information for the kISMET field experiments. The geology of the SURF site consists of a
sequence of intensely folded Precambrian metamorphic schists, phyllites, and amphibolites, which have
been cut by a number of Tertiary rhyolite dikes. It is also host to the Homestake gold deposit, which was
the impetus for the underground workings that served the largest gold mine in North America (Caddey et
al., 1991). Hydraulic fracturing of similar rock types in the Black Hills has proved successful in
improving well permeability (Rahn, 1994). EGS sites are known to be located in similar schistose rocks
in which fracture stimulation will be essential to unlock energy recovery potential.

The kISMET project started in 2015 as a SubTER "seedling" project with $250K of funding for site
selection and infrastructure development. The project was advanced to the level of "sapling" in late 2015
and supplemented by $1M in funding, to which $100K was added by Los Alamos National Laboratory
(LANL) for data collection and analysis. Following selection of competent drilling subcontractor and
support for SURF to establish key infrastructure at the kISMET site, we drilled and cored in mid-2016
five approximately vertical boreholes on 3 m (10 ft) spacing, one center borehole 100 m (328 ft) deep,
and four surrounding boreholes 50 m (164 ft) deep. We chose to drill vertical boreholes because the
maximum principal stress at SURF is sub-vertical ($\sigma_1 \approx \sigma_v$) (Wang et al., 2012). From the orientations of
the fractures generated in the vertical center borehole, the direction of the minimum horizontal stress

(σ_{HMin}) can be approximately determined. Two of the surrounding monitoring boreholes were slightly deviated to create a five-spot pattern around a test volume at ~50 m (164 ft) depth. The four monitoring boreholes were instrumented with active geophysical and electrical resistivity monitoring equipment. Accelerometers were placed in the 4850L drift for measuring micro-induced seismicity. In mid-2016, we carried out predictive hydrogeomechanical modeling of the stress field and fracture generation to anticipate fracture behavior and induced microseismicity. Starting in August 2016, we carried out the actual hydraulic fracturing-based stress measurements and stimulation. In parallel, laboratory studies on core from the boreholes were initiated. Following the field tests, analytical solutions were used along with field data to estimate fracture size. Research is ongoing to integrate SURF-wide observations of borehole breakout with kISMET results to extend the understanding of the stress state at SURF.

Results of this project can potentially benefit a wide variety of subsurface energy technologies. The crystalline rock at SURF means that the most direct beneficiary of the project will be geothermal applications (EGS), which often suffer from short-circuiting or low effective hydraulic conductivity, but the effects of rock fabric (e.g., Nasseri et al., 1997; Zang et al., 2014) that we investigated are also relevant to fracturing in marl and shale, of importance to unconventional hydrocarbon reservoirs. Similarly, the fracture propagation monitoring that is enabled by proximal access at the kISMET site yielded general knowledge about effects of stress, rock fabric, existing fracture network, and stimulation approaches on resulting fracture character. On the induced seismicity side, the work may improve understanding of event triggers and wave propagation in fractured anisotropic rock. Finally, microseismic monitoring of fracturing has broad applicability, and knowledge gained in the project about wave propagation in fractured rock may apply to EGS, GCS, and waste-water injection-related induced seismicity. In addition, the kISMET site will provide long-term benefits as an experimental facility for collection of community data sets related to SubTER pillar goals (e.g., JASON Report, 2014).

1.3   Plan of this Report

A variety of tasks was carried out by LBNL, a team comprising Univ. of Wisconsin-Madison, Golder Associates, Stanford University, and Sandia National Laboratories (SNL), hereafter referred to as WGSS, our direct national lab collaborators, and the South Dakota School of Mines and Technology. This report provides a comprehensive summary of kISMET activities in roughly chronological order from site selection, characterization, and drilling and coring (Chapter 2), to laboratory studies on cores collected from kISMET site (Chapter 3), to predictive modeling and analyses that we used to design the stress measurement and stimulation activities (Chapter 4). In Chapter 5, we summarize the hydraulic fracturing-based stress measurement and stimulation field activities and analysis. Chapter 6 provides preliminary analyses of electrical resistivity tomography (ERT), passive micro-seismic monitoring, and borehole continuous active source seismic monitoring (CASSM). We present in Chapter 7 estimates of fracture radius and other characteristics of the kISMET hydraulic fractures using analytical solutions. In Chapter 8, we discuss implications of the measurements for the larger-scale stress field at SURF. Chapter 9 provides a summary of the project accomplishments to date and suggests topics and approaches for future research at the kISMET site.

This page left intentionally blank.

2.   SITE-SELECTION AND SITE INFRASTRUCTURE

Lead Authors: Pat Dobson, Paul Cook, Bill Roggenthen, Drew Siler, Curt Oldenburg, and Jaret Heise

2.1   Site Criteria and Site Selection

The kISMET team discussed project objectives and scope with staff from SURF to identify locations that met the following criteria:

- Appropriate lithology that avoids excessive heterogeneity and lithologic complexity;

- Availability of key services (ventilation, power, water, internet, ground support);

- Space for drilling, for boreholes, and for equipment without interfering with existing SURF infrastructure;

- Sufficiently far away from sensitive physics experiments;

- Absence of drifts within 150 m (492 ft) below the site so that (downward) vertical kISMET boreholes would be far from existing drifts to avoid stress perturbation;

- Minimum cost for site improvements such as drilling boreholes and adding infrastructure;

- Sufficient depth to provide stress conditions representative of deep EGS sites.

Several site-scouting trips were conducted to investigate potential sites at SURF. Our first trip was conducted on Feb. 12, 2015 by Curt Oldenburg, Pat Dobson, and Bill Roggenthen. We were escorted underground by Tom Regan, and we also met with Jaret Heise and David Vardiman above ground in the SURF offices. Three different sites were considered during this visit: two on the 4850L (Fig. 2.1), and one on the 4100L (Fig. 2.2).
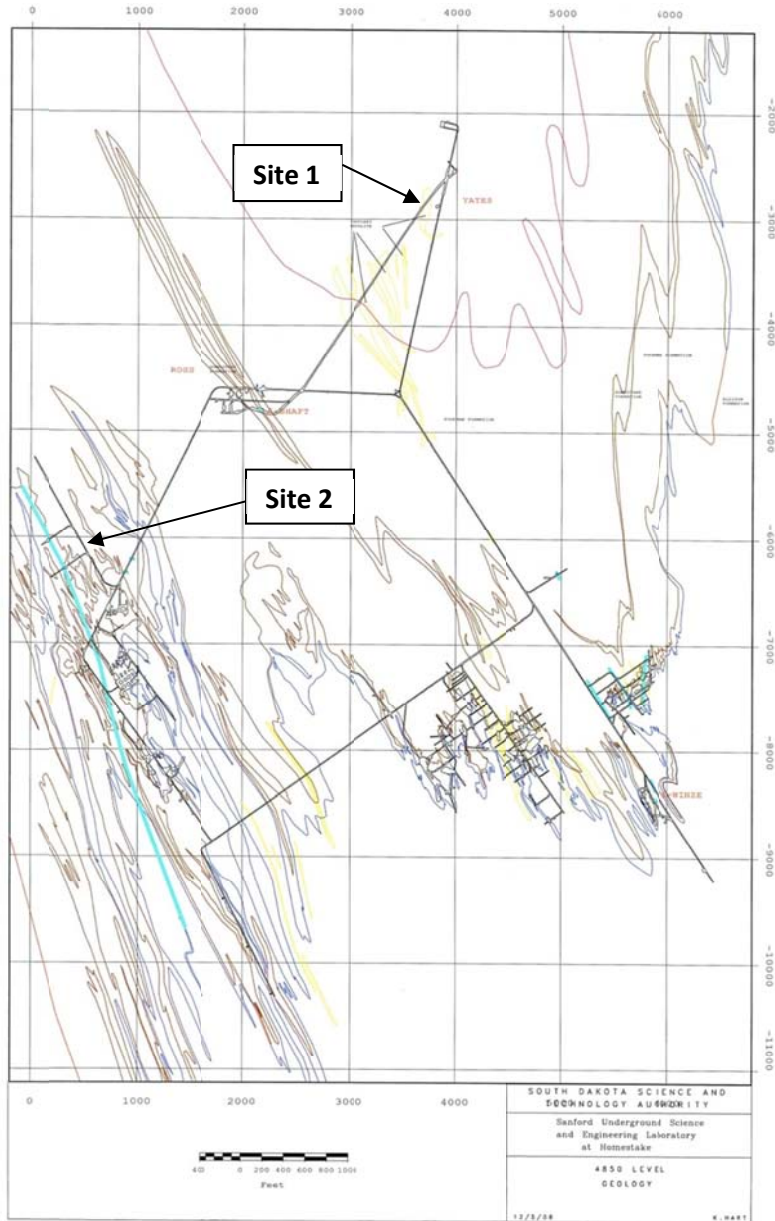
Figure 2.1. Geologic map of the 4850L, with locations of prospective kISMET Sites 1 & 2.
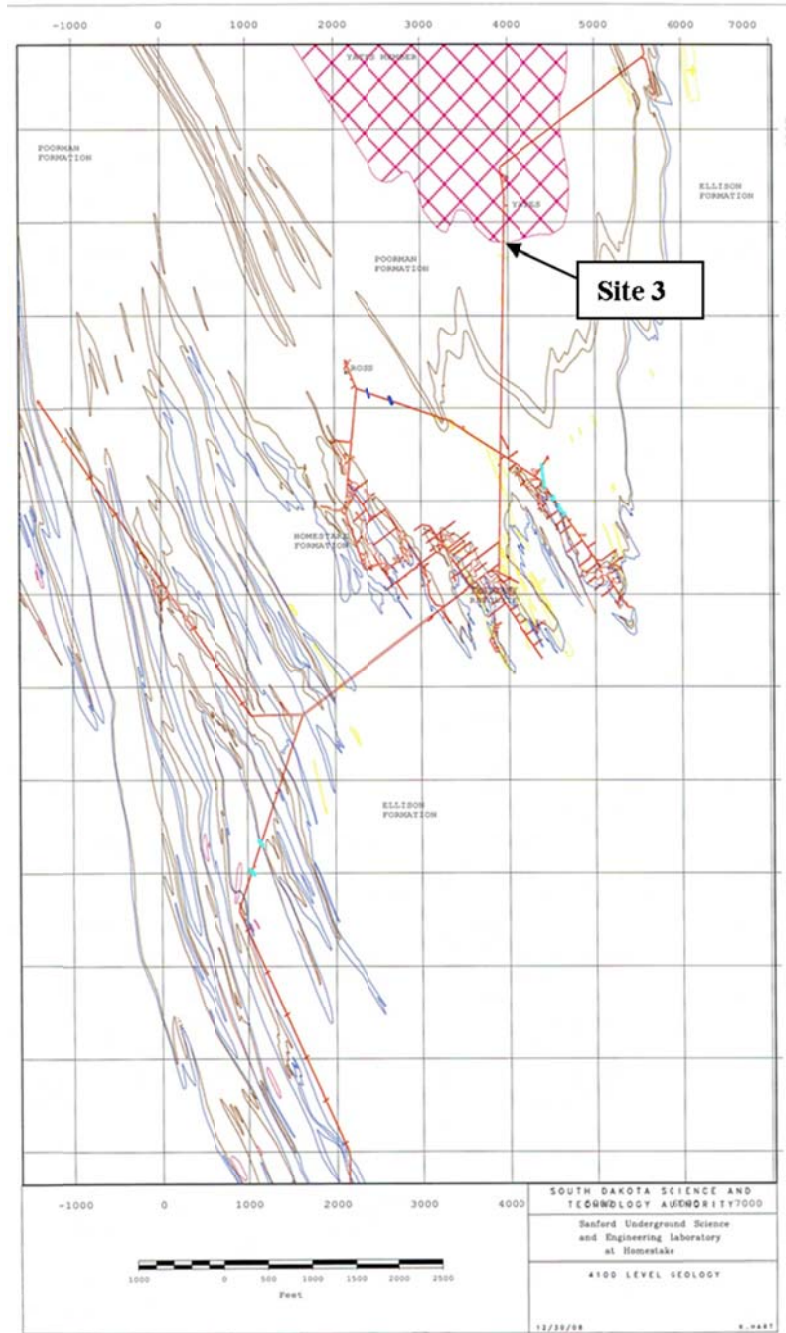
Figure 2.2. Geologic map of the 4100 level, with Site 3.

Site 1 was where the University of Wisconsin-Madison researchers had previously conducted stress investigations on the 4850L (Fig. 2.3). This site had the following advantages:

- Existence of well-characterized core holes in immediate vicinity which could be used for future monitoring efforts;

- Location is within Yates amphibolite, a more massive unit that is representative of EGS-type basement rocks;

- Location is in well-ventilated and rehabilitated portion of the 4850 level.

However, Site 1 also had some key drawbacks for the location of kISMET, including:

- The location is very close to existing physics laboratories;

- It is in an area of high traffic, which would require excavation of a side alcove for any drilling work.

This site had the potential to be used to determine in situ stress, but it did not appear suitable for a hydraulic stimulation experiment given the proximity to several dedicated physics laboratories. Bill Roggenthen and a graduate student at SDSMT have been conducting a cross-drift seismic tomographic survey in the area near the so-called Big X (intersection between the East and West Access Drifts near Drill Stations 1 & 2 in Fig. 2.3) to look at differences in seismic velocity. They have observed some significant differences that appear to correspond with the presence of rhyolite dikes and zones within the amphibolite that appear to have more intense fracturing (Fig. 2.4).

Three of the characterization drill holes at Drill Station 2 have widely varying fluid pressures as monitored by pressure gauges. They range from a high of 700 psi (5 MPa or 50 bars) (Fig. 2.5) to values of 25 and 5 psi (1.7 and 0.34 bar), indicating that the fracture networks that these boreholes intersect are poorly connected. Another borehole near the NASA Astrobiology Institute bioreactor (Hole 3A at Drill Station 1) has a static pressure of 1200 psi (8.3 MPa) suggesting that it is connected to fractures that reach up to the 2000L to sustain this hydrostatic pressure.
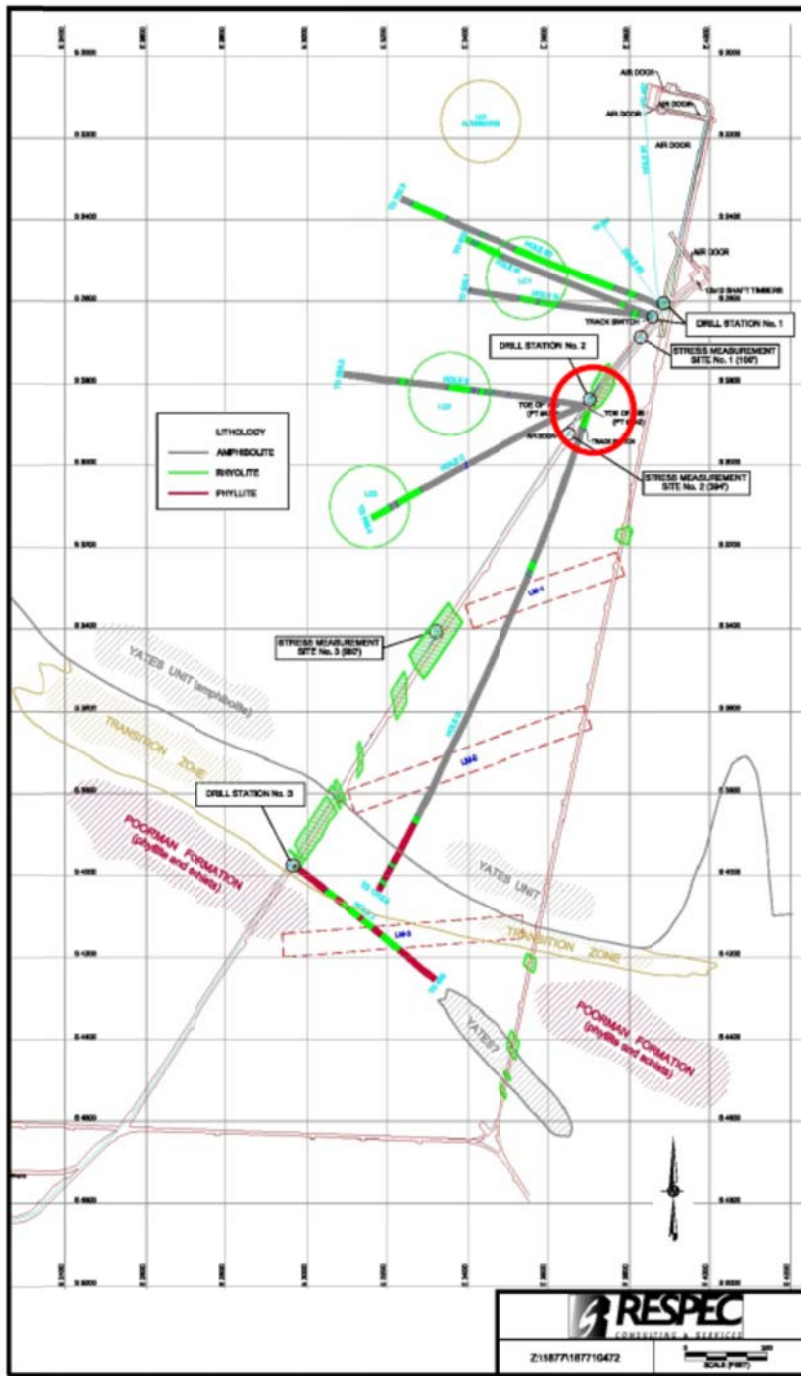
Figure 2.3. Location of Site 1 (red circle), the location of the University of Wisconsin-proposed in situ stress experiments.

Figure 2.4. Veined and sheared amphibolite that corresponds to a zone of decreased seismic velocity between the East and West Access Drifts near Drill Stations 1 & 2.

Figure 2.5. Instrumented drill hole with a static pressure of 700 psi (50 bars) at Drill Station 2.

Site 2, considered during our February 12, 2015 visit, was in the 17 Ledge area, south of Ross Shaft, also on the 4850 level. This site was the location of a DUSEL heater experiment proposed by Eric Sonnenthal (LBNL). The main advantages of this site are:

- Remote location is far away from existing and proposed physics laboratories and has very low traffic;

- There are several cross drifts, which would facilitate monitoring of fracture experiments;

- One of the cross drifts has a larger opening at the end which could accommodate drill rig and other equipment.

However, the site has some key disadvantages, which include:

- Area is poorly ventilated and needs work to stabilize drifts. This would require significant ground support (e.g., rock bolting) and other improvements to make the area safe to work in which would take time and money;

- Rock consists of highly foliated schists of the Poorman and Homestake Formations (Fig. 2.6), which add complexity to fracturing and may not be broadly representative of EGS basement rocks.

Figure 2.6. Folded and fractured schist of the Poorman Formation in first cross drift in 17 Ledge area, 4850 level. Photos are approximately 1 m across (left-hand image) and 0.5 m across (right-hand image).

We also investigated a third potential location, Site 3, located near the air door along the main drift by the Yates Shaft on the 4100L. The site had several key advantages, which include:

- Located on the 4100L which has no physics laboratories and therefore very low traffic;

- Location is within Yates amphibolite, which is a massive unit representative of EGS-type basement rocks;

- Could site a vertical borehole so that it would intersect both Yates amphibolite and Poorman schist (Fig. 2.7), which have a 30-40 degree dipping contact at this location. This is advantageous because we would potentially have two rock fabrics and one stress field to test effects of rock fabric on fracturing;

- Location is in a well-ventilated and rehabilitated portion of the 4100L;

- This level was not flooded when water rose in the mine after the pumps were turned off in 2003, and therefore the drift walls are more pristine (no iron staining) and other infrastructure (e.g., rock-bolt collars, pipes in ceiling, etc.) are not as rusty as on the 4850L.

However, this site does have some key challenges. These include:

- The drift is too small to accommodate standard drill rigs. We would need to mine out a 10 ft × 10 ft alcove for the kISMET experiment;

- Very little rock characterization work has been done in this area;

- The site lacks needed infrastructure such as water, electricity, and internet, which would have to be installed at this location;

- Proposed water reservoir for fire suppression was planned near the Yates shaft on the 4100L, and we would need to ensure that generated fractures do not compromise this reservoir;

- The site has standing water on the invert (floor) of the drift during our visit, a condition that is being managed by submersible pumps;

- The site is shallower (4100 ft (1250 m)), so it has less overburden (and thus lower vertical stress (σ_v) than the deeper 4850L sites;

- The site is directly above the Davis physics campus.

Figure 2.7. (a) Fractured and veined Yates amphibolite on 4100L; (b) Folded schist of the Poorman Formation on 4100L. Photos (both left- and right-hand images) are approximately 2 m across.

Based on our review criteria, none of these initial sites was deemed satisfactory for the kISMET experiment. The sites were either in an area too close to existing physics experiments, or were in areas that would be too costly to develop based on our project's budget. We asked SURF if they could identify

any other sites that would meet our criteria. After some consideration, they proposed a fourth candidate site, located on the 4850L in the West Access Drift where there is a section of double-wide track within 450 ft (137 m) of Governor's Corner. This site (circled area in Fig. 2.8) has a number of key advantages:

- It is located outside of the main traffic area and is distant from existing physics experiments;

- SURF is in the process of upgrading the structural support in the West Access Drift, which would allow kISMET to take advantage of these upgrades at no cost to the project;

- There is an electrical connection available at Governor's Corner, along with direct access to water and drainage;

- The site is wide enough to allow a drill rig to operate while still permitting passage past the site. And the crown is high enough so that the drill rig can drill and core vertical boreholes without needing any excavation at the site;

- The site is in competent rock (Poorman Formation) and is outside of the zone of rhyolite dikes, which create unwanted complexity in stress and lithology.
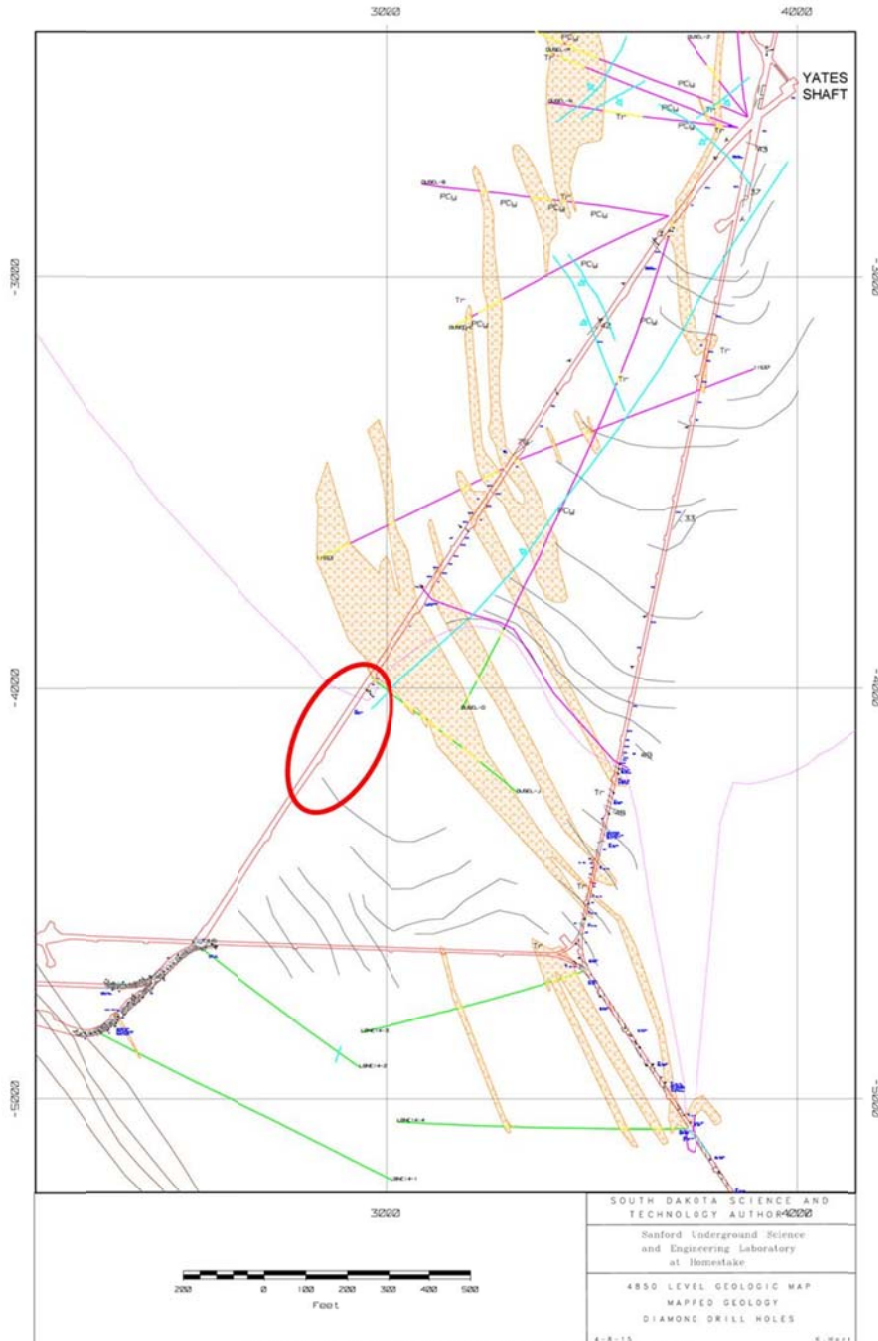
Figure 2.8. Geologic map of 4850L, with red oval indicating the site selected for initial kISMET experiments. Mapped rhyolite dikes are indicated by the tan stippled pattern.

Our team (Pat Dobson, Curt Oldenburg, and Bill Roggenthen) returned to SURF on May 21, 2015, to examine this site. We measured the dimensions of the site (Fig. 2.9) to verify that it could accommodate our boreholes. Based on all of the positive attributes of this location and our kISMET criteria, we decided to locate the kISMET project at this site (Fig. 2.10).
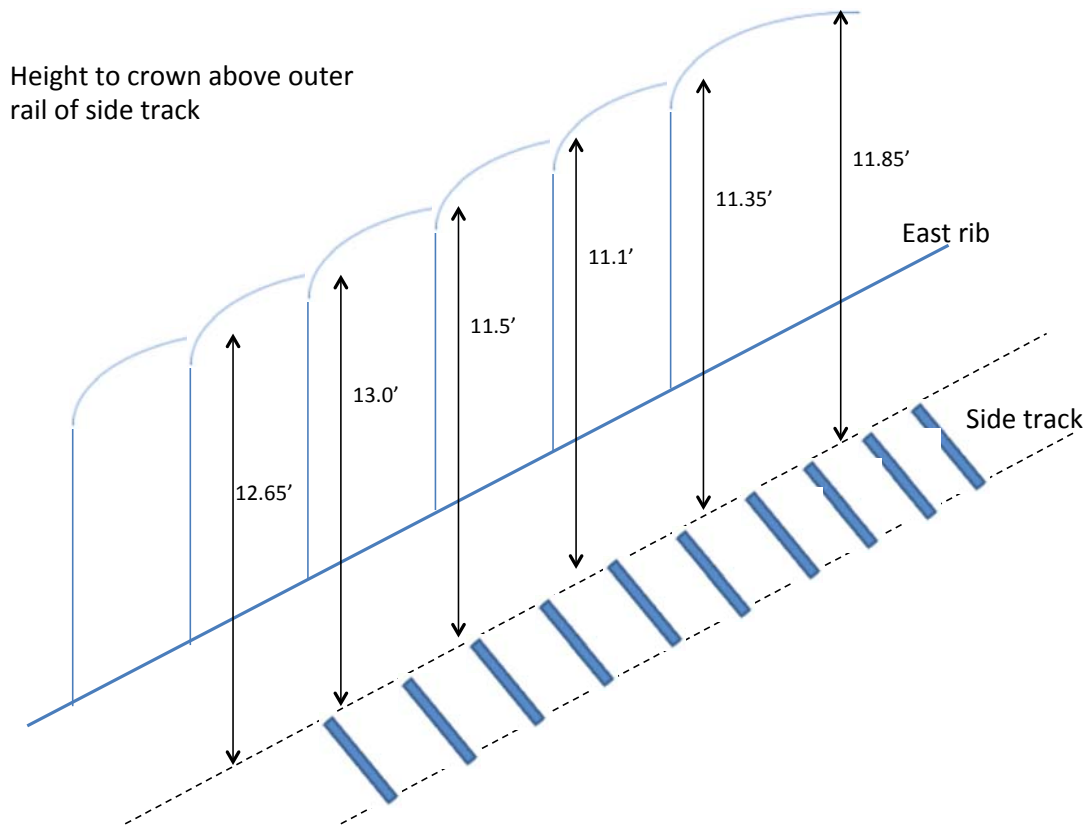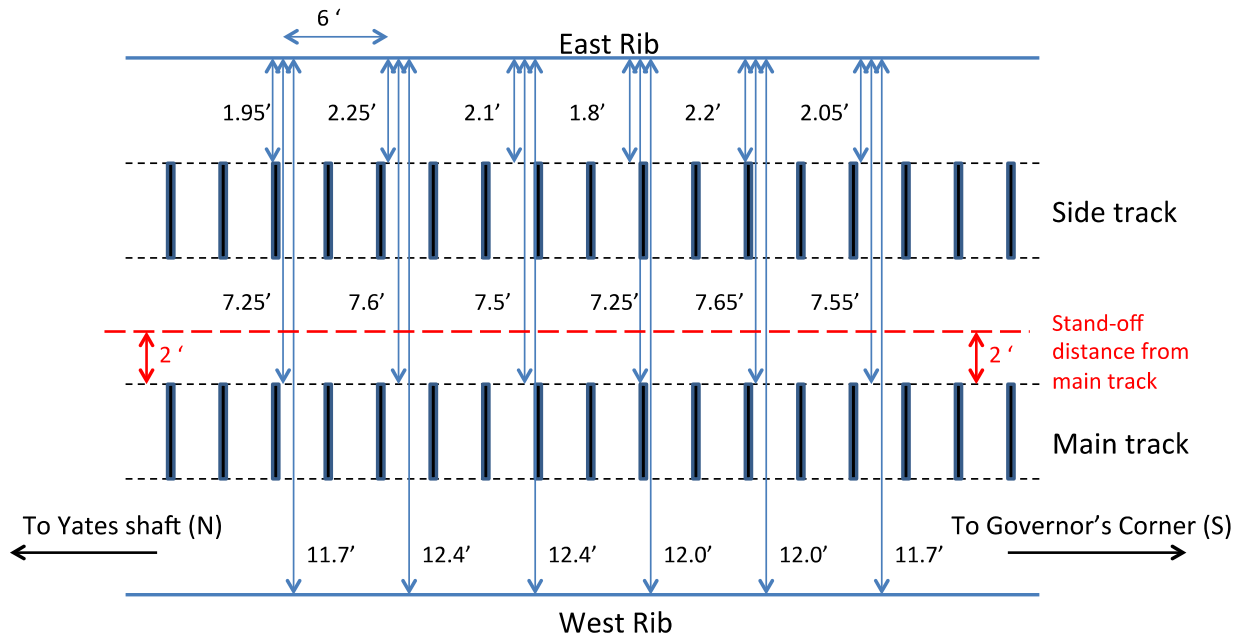
Figure 2.9. Dimensions of site (in decimal ft) on the West Access Drift of 4850L selected for kISMET.

Figure 2.10. Upper image: Composite photo of site taken on May 21, 2015 spanning approximately 60 ft (18.3 m) along the east rib of the West Access Drift. Lower image: Photo taken in February 2016 showing new ground support consisting of rock bolts and wire mesh. (For reference, the yellow kISMET spray paint on right-hand side of upper image is the same as that in left-hand side of lower image.).

2.2   Borehole Configuration

The next challenge in kISMET site development was to drill a (sub) vertical borehole array that would allow us to have four monitoring boreholes surrounding a central experimental borehole. Vertical boreholes are specified because we want the borehole to align approximately with a principal stress direction; at this depth, ~4850 ft (~1478 m) below ground surface, $\sigma_l \approx \sigma_v$ due to overburden stress.

In one of our earlier concepts, we envisioned an alcove that would allow drilling of a conventional five-spot configuration, with four vertical monitoring wells spaced at 90-degree intervals around a central

borehole. However, the cost of excavating such an alcove was prohibitive. We then developed a different design in which all of the borehole surface locations were in a straight line, but the outer holes were deviated so that they would form a five-spot configuration at the completion depth of 50 m (164 ft). This configuration is depicted in Fig. 2.11.

Configuration of boreholes on West Drift, 4850 level

3 m

Plan view

The center NQ borehole (blue) and the two nearest HQ monitoring boreholes (orange) are vertical; the outer HQ monitoring boreholes (green) are directional, and end up flanking the central borehole on either side, so that the bottom hole configuration (at 50 m) is similar to a five spot pattern. The surface locations of the 5 boreholes are all in a line on the side of a double-wide drift on the 4850 level. The center borehole is 100 m deep)

Cross sectional view

50 m

50 m

Figure 2.11. Views of proposed experimental layout on 4850L. The central vertical borehole (NQ) extends to a depth of 100 m (328 ft) (the other boreholes (HQ) will be 50 m (164 ft) deep).

The team discussed several key parameters of the holes – the spacing of the monitoring boreholes away from the central experimental (fracturing and stimulation) borehole, the depth of the boreholes, and the diameter of the boreholes. Key considerations were the physical and experimental requirements of the project, as well as the cost. We wanted to have the monitoring boreholes sufficiently close to permit proximal monitoring of the initiation and growth of the stimulated hydraulic fractures, while not having the holes so close that the fractures would grow to extend far beyond the monitoring boreholes. We also wanted to minimize the chance that the boreholes might intersect one another during drilling, a contingency we could avoid by ensuring that expected drilling deviation did not exceed the spacing of the boreholes. Another important consideration was to make sure that the boreholes were deep enough so that they were beyond the influence of the drift in terms of stress deviation from ambient condition. We made the assumption that this would require the test zones to be at least three drift diameters (i.e., three times ~12 ft, or 4 m), which comes to 12 m (39 ft) away from the invert to escape this effect. We decided to have the monitoring wells drilled to a depth of 50 m (164 ft) to give us plenty of space to conduct our experiments. We decided to drill the central experimental well even deeper in order to provide additional space at depth to conduct the first stress measurements, thus reserving the shallower part of the borehole to conduct the monitored fracturing (stimulation) experiment once the approach was proven to work. The

inclusion of extra depth in the central borehole to work out the bugs in the fracturing system proved to be a very good decision, as will be discussed in the stress measurement section.

The final decision was what size boreholes to drill. We selected HQ sized holes (dia. = 3.78 inches, 96 mm) for the monitoring boreholes, as this would give us more flexibility in deploying existing monitoring equipment in these holes. We were also informed that it would be easier to control the trajectory of these larger diameter holes when drilling through this strongly foliated rock due to the stiffer HQ drilling assembly relative to NQ. We chose a smaller diameter NQ hole (dia. = 2.98 inches, 75.7 mm) for the central experimental hole. This decision was influenced by the fact that the University of Wisconsin already had an NQ high-pressure straddle packer assembly. Although we procured a new dedicated packer assembly for our experiments, we kept the Wisconsin packer system in reserve as a backup if needed.

2.3   Selection of a Drilling Contractor

Our team spent a good deal of time developing criteria for selecting the best drilling system and contractor for our project. We contacted three different companies and requested them to provide us with drilling proposals that took into consideration all of the site and project requirements of our project. The drilling requirements specified the drilling configuration illustrated in Fig. 2.11, and also noted that the driller would need to comply with the SURF work and safety requirements. SURF operates on a four-day work week underground, so that the drilling plan would need to take this into consideration. The proposals from bidders needed to specify the drilling equipment that would be used, its dimensions and weight, the required services (power, water, ventilation, etc.), and what additives would be used for the drilling fluids. The proposals also needed to detail prior underground drilling experience and whether the company had prior experience working at the SURF facility. The bidders were requested to provide us with an itemized list of costs for mobilization, rig operation, coring, and all related drilling costs, as well as logging tools needed to document the borehole orientations. The bids were to be evaluated using a best-value criterion.

All three companies that we contacted submitted bids. Our team evaluated the proposals by breaking down the different components of the proposals. This included: (1) the cost estimates for each component of the project, along with the total estimated cost; (2) how realistic the time for conducting the work was (given that the actual costs would be impacted by the number of days spent drilling); (3) the suitability of the rigs for conducting the drilling work; (4) the experience that the company (and individual drillers who would be working on this project) had in working underground, and at the SURF facility in particular; and (5) past drilling performance. To evaluate this latter factor, we contacted prior clients to find out how their drilling experience turned out. We also had a drilling expert at Sandia National Laboratories review the proposals and provide our team with feedback. Based on a combination of factors (low price, realistic drilling times, superior rig, experienced drilling crew, and good recommendations), we selected First Drilling as our subcontractor for the drilling work.

2.4   Site Preparation and Logistics

We engaged SURF as a subcontractor to develop the selected kISMET site on the 4850L so that it would be suitable for hosting the drilling operations and subsequent experimental work. SURF provided the following site improvements under a time and materials contract:

- Structural support (rock bolts, mesh, etc.) in the drift and ground work to level the area where the drill rig would be located;

- Electrical power for the drilling via a temporary 480V, 200 Amp line coming from the transformer near the #6 Winze, along with 120 V power. A permanent power line was installed post-drilling prior to the experimental work.

- Excavation of an 18 in × 18 in × 18 in sump at the kISMET site;

- Installation of pick points to facilitate assembly of the drill rig, along with bolts and anchor points to secure the drill rig for each hole;

- Installation of a fiber optic line with an 8-port switch to accommodate the needs of the monitoring equipment for the kISMET experiments, as well as the geophones that will be installed in nearby locations;

- Fresh water from the 6-inch industrial water line that runs in the drift. There is a 2-inch spud with a valve that is located within 50 ft of the site. The line has ~80 psi (0.55 MPa) pressure, so no pressure reducer is needed, and this line is more than adequate for supplying water for drilling and subsequent experimental needs.

- A water-flush line to be used for disposal of cleaned (desilted) drilling water;

- A rail car with a spool and an air compressor for the packer system.

In addition to these services and improvements, SURF also provided an escort to accompany and monitor our underground operations. SURF also assisted in the transport of equipment down the Yates shaft and over to the kISMET site, as well as the transport of all core boxes up to the surface core repository at SURF.

2.5   Drilling

Our team (Curt Oldenburg, Pat Dobson, Paul Cook, Herb Wang, and Bill Roggenthen) visited the SURF site on April 13, 2016, to meet with the SURF staff and the driller from First Drilling, Bill Wortman. We gave an overview presentation to the group, which was followed by a discussion of the scope of work planned for the drilling operation. This was followed by a discussion of the health, safety, and environmental requirements for working underground and needed documentation. We then reviewed the proposed work schedule and discussed the logistics for drilling mobilization, drilling activities, and demobilization of the drilling rig. We also presented a memorandum of understanding (MOU) between SURF and the kISMET team. Under the terms of the MOU, a representative from each institution participating in the project was required to sign the document (MOU-2015-0801). After a safety briefing, we then visited the 4850L to inspect site conditions and discuss any needed modifications for work. A number of recommendations from this meeting were implemented:

- Contracting a local surveyor (Randy Deibert of Professional Mapping & Surveying, LLC) to help site and align the boreholes;

- Obtaining the services of the gyro logging company (as part of the drilling contract) to ensure that our crew was fully trained in the use of this tool;

- Making sure that we always had a kISMET team representative on site throughout the drilling phase;

- Having custom core boxes built to accommodate the 5-ft (1.52 m) sections of core so that they could remain intact.

The next 6-8 weeks were spent completing all of the required safety and work-procedure documentation, finalizing the subcontracts with First Drilling and Professional Mapping & Surveying, and putting together a work schedule and plan for core characterization. These documents included the experimental planning statement (EPS), standard operating procedures (SOPs) for all of the drilling activities, a job hazard analysis (JHA) of the drilling activities, and a work planning and control (WPC) document for LBNL work activities at the SURF site (AU-0199). After all of this documentation was completed, and First Drilling had provided SURF with a complete shipping manifest of all of the drilling equipment that

was going to be transported underground to the site, along with detailed information on all electrical devices and material safety data sheets (MSDS) forms for all chemicals that would be used in the drilling process, we were finally given the authorization to proceed from SURF.

The drilling operation has a number of significant safety hazards, including high pressure hoses, rotating rods, and high voltage. The work site was demarcated with barriers – anyone who wanted to pass by needed to get permission from the driller, and undergo a short safety briefing from the driller. In most circumstances, the driller stopped the rig prior to letting people pass through the area. SURF encouraged people to use the East Access Drift to minimize traffic through the area. Everyone at the drill site was required to follow the rules of both SURF and First Drilling – this covered all kISMET staff present at the drill site. All workers complied with the SURF safety regulations, used specified PPE, and had required safety training. First Drilling and kISMET workers were accompanied by a SURF staff member that had Facility Guide training. All people who conducted work on site were required to take the site-specific 8-hour safety training class, a course offered by SURF on a regular basis.

The First Drilling crew began mobilization at Lead on June 13, 2016. The First Drilling crew used a 20 HH underground electric/hydraulic core drilling rig with a FMC W11 mud pump. Drilling commenced on June 22, and was completed on schedule (and under budget) on July 20. Below is a table with details on the drilling of the five boreholes.

Table 2.1. Borehole drilling notes. K001 is shorthand for kISMET-001, etc.

Borehole	Date spudded	Date completed	Type	Depth (ft)	Depth (m)	Core loggers
kISMET-001	6/22/16	6/27/16	HQ, directional	175	53.3	Paul Cook
kISMET-005	6/28/16	6/30/16	HQ, directional	175	53.3	Paul Cook
kISMET-004	7/05/16	7/07/16	HQ, vertical	164.9	50.3	Bill Roggenthen
kISMET-002	7/07/16	7/11/16	HQ, vertical	164.9	50.3	Bill Roggenthen
kISMET-003	7/12/16	7/20/16	NQ, vertical	329.9	100.5	Bill Roggenthen Drew Siler

The drilling procedure was similar for all boreholes. After drilling the first 10-15 ft (3.0-4.6 m) of each borehole into the invert (floor), the borehole was reamed and a 10-ft section of stainless steel casing was cemented in place and the first initial directional survey was performed to ensure that the hole was oriented properly. The boreholes were surveyed periodically during drilling with the Reflex EZ-Gyro tool to ensure that the proper orientation of the holes was maintained. The tool has a reported accuracy of 1 degree azimuth and 0.3 degrees dip.

One of the key drilling concerns identified prior to drilling was the highly foliated nature of the rock and the associated tendency for the drill bit to deviate off course and follow the foliation. First Drilling employed several strategies to help mitigate these concerns. These included:

- Use of stiff 5-ft drill rod sections;

- Drilling with lower weight on bit. This resulted in slower penetration rates, but allowed for better control of the hole trajectory. The planned drilling schedule was to drill around 50 ft (15.2 m) per shift to ensure an accurate drilling trajectory to create the kISMET five-spot at 50 m (164 ft) below the invert (floor) of the drift.

- Precise initial orientation of the drill string when spudding the well. Proper orientation of the hole is critical. The surveying crew worked with First Drilling to ensure that this was done properly. We found after the first hole that the survey crew was not needed – the gyro tool provided sufficient control to orient the drill rig properly. The REFLEX Gyro tool is shown in action in Fig. 2.12.

- Securing of the drill rig to the invert using timber, chains, sprags, bolts, and anchor points for each drill-hole location. The fittings were tightened again right after the hole was spudded to make sure that it does not move. Foot clamps and wedges were used to hold the bit in place when spudding the hole.

- Use of a stabilized (octagon-shaped) core barrel to provide added rigidity to the system;

- Running intermediate gyro surveys in the holes to monitor the orientation of the holes. An initial survey was run at the time the surface casing was installed (at ~15 ft (4.6 m)), another at (82 ft (25 m), and a final survey at the bottom hole location (164 ft (50 m)) for the HQ holes. Additional intermediate surveys were run for the deeper (328 ft (100 m)) NQ hole.

Figure 2.12. Orienting the drill pipe at the start of kISMET-004 using the REFLEX gyrocompass.

There was 100% recovery of the core from all of the boreholes. Only one open fracture was observed during drilling (Fig. 2.13); all of the core consisted of phyllite of the Poorman Formation. Each section of core was described and photographed at the site, and then stored in core boxes, which were transported to the surface for storage at the SURF core repository. Examples of the core descriptions and core photographs are depicted in Fig. 2.14. Daily drilling reports were provided by the driller, and daily shift reports were provided by the kISMET staff on site. After drilling was completed on July 20th, the rig was demobilized and baseline borehole logging and deviation surveys were carried out.

Figure 2.13. Open fracture encountered in kISMET-002 at ~91 ft (27.7 m). The fracture is lined with small quartz crystals, and is interpreted to be related to Tertiary-age mineralization.

Figure 2.14. Examples of core descriptions (left-hand side image) and photographs from borehole kISMET-003, core run 8 (right-hand side image).

2.6   Geophysical Borehole Deviation Logging

Borehole deviation was measured twice after drilling and coring were completed, once using a dedicated borehole deviation tool and a second time using the integrated deviation sensors on the optical televiewer. Sonde azimuth was estimated using a three-component (3C) flux-gate magnetometer while inclination was measured using a 3C accelerometer. Measurements were made every 10 cm (3.94 in) from top-of-casing (TOC) to the bottom of each borehole (either 50 m or 100 m below grade surface).

The magnetic deviation data showed a maximum of ~6.5 m (21.3 ft) *XY* deviation relative to surface locations for angled boreholes kISMET-001 and kISMET-005 as shown in Fig. 2.15. While the bottom of the stimulation well (kISMET-003) deviated roughly 6 m (19.7 ft) from vertical, the top 50 m of the well deviated only ~2 m (6.6 ft) from the vertical direction, confirming the creation of a five-spot pattern at 50 m depth based on gyro deviation log results. kISMET-002 and kISMET-004 deviate less than 0.8 m from vertical, confirming nearly vertical boreholes, consistent with the gyro deviation logging. Figures 2.15a and 2.15b show the bull's eye map-view deviations for all five boreholes with depth superimposed on the traces to indicate deviation as a function of depth (Fig. 2.15b). As shown in Fig. 2.15d with no horizontal exaggeration, First Drilling did an excellent job in meeting our design for a five-spot at 50 m depth given the challenges present with foliated rock. The final surface layout of the boreholes based on the surveying work is depicted in Fig. 2.16.

(a)

(b)

(c)

(d)

4850 ft

4850+165 ft
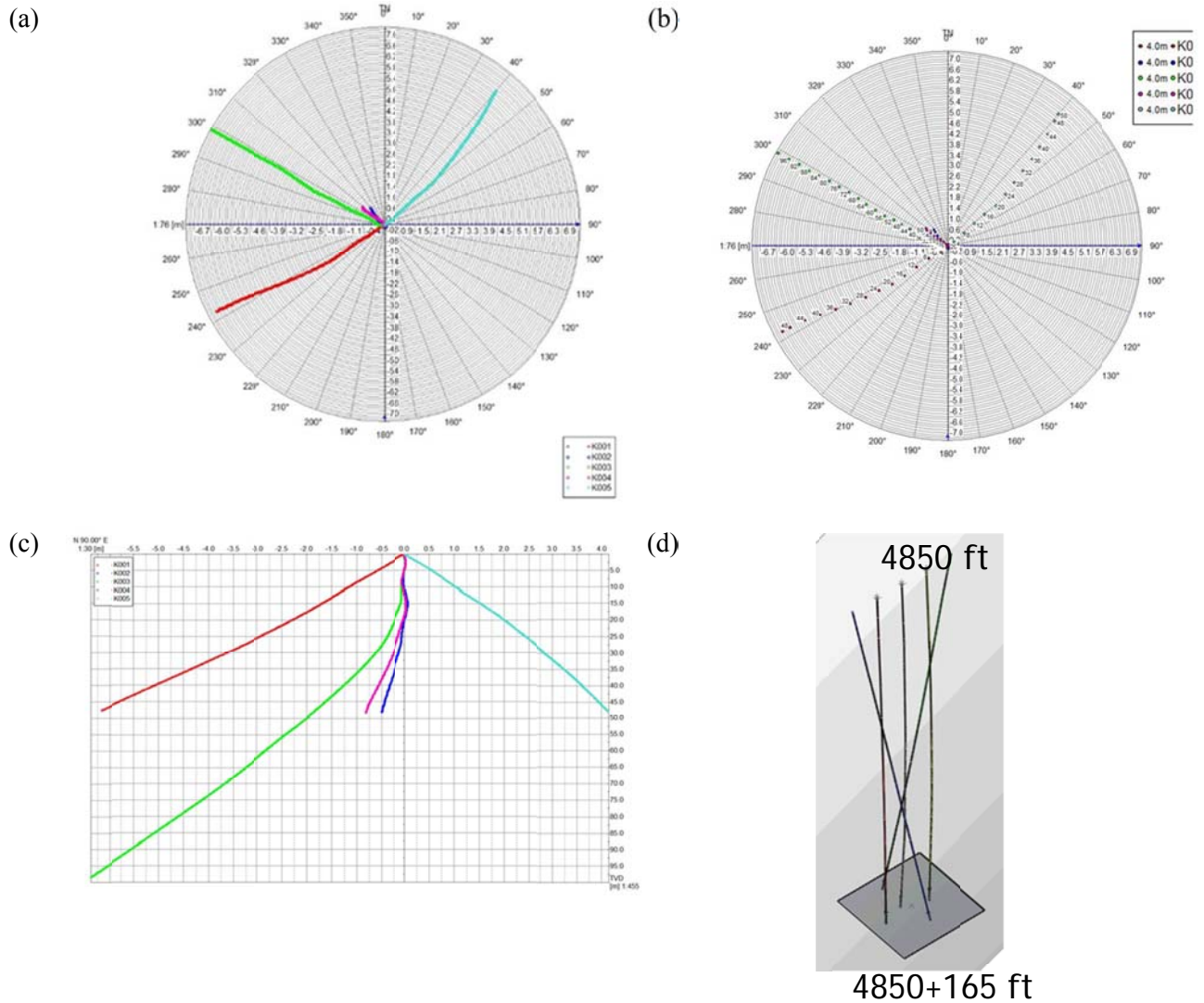
Figure 2.15. Deviation logging results for the kISMET boreholes. (a) Bull's eye composite deviation logs for all four wells. (b) Bull's eye composite deviation with depths indicated on each trace to reveal that borehole K003 (kISMET-003) did not deviate far from the five-spot target at 50 m depth, but deviated more at deeper levels. (c) Side-view of the deviations shown with large horizontal exaggeration. (d) Depiction of borehole trajectories to a depth of 50 m showing the five-spot pattern created 50 m in the West Access Drift on the 4850L.
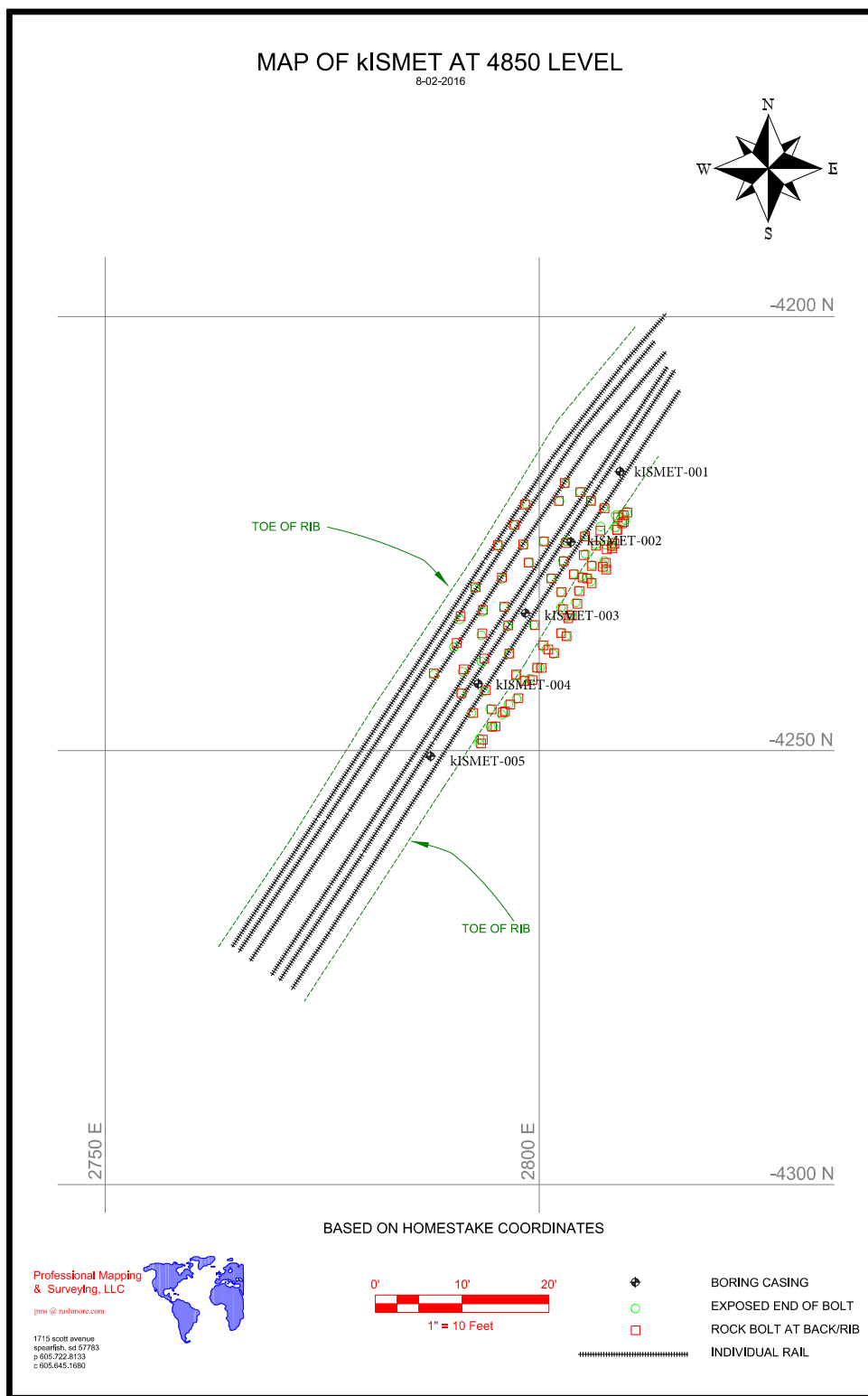
Figure 2.16. Survey of surface features including the boreholes at the kISMET site.

2.7   Temporary Decommissioning

After the well logging, stress measurements, and fracture experiments were completed, the wells were capped and covered with enclosure "boxes" so the site can be walked on and driven over, and so the side rails could be utilized. A photograph of the boreholes after this work was completed is depicted in Fig. 2.17.
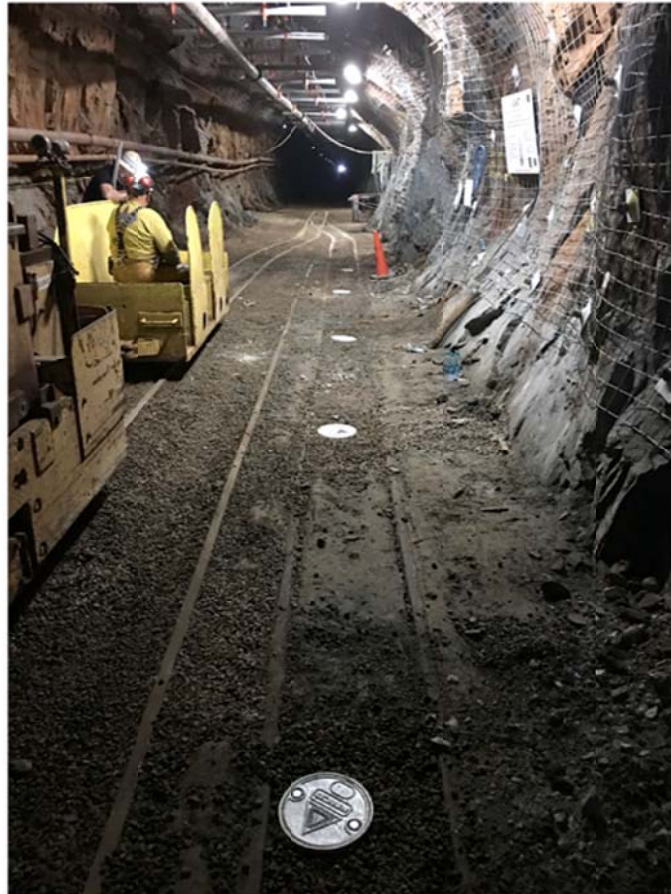
Figure 2.17. Five well "boxes" with white circular covers in the photo show well completion at the kISMET site in October 2016 after field experiments were completed.

3. LABORATORY ROCK CORE STUDIES

Lead Authors: Seiji Nakagawa, Hiroki Sone, Peter Vigilante, and Tim Kneafsey

The primary objectives of the laboratory core studies are (1) to characterize the mechanical and hydrological properties of the rock (phyllite of the Poorman Formation) from the kISMET site at SURF and (2) to examine the impact of the rock fabric and in situ stress anisotropy on hydraulic fracturing. These laboratory experiments are complementary to the in situ hydraulic fracturing experiments in that they examine properties and behaviors under highly controlled conditions that are not practical for field experiments, albeit at smaller scale than the field experiments. Because the laboratory experiments are conducted under a controlled and known stress state (magnitude and relative orientations of the principal stresses with respect to the anisotropy of the rock), comparison of the laboratory-produced fracturing to the fractures produced in situ may lead to more accurate estimation of the in situ stress state and better understanding of the observed in situ hydraulic fracturing. The rock samples used in the laboratory experiments were obtained from core from the NQ borehole in which the in situ hydraulic fracturing tests were conducted. While the more involved laboratory-scale hydraulic fracturing tests are still in progress, a series of basic rock property characterization experiments have been completed and are summarized in this section along with a discussion of the tests that are still in progress.

3.1 Baseline Rock Property Characterization

Before conducting laboratory-scale hydraulic fracturing experiments, a series of baseline rock property characterization tests were conducted. Our particular focus was on the impact of rock heterogeneity and the anisotropy resulting from the very prominent fabric consisting of foliations and small-scale folds in the phyllite. The anisotropy and heterogeneity of the rock properties were investigated by means of X-ray CT imaging and ultrasonic velocity measurements, followed by measurements of tensile strength and flow permeability.

3.1.1 X-Ray CT Imaging (LBNL)

Two core samples (diameter 2.00 inches) were obtained from the kISMET-003 NQ borehole from depth levels 258.4–259.9 ft (78.76–79.22 m) ("Long" core) and 250–251 ft (76.2– 76.5 m) ("Short" core) below the 4850L West Access Drift invert (floor). X-ray CT imaging was performed using a modified GE Lightspeed 16 medical CT scanner at 120 kV and 160mA. The CT data were calibrated by scanning a number of cylinders of light-element material with known density and constructing a calibration curve. The calibration curve does not account for atomic number, thus densities presented here are probably lower than gravimetric densities.

We present in Fig. 3.1 X-ray CT images of the core. Three cross sections are presented for each core segment. The first is a centrally located cross section perpendicular to the core axis. The core was aligned so that the laminations appear as vertical stripes in this cross section. The second set of cross sections are two core axis-parallel cross sections, one obtained from a vertical plane through the core (along the foliation planes), and the other in the plane perpendicular to the foliation. In Fig. 3.1, higher densities are presented as brighter shades of gray. Some regions have densities higher than what the instrument could measure under these conditions, which causes these regions to show as white spots. The lowest density regions in the core of Fig. 3.1 have densities near 2.5 g/cm^3.

Both cores show similar features in that in one direction, the scans appear somewhat uniformly laminated. In the perpendicular plane, the layers are quite disturbed and very rough. The core from 250 ft (76.2 m) is more heterogeneous than the deeper core. As shown, heterogeneity in rock fabric occurs even at the centimeter scale, making it difficult to extract a uniform sample for laboratory testing.
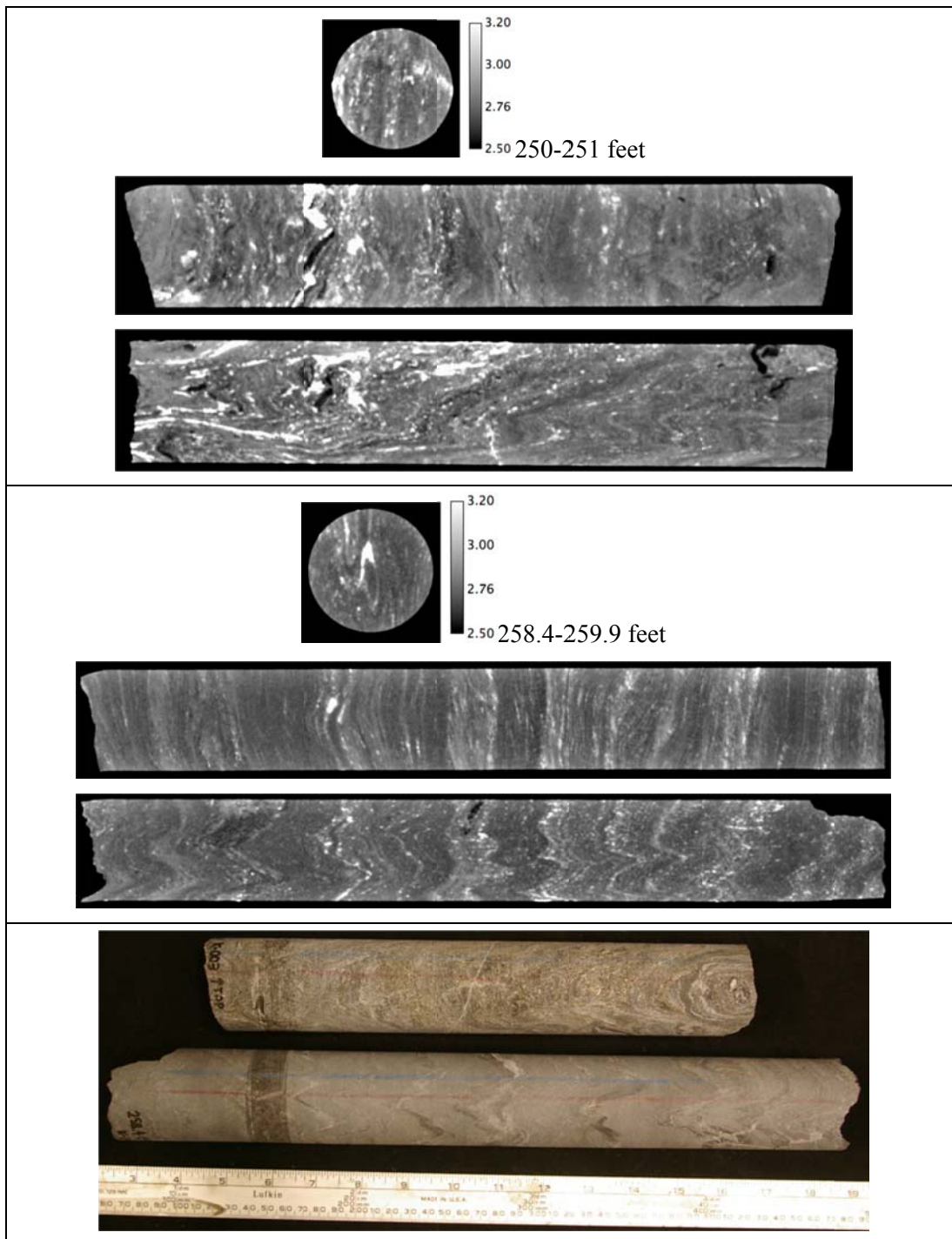
Figure 3.1. X-ray CT scans of core from 250-251 ft (~76.2 m) (top, Short" core) and 258.4-259.9 ft (~78.9 m) (center, "Long" core). Photographs of the both the "Short" and the "Long" cores are shown at the bottom.

3.1.2   Ultrasonic Velocity Measurements (LBNL)

Ultrasonic P-wave velocity was measured using a pair of narrow-band immersion transducers (Panametrics A303-S.Central frequency 1 MHz, transducer diameter 1.5 cm) along the diameters of the cores. The experimental setup is shown in Fig. 3.2. Before the measurements were made, originally room-dry core samples were soaked in tap water for five days at ambient temperature (~25ºC). This was done because under room-dry conditions, poor sample-to-transducer coupling did not allow transmission of high-frequency ultrasonic waves through the sample with sufficiently large amplitudes for accurate velocity measurements. Coupling the waves through water allows good transmission of the seismic energy through the sample. The imbibed water resulted in only 0.11% (Long core) and 0.14% (Short core) increases in the core weight, suggesting that the rock has very low permeability and porosity.

The wave travel time was measured and the P-wave velocity determined for a range of orientations and locations along the cores. For each core, the reference orientation was determined from the texture (foliation) on the surface of the cores. Because these planes have mm- to cm-scale folds in one direction along the foliation plane, at the ends of the core distinct linear alignment of the rock fabric can be seen in the direction of the fold axis as shown in Fig. 3.3. The direction of the fold axis, however, exhibited some variation even within a single cross section of the cores, which made it difficult to select the "correct" reference direction. Additionally, the overall foliation planes appeared to be locally tilted for the Short core (250–251 ft), cutting the core axis at shallow angles. (Note that this tilt appears to be more consistent with the large-scale geological structure of the mine compared to the Long core. Compare rock fabric Short and Long cores in Fig. 3.1.)
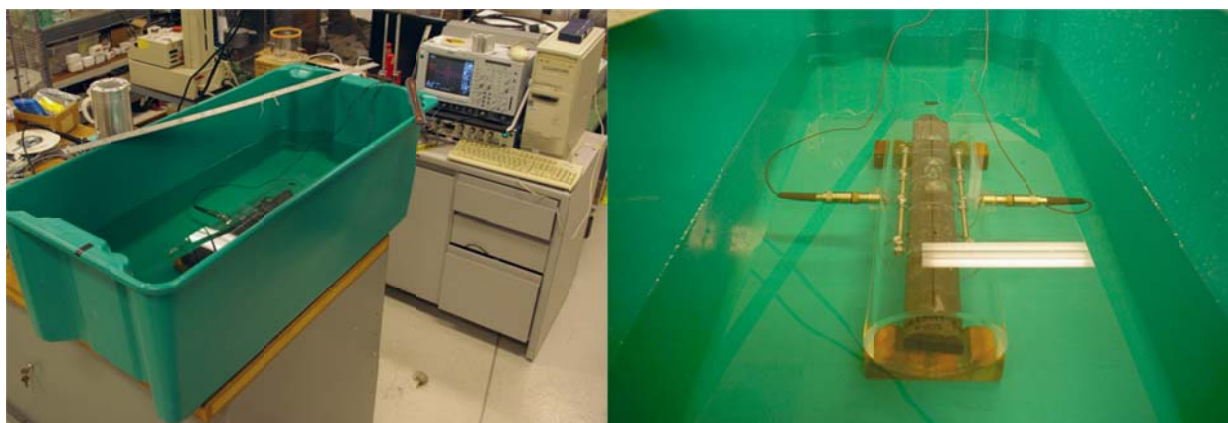
Figure 3.2. (a) Ultrasonic P-wave test setup. (b) Core sample immersed in the scan rig.
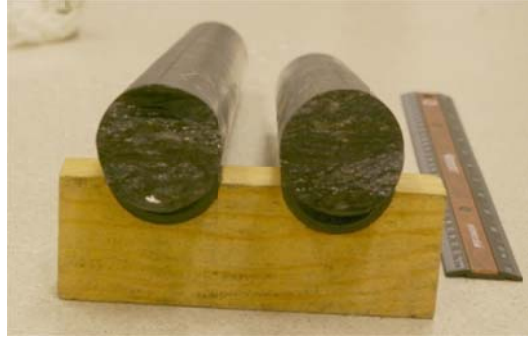
Figure 3.3. Foliation planes (in the horizontal directions in the image) observed at the ends of the cores. The direction of the planes and of the folds varies, however, and can be ambiguous.

The first set of measurements was performed to determine the orientation and the degree of anisotropy of the rock (Fig. 3.4). For each core, the ultrasonic velocity was measured around the core axis at three levels, in the directions -90º to +90º from the reference direction. Fig. 3.4a shows the determined velocities, each line showing measurements conducted at a single level. (Note that the numbers in the legend are the distance from the bottom end of each core). Each core exhibited very strong velocity anisotropy (as much as 15%) and a well-defined peak orientation, possibly resulting from rock foliation. The anisotropy measured for the Short core indicated that the direction of the mean fold axis selected based upon the surface texture was off by ~20º from the "true" reference direction.

Next, we measured the velocity changes (heterogeneity) along each core, in the directions -90º and 0º with respect to the reference direction (Fig. 3.4b). From this and the first measurements, it can be seen that velocities are generally slower in the Short core than in the Long core, particularly for the shallower half of the core (position > 100 mm). When compared to the X-ray CT images (Fig. 3.1), this low-velocity section coincides with a section containing a large amount of pyrite aligned in linear features in the rock, which can be identified as bright bands in the CT images and are clearly visible to the eye on the core surface. The rapidly changing velocity profile along the cores indicates strong, fine-scale (~1 cm or smaller) changes in the mechanical properties of the rock, possibly due to the well-developed foliation.

(a) Velocity anisotropy   (b) Velocity heterogeneity
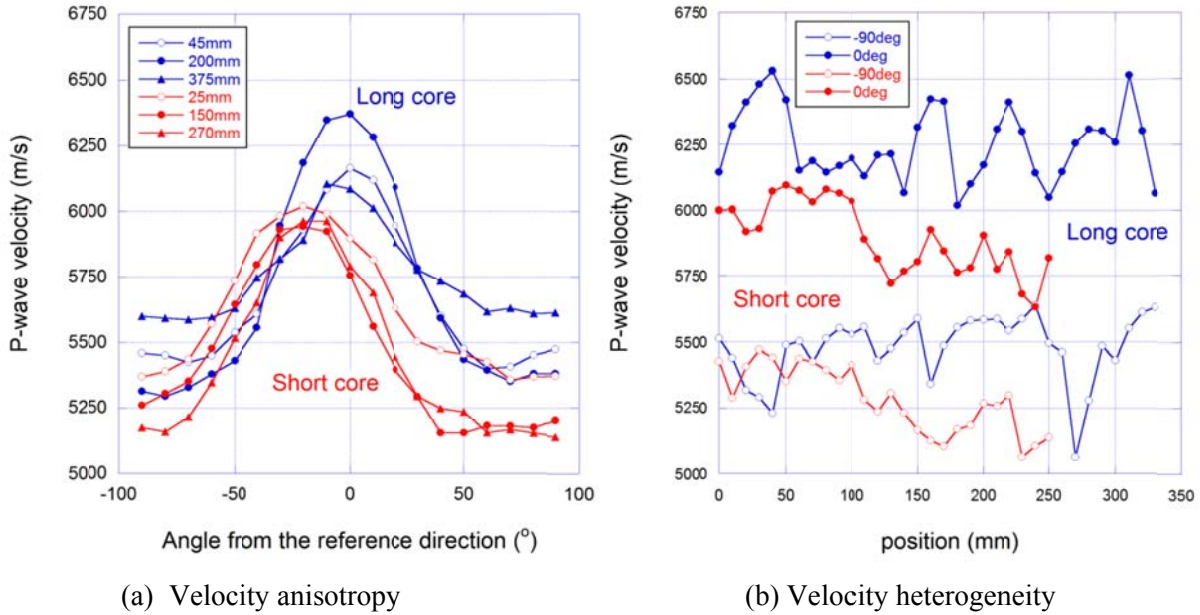
Figure 3.4. Seismic P-wave velocity anisotropy around (a) and along (b) the two cores. Very clear anisotropy is present for the entire lengths of the cores. Velocity also varies rapidly along the cores, possibly because of sub-centimeter-scale laminae with strong contrasts in elastic moduli. Note that the anisotropy is characterized only within planes perpendicular to the core axis. The smallest P-wave velocity in the rock can be even smaller in the direction perpendicular to the mean foliation planes.

3.1.3   Tensile Strength Measurements (Univ. of Wisc.)

Using short, disc-shaped samples (dia. = 25.4 mm, thickness = ~10–13 mm), Brazilian disc tests were conducted on rock samples obtained from the borehole at the same depths that the in situ stress measurements were made. The objective of these measurements is to understand the impact of the foliation plane on the tensile strength, crack formation, and crack propagation behavior in the rock. Several cylindrical plugs were sub-sampled from the core so that the plug cylinder axis is parallel to the foliation. Then the plugs were sliced into discs to obtain groups of samples that have consistent lithology and foliation within each group (Fig. 3.5a). Each disc was placed between two flat and parallel hardened steel surfaces, and then loaded diametrically at a constant displacement rate of 0.5 microns/sec until rock failure. Within each sample group, the angle between the foliation plane and the loading direction was varied over 0 to 90° (Fig. 3.5b). In theory, if the rock is isotropic and homogeneous, an opening-mode fracture will form parallel to the loading direction. However, due to the potential anisotropy of the tensile strength, the fracture geometry may be influenced by how the foliation is angled against the loading direction. Fig. 3.5c shows a representative load-displacement curve obtained from a single sample. By identifying the peak load reached during the experiment, we can calculate the tensile strength of the rock using the equation

$$\sigma_t = \frac{2P_{peak}}{\pi DT} \tag{3.1}$$

where P_{peak} is the peak load, D is the diameter of the cross section (i.e., 25.4 mm), and T is the thickness of the sample.
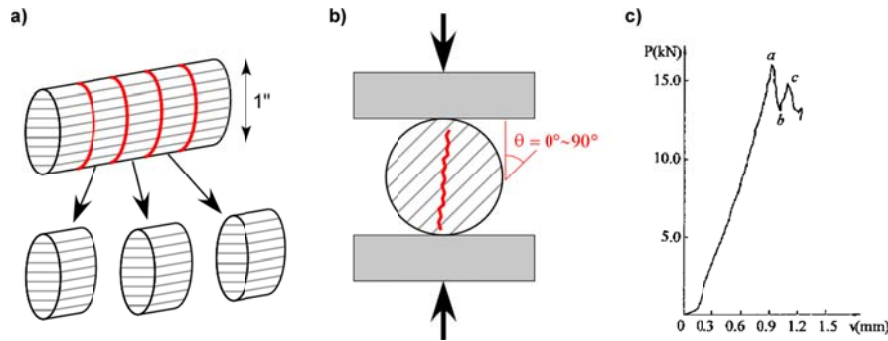
Figure 3.5. Brazilian-disc test (a) sample preparation, (b) test setup, and (c) typical test record (source: Wang and Xing, 1999).

Preliminary results are shown in Fig. 3.6. We see by comparing the load-displacement record that the elastic stiffness (represented by the slope) is indeed anisotropic, especially samples from core run 56, where the rock appears stiffest when loaded parallel to the foliation ($\theta = 0°$), consistent with the velocity measurements from Section 3.1.2. Tensile strength is also strongly anisotropic for both samples types where the rock is easier to split when loaded parallel to the foliation. Tensile strength ranges between 3–7.5 MPa (435-1087 psi) and 5–12 MPa (725-1740 psi) for samples from core run 41 and 56, respectively. The foliation, mostly defined by the alignment of phyllosilicate minerals, serves as a weak plane and seems to have influenced the fracture path of samples loaded diagonally relative to the foliation ($\theta = 30$–$60°$). Samples are planned to be scanned by the X-ray CT imaging as in Section 3.1.1, in order to digitally characterize the morphology of the fractures created in these tests.
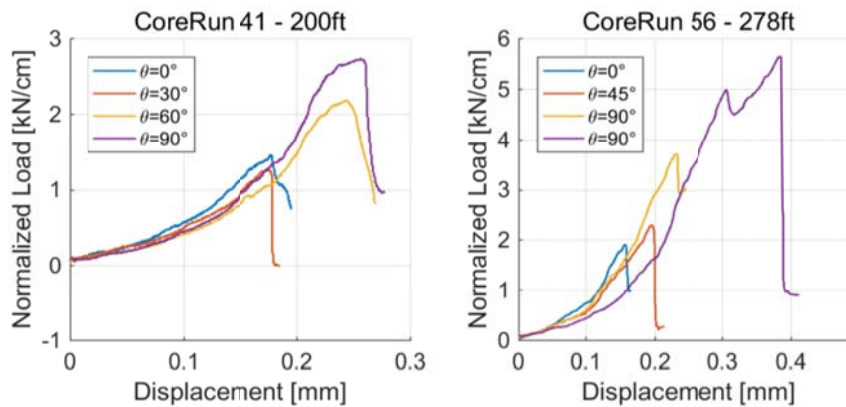
Figure 3.6. Load-displacement curve from Brazilian-disc tests on two groups of samples from cores recovered at 200 ft and 278 ft (61 m and 84.7 m) below the 4850L. The diametric load is normalized by the sample thickness to allow comparison.

3.1.4   Permeability Measurements (LBNL)

The host rock surrounding the kISMET boreholes is very tight (low permeability), with no clearly visible open fractures. Nevertheless, even small amounts of leak-off of injected water from hydraulic fractures into the rock matrix can affect fracture propagation. Therefore, permeability of the in situ rock matrix is

an important control on hydraulic fracturing. The presence of strong rock fabric and anisotropic mechanical and seismic properties suggest that permeability may also be highly anisotropic.

In this task, we will measure permeability using a special experimental setup at LBNL built for very tight, low-permeability rock. We anticipate measuring permeability initially using a gas pressure decay permeameter as sketched Fig. 3.7 from Finsterle and Persoff (1997). In this method, the one-inch diameter sample is placed in an elastomer sleeve between two steel end pieces that are connected by fine steel tubes to small external volumes. One side is pressurized, and at initial time, the valve is opened to the rock core, and pressures on both sides of the core are measured over a long duration. The pressure decay on the higher pressure side and the pressure increase on the low side are than used to compute the permeability, the Klinkenberg parameter, and the porosity. If the permeability is high enough, a steady state method will be used as well. Depending on the results of these tests, alternative techniques may also be used.
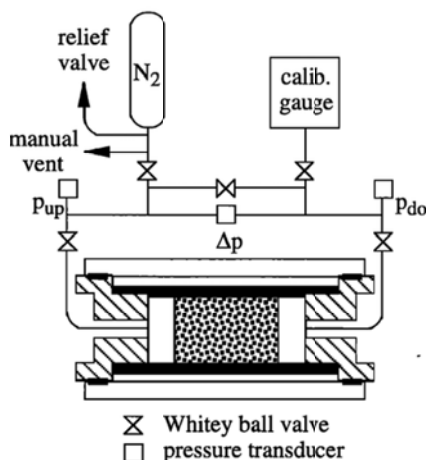
Figure 3.7. LBNL pressure decay permeameter. (Source: Finsterle and Persoff, 1997).

3.2   Mini Hydraulic Fracturing Experiments

Two types of laboratory-scale mini hydraulic fracturing experiments are under way to investigate the importance of rock fabric (anisotropy and heterogeneity) on near-borehole hydraulic fracture generation. The first experiment will be conducted using bi-axially confined cylindrical rock cores. The objective of this experiment is to examine the effect of the rock fabric alone on fracture generation. The second experiment will be conducted using cube-shaped samples subjected to triaxial stresses (principal stresses) that are close to the estimated kISMET in situ stresses. The objective of this experiment is to examine how the combined effect of rock fabric and stress anisotropy alters the hydraulic fracture generation compared to the fabric effect alone.

3.2.1   Thick-Wall Cylinder Fracturing Test—Rock Fabric Effect (Univ. of Wisc.)

Laboratory hydraulic fracturing experiments will be performed in a conventional triaxial apparatus RTR-1000 (GCTS Testing Systems) at the University of Wisconsin-Madison. A section of the whole NQ core from the kISMET in situ stress measurement interval will be cut into 50–75 mm lengths, then a borehole of 1/8–3/8 inch (3.175 mm-9.525 mm) diameter will be drilled parallel to the core axis for fluid injection. Samples will be subject to a biaxial stress state with an isotropic stress comparable to in situ stress magnitudes applied by a confining fluid and axial differential load applied by the loading column pistons.

Water will be injected at a constant flow rate using an ISCO syringe pump to observe the breakdown pressure in this simulated laboratory hydraulic fracturing experiment. Post-experiment samples will be observed either by X-ray CT or by slicing the samples in order to document the fracture geometry and to address the possibility that the foliation has affected the fracture geometry and/or the breakdown pressure. Differential stress magnitude, flow rate, and injected fluid viscosity are potential parameters that will be varied in the tests. Such a parametric study can help identify possible scale effects, which validate the applicability of fracture mechanics principles (Rummel, 1987) and aid comparison with field data.

If enough core segments are present, we also intend to perform similar cylindrical fracturing experiments with varying controlled foliation orientation to systematically observed the influence of foliation orientation on the breakdown pressure and hence the stress measurement interpretations. Preparing a set of samples for such a test appears to be challenging due to the extreme core-scale heterogeneity of the Poorman Formation. We are planning to obtain larger HQ cores with relatively long intervals of consistent lithology and foliation, although these may not necessarily come from the same intervals of the kISMET borehole at which stress measurements were made.

3.2.2   Mini Cube Fracturing Test—In Situ Stress and Texture Anisotropy Effect (LBNL)

Small-scale hydraulic fracturing experiments will be conducted using 1.5-inch cubes cut out of the NQ cores used in the X-ray CT imaging and ultrasonic velocity measurements. The experiments will use LBNL's true-triaxial loading frame including acoustic emission measurement capability (Fig. 3.8). With this setup, maximum principal stresses of ~9950 psi (68.6 MPa, horizontal stresses) and ~47700 psi (329 MPa, vertical stress) can be applied. The acoustic emissions can be monitored and their locations determined using 12 miniature AE sensors embedded in the loading platens.

During the experiment, estimated, anisotropic in situ stresses will be applied to a rock cube which is cut so that the rock fabric is oriented in the desired direction with respect to the principal stress axes. Subsequently, fluid will be injected in a small-diameter (~1/8 inch (3.175 mm) diameter) analogue borehole to induce a hydraulic fracture to determine the breakdown pressure. Once the fracture is generated, the injection pressure will be temporarily reduced, and then increased again to determine the fracture re-opening pressure which will be correlated to the applied minimum horizontal (around the borehole) stress in the experiment.

After the experiment, the orientation and geometry of the induced hydraulic fracture will be examined either non-destructively using X-ray CT and/or ultrasonic waves, or destructively by slicing the rock cube.
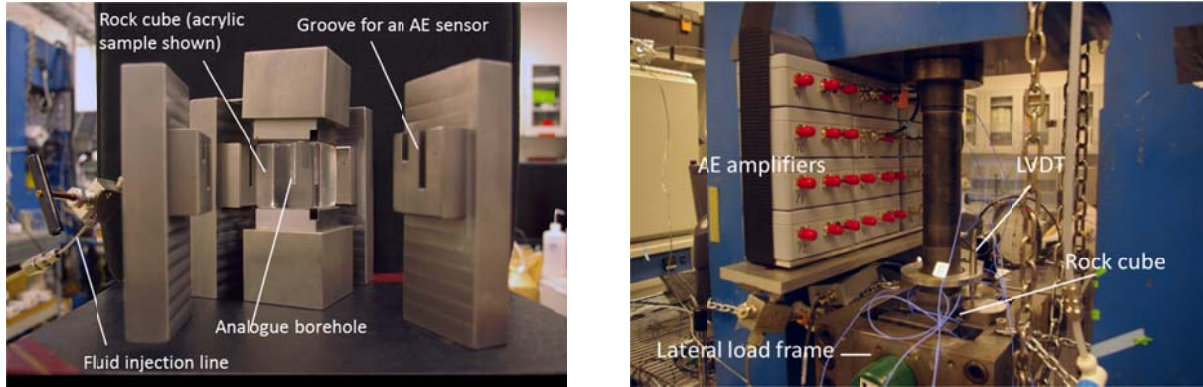
(a) Grooved loading platens for cube samples

(b) Velocity heterogeneity

Figure 3.8. (a) Miniature laboratory-scale hydraulic fracturing experiment using a cube sample. The apparatus allows for three principal stresses to be applied to a rock cube cut out of a core in which a small "borehole" is drilled, injection into which can be used to induce hydraulic fractures. (b) The experiment can be conducted with concurrent monitoring of acoustic emissions.

3.3 Discussion and Conclusions

Laboratory experiments are still in progress at the time of writing this kISMET Summary Report. The preliminary results of rock characterization indicate that the in situ rock at the kISMET site is extremely anisotropic and heterogeneous. This may make it difficult to use small-scale laboratory experiments to help interpret the field test results. In particular, as the "Long core" from the 258.4–259.9 ft interval indicates, local mm-scale foliation planes can intersect the average foliation bands at steep angles due to folding, which results in strong azimuthal anisotropy around the core axis. The complex nature of the rock fabric suggests the behavior of the in situ hydraulic fractures may be affected by local small-scale heterogeneity and fracturing along weak planes (such as mica sheets) that are not aligned with the large-scale foliation planes or the borehole axis. And yet as will be shown in Chapter 5 of this Summary Report, the observed hydraulic fractures in the kISMET field experiments were remarkably uniform in orientation.

The strong heterogeneity makes it difficult to select cube sample orientations (i.e., orientations to cut the cores) based upon the estimated in situ principal stress orientations. This is because the texture on the surface of the cores and the oriented images of the borehole walls are difficult to match up due to significant changes in the rock fabric over the thickness of the coring bit kerf. For this reason, we are currently identifying the core orientations based upon the overall textures resulting from the foliation planes and the orientation of the fold axes. This makes it somewhat easier to match between the core and the borehole wall image than individual features such as foliation bands and mineral-filled fractures.

This page left intentionally blank.

4.   PRE-TEST MODELING AND ANALYSIS

Lead Authors: Hai Huang, Jing Zhou, Earl Mattson, and Thomas Doe

4.1   Introduction

An important part of the kISMET experimental design is the determination of the injection parameters (duration of injection at given flow rate) to produce hydraulic fractures with desired size ranges for their intended purposes. For the stress-measurement fracturing, it was important to assure that the fractures are large enough to be representative of the stress field and produce reasonable stress values, but not so large that they penetrate into the main kISMET experiment volume, which is approximately 40 m (131 ft) below the drift invert (floor) around the five-spot pattern. For the stimulation experiment conducted in the test volume, it was important to create fractures large enough to have a reasonable geophysical signature, but not so large that they would extend significantly beyond the monitoring array.

The second objective of design calculations is to provide an initial conservative estimate of the magnitudes of potential seismic activities induced by the hydraulic fracturing experiments under various injection scenarios. Vibration and seismicity were pointed out as a concern by SURF staff because of potential negative effects on other experiments carried out at SURF.

Both analytical calculations and numerical simulations were used in the project for estimating the fracture size and volume prior to kISMET hydraulic fracturing. In this section, we restrict our presentation to pre-test analysis of the numerical simulation approach, and we bundle presentation of the analytical methods in with post-test analyses of fracture size presented in Chapter 7. The main objective of the pre-test modeling and simulation studies reported here is to provide initial estimates of the fracture sizes (length and height), geometry, breakdown pressure, and fracture propagation pressure in order to inform the design of the hydraulic fracturing experiments. A secondary purpose is to provide some background on numerical simulation of hydraulic fracturing and the specific methods that we used in the kISMET project.

4.2   Methodology of Coupled Network Flow-DEM Model

Hydraulic fracture propagation in crystalline low-permeability rocks is a very complex process, controlled by many factors, e.g., in situ stress state, injection rate, fluid viscosity, and rock heterogeneity across many scales, ranging from mineral fabrics to natural fractures of varying sizes, and mineral fillings. Very often the generated fracture morphology is difficult to monitor and characterize in time during the fracturing experiments in the field through existing diagnostic methods. Thus the development of physics-based hydraulic fracturing models not only provides valuable information to guide fracturing experiment design and monitoring planning, but also helps interpret experimental results and monitoring data. A robust hydraulic fracturing model should at least include the following physics:

(1) stress concentration and redistribution before and during fracture propagation;

(2) pressure dissipation due to viscous flow along discrete fractures and within the formation, and due to leak-off from fractures into formation;

(3) appropriate coupling between fracture opening and fluid flow.

There have been a number of hydraulic fracturing models with varying levels of physics rigor developed using different analytical and numerical approaches (e.g., Economides and Nolte, 2000; Xu et al., 2010; Dahi-Taleghani and Olson, 2011; Wu and Olson 2013). In this project, a coupled network flow and quasi-static discrete element model (DEM) developed by INL called FALCON was applied for pre-test fracturing design purposes because it provides a nice balance between simulation run time and rigor of modeled physics.

The coupled network flow and quasi-static DEM model is briefly described in this section. In the DEM model (Potyondy and Cundall, 2004) as shown in by Fig. 4.1, rock volume is typically represented by an assemblage of randomly generated, non-uniform-sized circular (in 2D) and spherical elements (often referred as particles). The DEM lattice formed by the Delaunay tessellation of the particles, is used to simulate mechanical deformation and fracture propagation. Each edge of the tetrahedral resulting from the Delaunay tessellation represents an elastic beam connecting two adjacent DEM particles. In a quasi-static DEM model with a mechanical load applied, particles will move and rotate into a new mechanical equilibrium stage via a numerical relaxation procedure (similar to successive over-relaxation procedures). The elastic beams between two adjacent particles will be deformed and sustain increasing stretching and shearing forces. Once the shearing and stretching forces of a beam exceed some pre-defined threshold values, that beam will break, mimicking a crack initiation, and the stress will be transmitted into neighboring beams, which are likely to break sequentially, mimicking crack propagation.

During each time step, this beam breaking--relaxation process is repeated a number of times until no more beams break at the given loading level, at which point the simulation progresses to the next time step. Unlike the other DEM-based fracture simulators like PFC2D or PFC3D (from Itasca, Inc.) that are fully dynamic, the hydraulic fracture propagation is treated here as a quasi-static process. The biggest advantage of such quasi-static treatment of the hydraulic fracturing process is that it allows the use of large time steps in the simulation, compared to the fully dynamic approaches in which time-step sizes are limited for stability reasons, i.e., the time-step size has to be smaller than the time required for an elastic wave to travel through one element, which significantly increases simulation run times. Another significant advantage of the quasi-static DEM model is that the beam breaking--relaxation procedure ensures the system will rapidly converge to a global minimum of the free energy of the system for a given load during each time step. In order to account for the local mechanical heterogeneities due to variations of mineral fabrics, random perturbations can be added to the tensile strength, shear strength, and stiffness constant of individual beams. It turns out that the randomness of the beam mechanical strengths, together with the "disordered" DEM lattice, are critical for generating realistic fracture geometry and fracture patterns.
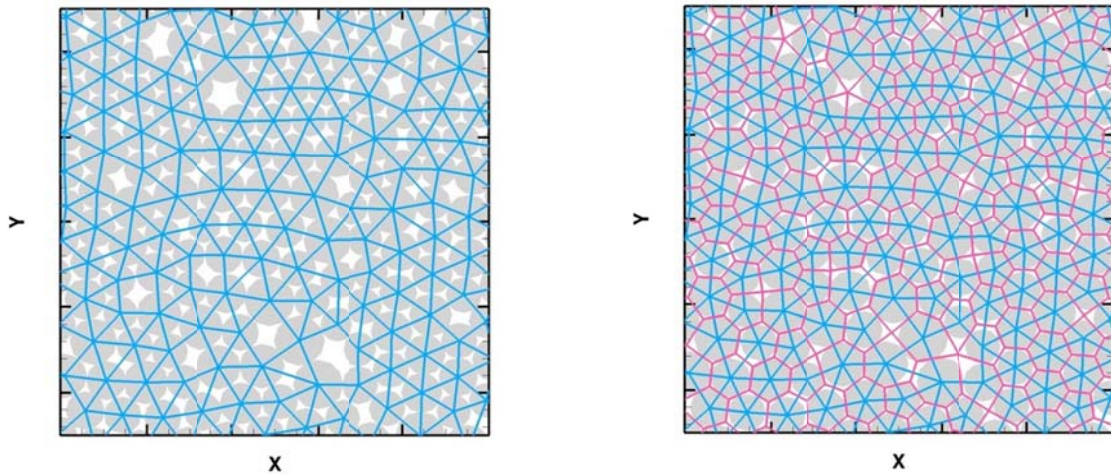
           (a) DEM lattice   (b) DEM lattice coupled with flow lattice

Figure 4.1. The concept and construction of the dual lattice system. In both figures, the grey circles
         represent randomly distributed DEM particles. The blue lines (elastic beams) connecting DEM
         particles represent the DEM lattice. The red lines in (b) are the conjugate flow lattice.

The displacement and rotation of each DEM particle may result from the combined effects of the following forces leading to the formation of hydraulic fractures:

(1) beam force and moment from the connected particles;

(2) viscous damping force;

(3) repulsion by neighboring particles not connected by beams;

(4) interaction between particles and walls;

(5) stress gradient if the stress is not uniform in principal directions;

(6) external force caused by the fluid pressure gradient due to injection.

Fig. 4.2 depicts the force calculation steps used in the DEM model (Zhou et al., 2015). Because this method is quasi-static, the dynamic step with calculation of velocity and acceleration is not required. The Force-Displacement law is used to determine both the translational and rotational motion of each particle and the contact forces after particle displacement.
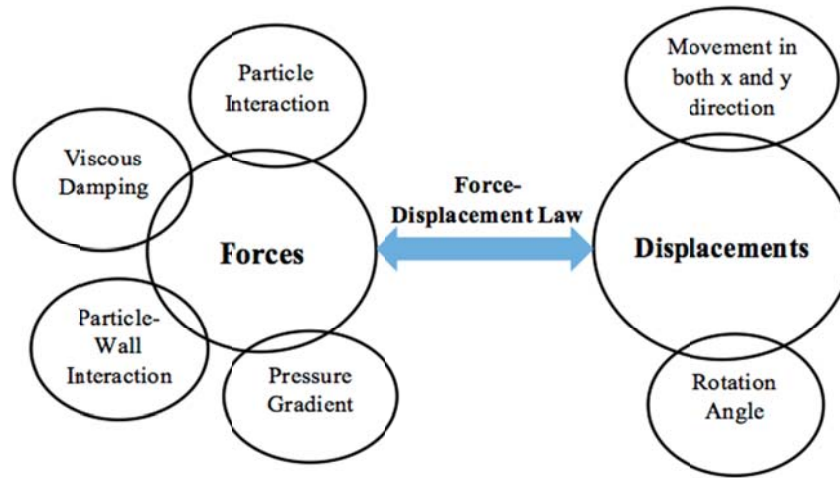
Figure 4.2. The algorithm of quasi-static DEM model.

In the absence of a pressure gradient, the force and moment exerted on a node i by a neighboring node j are given by

$$\vec{F}_{i,j} = k_n \left(d_{i,j} - d_{i,j}^0 \right) \vec{n}_{i,j} + k_s \frac{1}{2} \left(\phi_{i,j} - \phi_{j,i} \right) \vec{s}_{i,j} , \tag{4.1}$$

$$\overline{M}_{i,j} = k_s d_{i,j} \left[\frac{\Phi}{12} \left(\phi_{i,j} - \phi_{j,i} \right) + \frac{1}{2} \left(\frac{2}{3} \phi_{i,j} + \frac{1}{3} \phi_{j,i} \right) \right], \tag{4.2}$$

where $d_{i,j} = \left| \overline{(x,y)}_i - \overline{(x,y)}_j \right|$ is the distance between the centers of two DEM nodes i and j, and $d_{i,j}^0$ is the initial equilibrium (stress free) distance. The rotation angle in the local coordinate frame of the beam is given by ϕ_i. The normal and shear force constants, k_n and k_s, must be calibrated against the desired Young's modulus E and Poisson's ratio ν. The detailed calibration process can be found in Section 4.3.2. In addition, $\Phi = (12\,E\,I)/(G\,A\,d^2)$, in which I is moment of inertia, G is shear modulus, and A is the cross-sectional area of the elastic beam.

Once a mechanical load is applied (the load is imposed by the injection of fluids in this case), an over-relaxation algorithm is used to relax the DEM network to a new state of mechanical equilibrium in which the net forces and moments are zero for all of the DEM particles. If a beam satisfies the von Mises failure criterion given by

$$\tau = \left(\frac{\varepsilon}{\varepsilon_c}\right)^2 + \frac{\max\left(\left|\phi_{i,j}\right|, \left|\phi_{j,i}\right|\right)}{\phi_c} > 1,$$

(4.3)

it will be irreversibly removed from the DEM network, giving rise to crack initiation and growth. Here ε is the longitudinal tensile strain of the beam, and ε_c is the critical longitudinal tensile strain (the maximum tensile strain that the bond can sustain), and ϕ_c is the critical rotational angle above which the beam will break, even in the absence of tensile strain. Typical values for ε_c and ϕ_c (dimensionless) range from $\sim 10^{-3}$ to $\sim 10^{-2}$ for rocks and many other polycrystalline brittle solids. This criterion can simulate both tensile- and shear-induced rock failures.

In order to couple fluid flow with the DEM model while appropriately accounting for viscous pressure dissipation along fractures (approximated by Couette flow between parallel plates) and through the formation (Darcy flow) due to leak-off of hydraulic fracturing fluids, a conjugate flow lattice is constructed based on the DEM lattice, as illustrated in the 2D example of Fig. 4.1(b). Conjugate nodes are assigned to the centers of polygons (2D DEM lattice) and tetrahedrons (3D DEM lattice). The flow lattice is formed by connecting the neighboring conjugate nodes. Assuming Darcy flow is valid, the governing equation for fluid flow is

$$\frac{\partial(\zeta\rho_f)}{\partial t} = \nabla\left(\frac{\rho_f k}{\mu}\nabla p\right) + Q,$$

(4.4)

where ζ is the porosity of the porous medium, ρ_f is the density of the injected fluid, k is the formation permeability, μ is the fluid's dynamic viscosity, p is the pressure, and Q is the injection rate. Fluid pressure at each conjugate flow node is updated during each time step. Any pressure alteration will exert additional force on the neighboring DEM particles as equivalent body forces through the following equations

$$\vec{F}_{i,j} = k_n\left(d_{i,j} - d_{i,j}^0\right)\vec{n}_{i,j} + k_s\frac{1}{2}\left(\phi_{i,j} - \phi_{j,i}\right)\vec{s}_{i,j} - \nabla p \cdot \pi r^2,$$

(4.5)

$$\overline{M}_{i,j} = k_s d_{i,j}\left[\frac{\Phi}{12}\left(\phi_{i,j} - \phi_{j,i}\right) + \frac{1}{2}\left(\frac{2}{3}\phi_{i,j} + \frac{1}{3}\phi_{j,i}\right)\right].$$

(4.6)

It is important to note that before a crack is initiated, the coupled network flow-DEM model reproduces the conventional poroelasticity effect. When an elastic beam breaks, a more conductive flow channel will be generated which connects the two associated fluid nodes of the flow network with a new permeability in the form of

$$k \cong \frac{b^2}{12}$$

(4.7)

where b is the aperture of the fracture (same as the separation distance of the two neighboring DEM particles that have been "cleaved," a direct output of the DEM model). The new permeability will replace the original value and is used in the pressure simulations. The leakage from fractures into adjacent porous matrix is accounted for by connecting the flow nodes along the fractures with the flow nodes within the porous matrix, unlike most other boundary element models that typically only account for fluid flow

along fractures. This unique feature allows FALCON to evaluate the leakage of fracturing fluid into the porous matrix.

The simulation of the coupled network flow-DEM processes consists of interleaved fluid flow, mechanical relaxation of the DEM network, and beam-breaking steps. During each time step, the new fluid pressure field (in both fractures and matrix) is obtained first by solving Eq. 4.4. Then the new fluid pressure field is applied to the DEM network according to Eqs. 4.5-4.6, and the DEM network is relaxed to a new mechanical equilibrium. The beam that most exceeds the failure criteria, which is usually near a crack tip, is then removed from the DEM network and the network is again relaxed into a new state of mechanical equilibrium. The mechanical relaxation and beam-breaking are repeated a number of times during each time step, mimicking crack initiation and propagation, until no additional beam-breaking occurs, at which point the simulation proceeds to a new time step. This quasi-static approach to modeling hydraulic fracturing is reasonable because stress build-up and relaxation associated with hydraulic fracture propagation often exhibits quasi-static behavior.

4.3   Model Calibration

4.3.1   Calibration Parameters

The DEM model parameters, normal force constant (k_n), shear force constant (k_s), critical tensile strain (ε_c), and critical rotational angle (ϕ_c) must be calibrated to accurately represent the mechanical properties of brittle rocks such as Young's modulus (E), Poisson's ratio (ν), tensile strength (σ_T) and compressive strength (σ_c) (Huang and Mattson, 2014). Tables 4.1–4.2 list the geological and operational parameters chosen for pre-fracturing test simulations, based on the results of Vigilante (2016) who summarized current knowledge of stresses and rock mechanical properties at the SURF site.

Table 4.1. Rock properties and operational parameters used in the simulations.

Parameters	Value
Young's modulus (GPa)	41
Poisson's ratio	0.23
Shear modulus (GPa)	17.9
Density (g/cm^3)	2.95
Uniaxial compressive strength (MPa)	115
Uniaxial tensile strength (MPa)	14
Formation permeability (nanoDarcy)	10
Formation porosity	0.06
Injection rate (liter/min = lpm)	2.0
Injection fluid viscosity (Pa s)	1.0×10^{-3}

Table 4.2. Estimated in situ principal stresses from compilations of Vigilante (2016).

Principal Stress	σ_v	σ_{HMax}	σ_{HMin}
Value (MPa)	44	30.35	25.07

4.3.2   Parameter Calibration

The calibration of DEM model parameters is performed by simulating a uniaxial tensile test, as shown in Fig. 4.3. Because the hydraulic fracture opening and propagation are mainly driven by the tensile failure at the fracture tip caused by increased pore pressure, we calibrate the DEM to Young's modulus, Poisson's ratio, and tensile strength.

The dimensionless force constant k_n was selected from a random Gaussian distribution with a mean of $\mu = 1.0$ and a standard deviation of $\sigma = 0.1$. A constant k_s/k_n ratio of 0.3 was used in the parameter calibration. The force constant k_n and k_s/k_n jointly determine the macroscopic Young's modulus and Poisson's ratio. The critical tensile strains ε_c of the beams were selected randomly from a Gaussian distribution with a mean of $\mu = 1 \times 10^{-3}$ and a standard deviation of $\sigma = 1 \times 10^{-4}$. The critical tensile strain determines the macroscopic tensile strength of the rock. During the numerical uniaxial tension test, DEM particles near both ends move uniformly in opposite directions at a specified strain rate in order to mimic uniaxial tensile loading conditions. At each loading stage, the average axial stress and lateral strain within the sample were calculated by volume averaging in order to generate the stress-strain curve.

Fig. 4.3 shows the simulated stress-strain curves for the uniaxial tensile test. The simulated rock sample behaves like a linear elastic solid before the load reaches its peak failure value corresponding to the linear parts of the stress-strain curves. When the load reaches its peak (failure) value, the sample fails suddenly and stress is released rapidly. This brittle behavior is typical for crystalline rocks. The stress-strain curve gives the dimensionless Young's modulus (average slope of the linear parts of the curve) of $E_0 = 2.0$. The simulated sample has a macroscopic dimensionless critical tensile stress of 1.43×10^{-3}. The dimensionless critical tensile stress can then be rescaled to the dimensional macroscopic, measureable tensile strength of the rock through Eq. 4.8. The tensile strength used in the model for pre-test simulations is higher than the reported value from the literature (~15 MPa) in order to provide initial conservative estimates of the breaking pressure. We plan to calibrate the model using laboratory core test data in the future.

$$\sigma_T = \frac{E}{E_0}\sigma_{T0} = \frac{41.3\,GPa}{2.0} \times 1.43 \times 10^{-3} = 29.3\,MPa \tag{4.8}$$
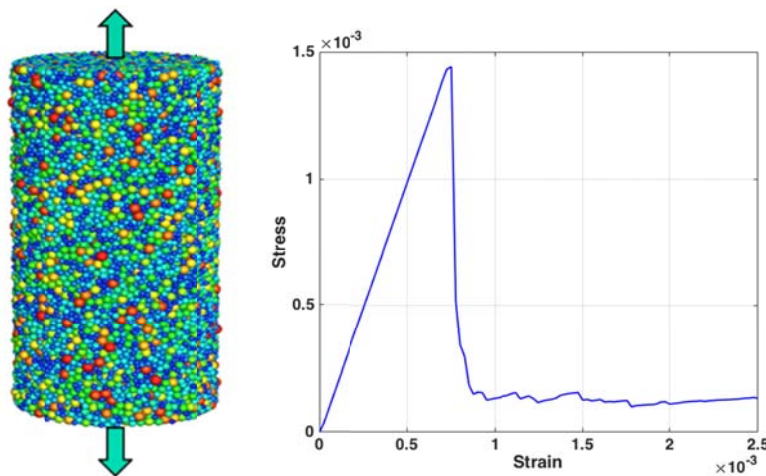
Figure 4.3. Numerical uniaxial tension test: (left) the DEM model used in the test (color scales with particle size) and (right) simulated dimensionless stress-strain curve for the uniaxial tension test.

4.4   Pre-Test Simulation Results

In the pre-test simulations, we assumed that the rocks are homogeneous in a statistical sense (local variations of beam stiffness, and tensile and shear strengths are included via random perturbations), isotropic, and the model domain size is chosen to be 50 ft × 50 ft × 30 ft, (15.24 m on a side) as shown in Fig. 4.4. An open vertical wellbore is located at the center of the model domain and penetrates the whole depth (red cylinder) with a diameter of 1 ft (0.3048 m). Only the middle part of the vertical well (green zone) of height 3 ft (0.91 m) takes the fluid injection with the rate of 2 L/min. The overburden stress (σ_v) is oriented in the *Z*-direction, the maximum compressive horizontal stress (σ_{Hmax}) is oriented in the *Y*-direction. The values of in situ stresses used in the simulations are given in Table 4.2. A total of 118,634 DEM particles of variable sizes, ranging from 0.4 ft to 0.6 ft (0.12 m to 0.18 m) were randomly generated and packed into the model domain to form the DEM lattice and associated conjugate flow network. The permeability of the rock is 10 nanoDarcy (1.0×10^{-20} m^2), representing an ultralow-permeability formation.
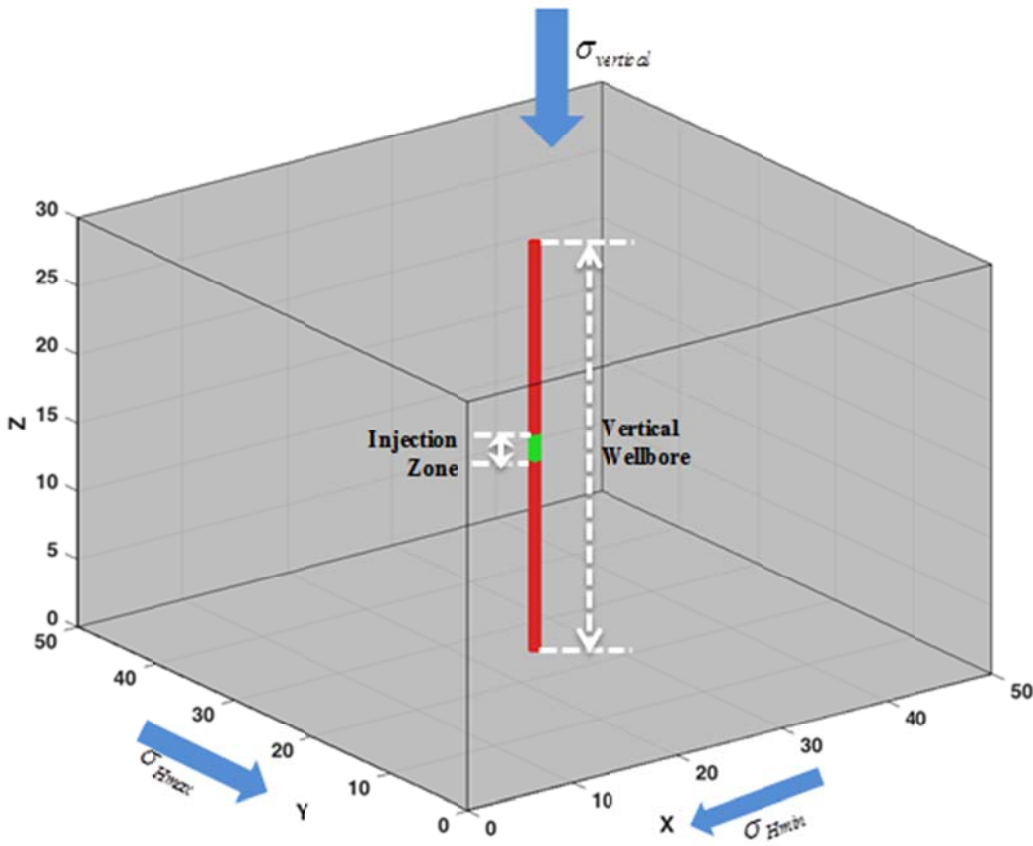
Figure 4.4. Simulated domain with a vertical open wellbore.

Fig. 4.5 shows the simulated fracture propagation process with time. As the fluid injection starts, the pressure in the wellbore begins to rapidly build up due to the low compressibility of water. Once the wellbore pressure is large enough (~35 seconds after injection starts, or equivalently, after ~1.17 L of injection have occurred) to break the beams between DEM particles adjacent to the wellbore, a nearly vertical fracture is initiated and starts to propagate (Fig. 4.5b). One important observation worth mentioning is that once the fracture starts to initiate, it will "pop-open" a crack with a relatively large

radius initially, ~1.2 m, with an average aperture of ~2.0×10^{-4} m. These predicted values are similar to analytical calculations presented in Chapter 7. Due to the local mechanical heterogeneity incorporated into the model, the initial crack does not assume an ideal bi-wing penny shape, but rather it exhibits some asymmetry. As more fluid is injected, the crack continues to propagate more or less along the horizontal maximum compressive stress direction (*Y*-axis in the simulation) and eventually grows into a penny shape (see Fig. 4.5c - Fig. 4.5d). Unlike the uniform crack-front growth, the simulated growth of the crack front at any given moment is actually non-uniform, with some parts of the crack front growing and the rest periodically static. The uniform growth concept is valid only in a statistical sense during the late stages of crack propagation. Also, because there is randomness introduced into the mechanical properties of beams, the fracture propagation is not perfectly symmetric at both sides, which is realistic for natural rock considering the heterogeneity in the subsurface environment. The generated crack surface versus injected fluid volume is summarized in Table 4.3. The crack radius matches with the analytical solution described in Chapter 7. The numerical model result shows a similar trend to the analytical solution for fracture radius vs. injection volume.

(a) $t = 0$ s

(b) $t = 35$s

(c) $t = 145$ s

(d) $t = 345$ s
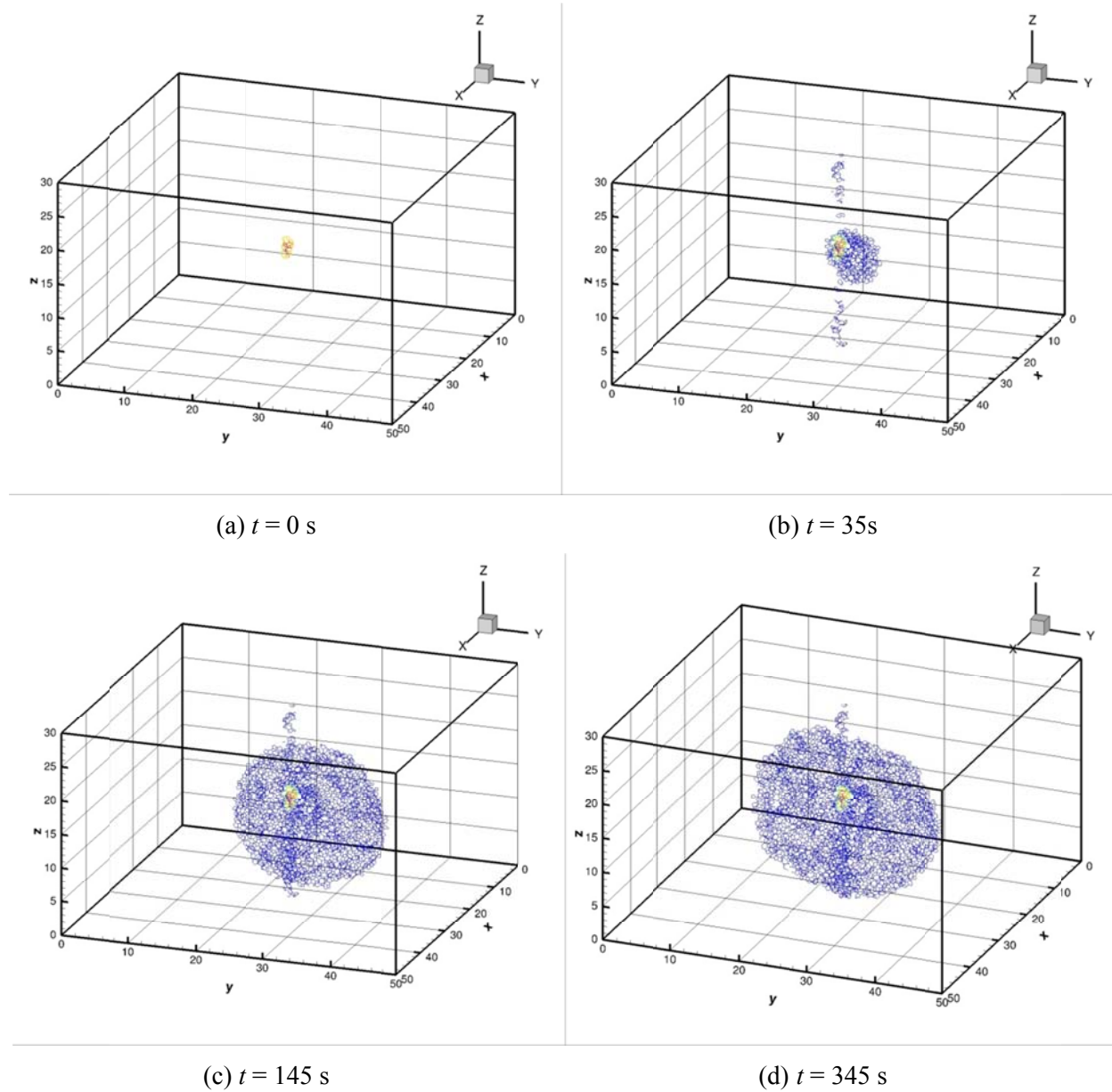
Figure 4.5. Induced fracture geometry at different times. The color scales with the hydraulic diffusivity (warm and cool colors = high and low hydraulic diffusivity, respectively). Notice that the initial large hydraulic diffusivity within the injection zone, and the trend of reducing hydraulic diffusivity (equivalent to crack aperture) from near wellbore to the crack front.

Table 4.3. Generated fracture radius versus injection time and volume.

Injection Time (s)	Injection Volume (liters)	Crack Radius (m)
35 (Fig. 4.9(b))	1.17	1.21
145 (Fig. 4.9(c))	4.83	3.35
345 (Fig. 4.9(d))	11.5	4.26

The observed fracturing pattern is further elucidated by examination of the stress field in the crack plane as depicted in Fig. 4.6. The stress component S_{xx} shown here is actually the stress normal to the average crack plane (YZ plane). Note that we use a positive value for tension and negative value for compression (in contrary to the common geomechanics convention). There is a nearly circular ring with concentrated tensile stress, which actually represents the crack front, with a compressive stress zone within due to fluid pressing against the opened crack surfaces. It is these concentrated tensile stresses near the crack front that drive fracture propagation. It is obvious that the stress concentrations along the crack front are not uniform, due to the local variations of mechanical properties. Therefore the growth of the crack front is very much similar to the process of a moving contact line with random "pinning" and "de-pinning," which is a critical feature in order to generate episodic "bursts" of microseismic events.
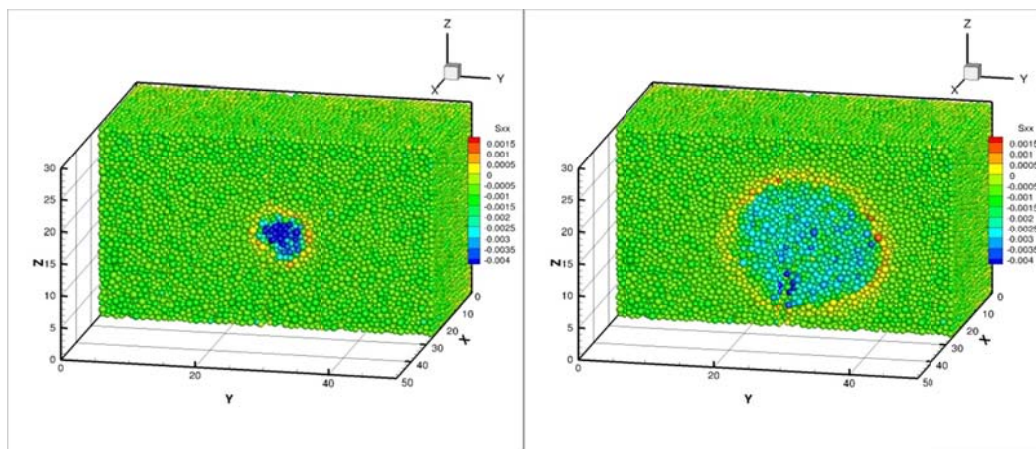
Figure 4.6. Dimensionless stress S_{xx} normal to the average crack plane during early (left) and (late) crack propagation stages.

Fig. 4.7 shows the wellbore pressure evolution with injection time. From the simulation results, we observe that the fracture will start to propagate when the pressure reaches the peak defined by the breakdown pressure, and then it will propagate with a stable, reduced pressure called the propagation pressure. The estimated breakdown pressure is 66.78 MPa, and the estimated propagation pressure is 29.91 MPa. According to the literature (Yew, 1997), the breakdown pressure from analytical solution is:

$$P_b = 3\sigma_{Hmin} - \sigma_{Hmax} + T - P_0 = 3 \times 25.07 - 30.35 + 29.3 = 74.16 \; MPa \tag{4.9}$$

(with assumption of zero pore pressure (P_0)) which is very close to the predicted breakdown pressure by the numerical simulations with the given initial in situ stress conditions. Note that as used in this report, $\sigma_{HMin} = \sigma_{Hmin}$, and $\sigma_{HMax} = \sigma_{Hmax}$). However, due to a relatively large rock tensile strength value used in these pre-test simulations (carried out when did not know tensile strength at the kISMET site), this

predicted breakdown pressure provides an upper bound for wellbore breakdown pressure. In the simulated wellbore pressure vs. time curve, there is a rapid pressure decrease at ~35 seconds after the propagation starts, corresponding to the initial crack opening (a sudden increase in fracture volume to allow compressed fluid to rapidly expand). As the crack propagates farther, the fluid pressure needed to maintain crack growth decreases. According to fracture mechanics, a critical stress intensity value at the crack front (as a result of stress concentration at the crack front) needs to be reached and maintained in order to keep the fracture propagating. Because the stress intensity factor at the crack front is proportional to the square root of crack length, a smaller fluid pressure acting against fracture walls is needed to maintain a critical stress intensity value as the crack length increases.
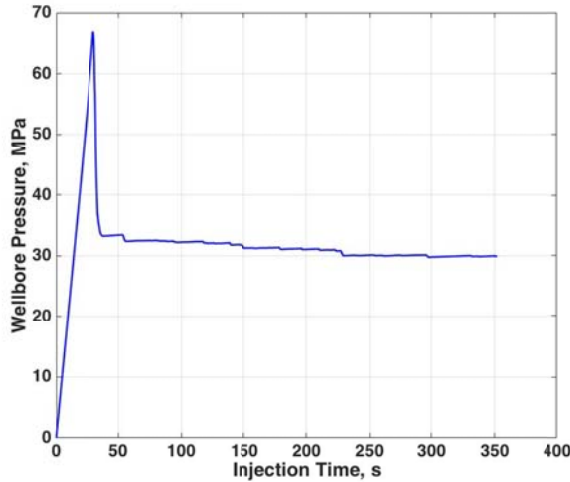
Figure 4.7. Wellbore pressure versus injection time.

4.5   Released Energy

When the initial in situ stress is applied in the model, strain energy is stored in elastic beams that connect DEM particles. As a crack initiates and starts to propagate, the beams will break due to the fluid injection and increase of pore pressure to model fracture initiation and growth. When this happens, the strain energy stored in the elastic beams will be released and partially converted into heat, partially absorbed by the neighboring DEM particles (via pressure-volume work), and partially radiated as elastic waves (i.e., as seismic waves) (Hazzard and Young, 2002).

One important concern that was raised by other the physics experimental groups at SURF was how large the microseismicity would be from the hydraulic fracturing at kISMET. Our DEM numerical simulations are capable of providing an estimate of this released energy. Therefore, one of the goals of the pre-test simulations was to provide an initial estimate of the magnitude of induced seismic events related to hydraulic fracturing at kISMET. The DEM model calculates the elastic strain energy released from the broken beams during simulated fracturing. Assuming each beam breakage is a single seismic event, and all elastic strain energy stored in the beams prior to breaking is used in generating earthquakes, the DEM model provides a very conservative estimate of the potential seismic magnitude.

Fig. 4.8 gives a spatial-temporal map of the simulated seismic events and associated energies released. The events are colored according to time and sphere sizes are proportional to the event magnitudes. One general trend observed is that these simulated events are consistent with the crack propagation process, with earlier events closer to the wellbore, and later events farther away from the wellbore. Arguably, some earlier events with large energy releases are associated with initial crack opening and close to the

wellbore. However, some large events far away from the wellbore are also observed during the late time. In general, the majority of the events are relatively small.
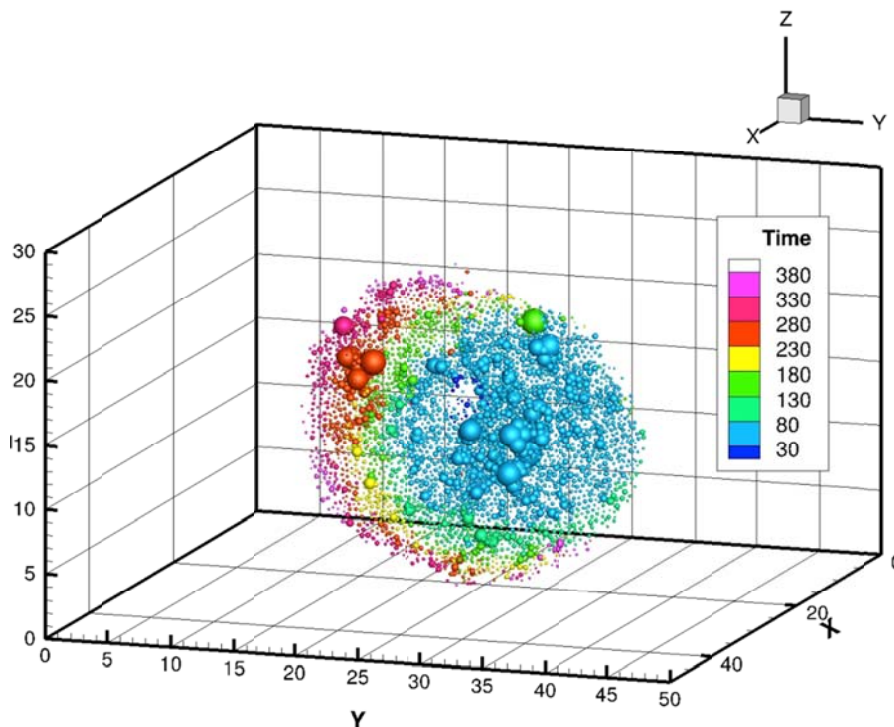
Figure 4.8. Seismic events generated by the coupled network flow-DEM model. The color of each sphere represents time and the size of sphere is proportional to event magnitude.

While the exact locations of individual events in the DEM model are meaningless because of the random perturbations added to the beam mechanical properties and the disordered DEM lattice that is used, the statistical temporal analysis of the released energies of individual events and cumulative released energy associated with fracture are more meaningful. Fig. 4.9 shows the event energy release vs. injection time. We grouped the individual events during each time step into a single equivalent event. The largest energy release happened at the initial fracture opening stage, which has the most beam breakage events. After the initial opening, the fracture propagates smoothly (on average) under constant rate injection, with a few relatively large events (spikes shown in Fig. 4.9). The total energy released during the 345 seconds of injection is 0.37 MJ, and the average released energy of each event is 96.9 J. The episodic bursts of events during the injection are actually a unique feature arising from incorporating local heterogeneity into the model.

The moment magnitude (M_w) associated with the events can also be calculated by the following formula (Hazzard and Young, 2002)

$$M_w = \frac{2}{3}\log M_0 - 6 \qquad\qquad (4.10)$$

where M_0 is a single moment tensor which is calculated by the change in contact force and the relative distance between the originally connected DEM particles. Fig. 4.10 shows the histogram of the event magnitudes. It is clear that the majority of the events are very low-magnitude events, with a few outlier larger events with magnitude of ~ -4 (too small to be of any concern in terms of induced seismicity).
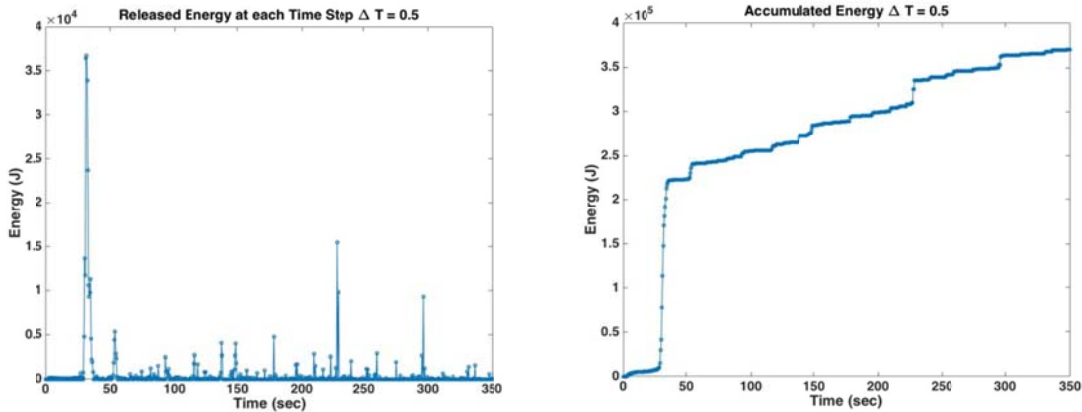
Figure 4.9. (Left) released energy vs. injection time and (right) cumulative released energy vs. time.
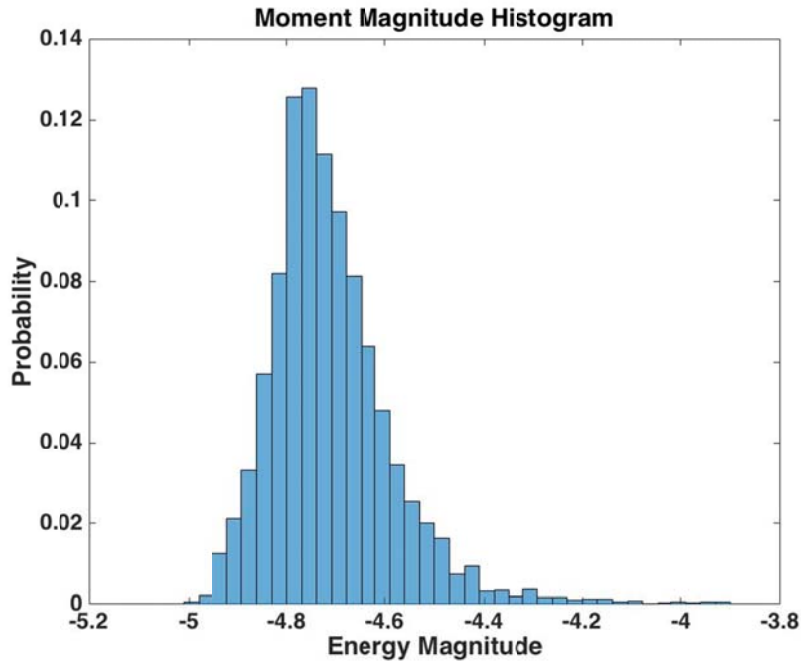
Figure 4.10. Histogram of the moment magnitude generated by the coupled network flow-DEM model.

There is a well-known Gutenberg-Richter magnitude-frequency law that expresses the probability of a seismic event with magnitude equal or great than M in the form of $\sim 10^{-bM}$, where b is often referred as seismic b-value. Fig. 4.11 shows the log-probability of the simulated seismic events with magnitude equal or greater than M versus the magnitude M. It is extremely interesting that the simulated magnitude-frequency curve follows a similar power-law scaling behavior, which suggests that the coupled network flow-DEM model has captured important physics of the hydraulic fracturing process.
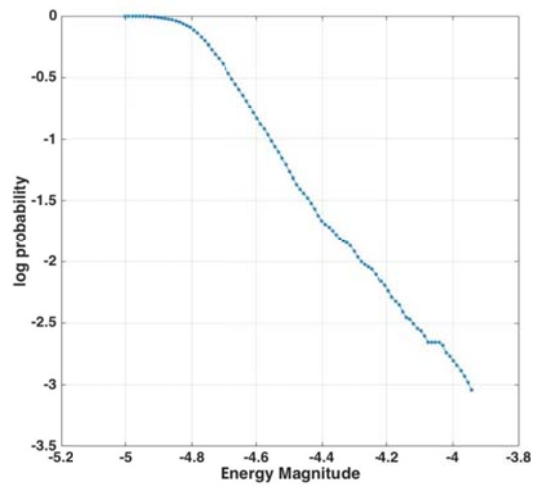
Figure 4.11. The cumulative distribution function and log(probability) of energy magnitude.

5.   STRESS MEASUREMENT AND STIMULATION

Lead Authors: Herb Wang, Moo Lee, Thomas Doe, Bezalel Haimson, Hiroki Sone, Mathew Ingraham, Neal Lord, and Peter Vigilante

5.1   Introduction

The University of Wisconsin-Madison, Sandia National Laboratories, and Lawrence Berkeley National Laboratory conducted hydraulic fracturing and stimulation experiments as part of kISMET project sponsored by the U.S. Department of Energy (DOE) SubTER (Subsurface Technology and Engineering Research, Development and Demonstration) cross-cut initiative. The kISMET experiments meet objectives in SubTER's "stress" pillar and the "new subsurface signals" pillar by testing the monitoring of fracturing by active seismic, electrical resistivity tomography, and passive microseismic monitoring. The kISMET facility is located at the 4850L in the West Access Drift near the Davis Campus of SURF (Fig. 5.1). The tests were conducted in the central hole, kISMET-003 (aka K3, K03, and K003). The borehole is vertical with a 7.6 cm (3 in) diameter and 100 m (328 ft) length located in the zone of Precambrian metamorphic phyllite.

A broad objective of the project was to define the in situ state of stress at SURF because questions have arisen from the large variability in previous stress measurements. What is the source of the stress variability? Is it rock heterogeneity and/or anisotropy? Is it the influence of excavations? Is it related to the scale of the overcoring measurement technique? These issues are important to understand in terms of larger SubTER goals of controlling the geometry of a "designer" fracture network and induced seismicity. A further motivation was to interpret image logs from 1654 meters (5400 ft) of continuously-cored, sub-horizontal borehole that were part of geotechnical studies at SURF under its previous name (Deep Underground Science and Engineering Laboratory, or DUSEL). The image logs showed widespread breakouts having variable intensities and orientations in different boreholes and different portions of boreholes. They represent a valuable source of data to understand how stresses vary at different spatial scales within the underground (Lucier et al., 2009), which is discussed in Chapter 8. Their quantitative interpretation, however, requires a well-characterized minimum horizontal stress magnitude and direction.

The organization of this chapter is as follows. First, we summarize previous measurements of stress at SURF. Next we describe the test equipment and experimental procedures that we used at kISMET to measure stress by hydraulic fracturing; these methods closely follow the International Society of Rock Mechanics (ISRM) protocol described by Haimson and Cornet (2003). Then we present the measured stress test data and their interpretation for the minimum horizontal stress magnitude and direction. Following this, we present results from the stimulation phase during which fracture growth was controlled via low-flow injection rates. The associated CASSM and ERT monitoring experiments are presented in Chapter 6. Finally, the relationship of the kISMET results to regional stresses is discussed.
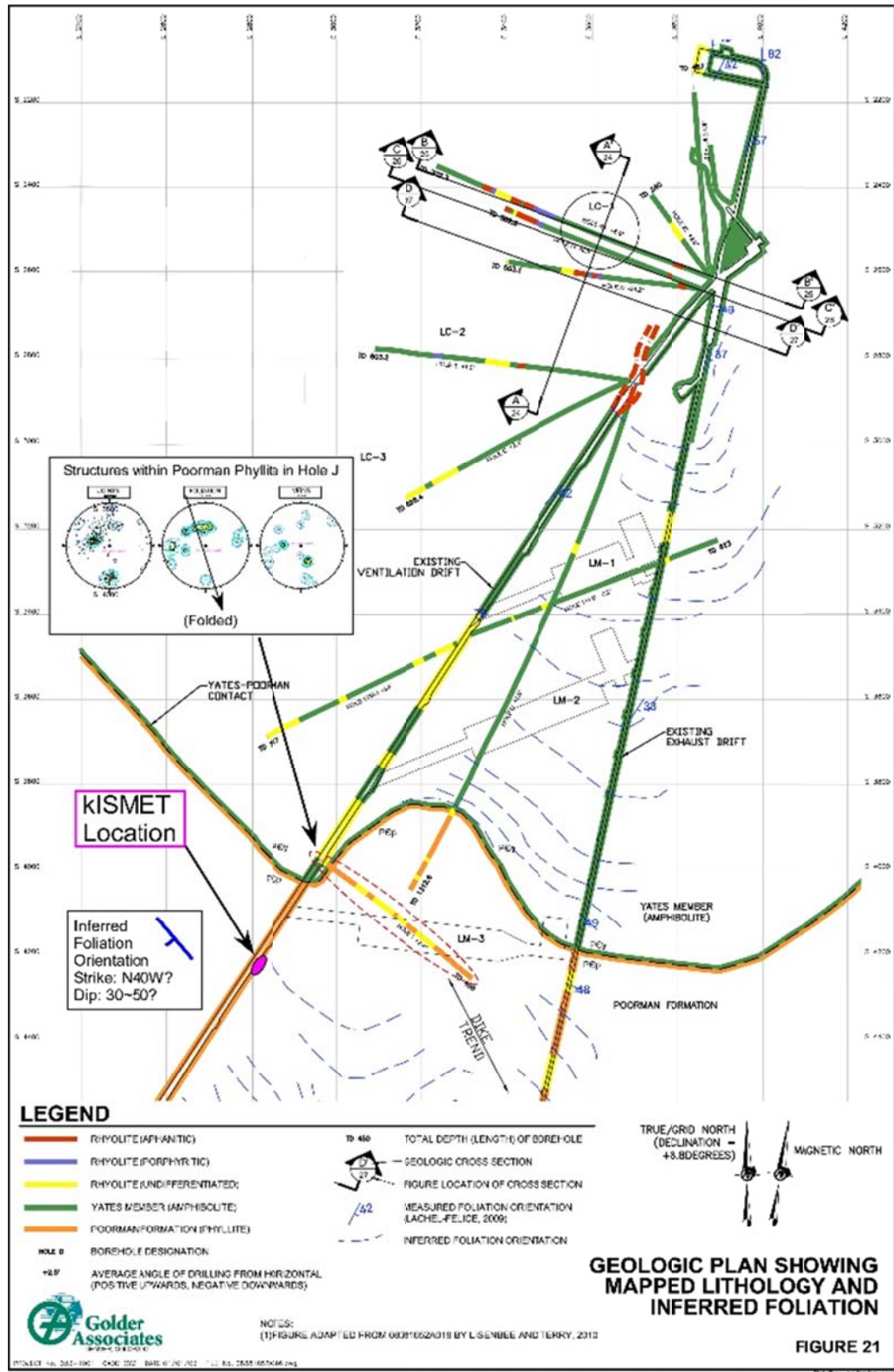
Figure 5.1. Location of kISMET test site at SURF.

5.2   Previous Work

The prior characterization of in situ stress at SURF was initiated in 1970 followed by measurements at multiple levels in each of the following three decades. Significant new research on stresses was conducted in the 1980's by Pariseau (1986) in studies associated with Vertical Crater Retreat (VCR) mining in the vicinity of the Ross Shaft in the 1980's and again in the 2000's when plans were being developed to excavate large caverns at the 4850L as part of the DUSEL project. A benchmark, mine-scale reference stress-magnitude model was proposed by Pariseau (1986) based on his compilation of about half a dozen stress measurements made prior to 1985 resulting in the following estimates of stress and function of depth (z):

$$\sigma_v = 28.28\,z$$
$$\sigma_{HMax} = 14.317 + 11.99\,z \qquad\qquad (5.1)$$
$$\sigma_{HMin} = 0.834 + 12.44\,z$$

where the units of stress and depth are MPa and km, respectively. The measurements scatter widely relative to the linear relations as shown in Fig. 5.2. The measurements might have been affected by rock heterogeneity and/or anisotropy or by stress concentrations associated with mining excavations and thus might not sample the unperturbed stress field. The ratio of maximum-horizontal-to-vertical stress is between 0.6 and 0.9 and the ratio of minimum horizontal stress to vertical stress is between 0.36 and 0.6. The pore pressures could not have been representative of fully saturated pores at the measurement sites because the hydrostatic pore pressure gradient of 0.01 MPa/m would mean the pore pressure at 2255 m (7400 ft) depth exceeds the minimum horizontal stress.
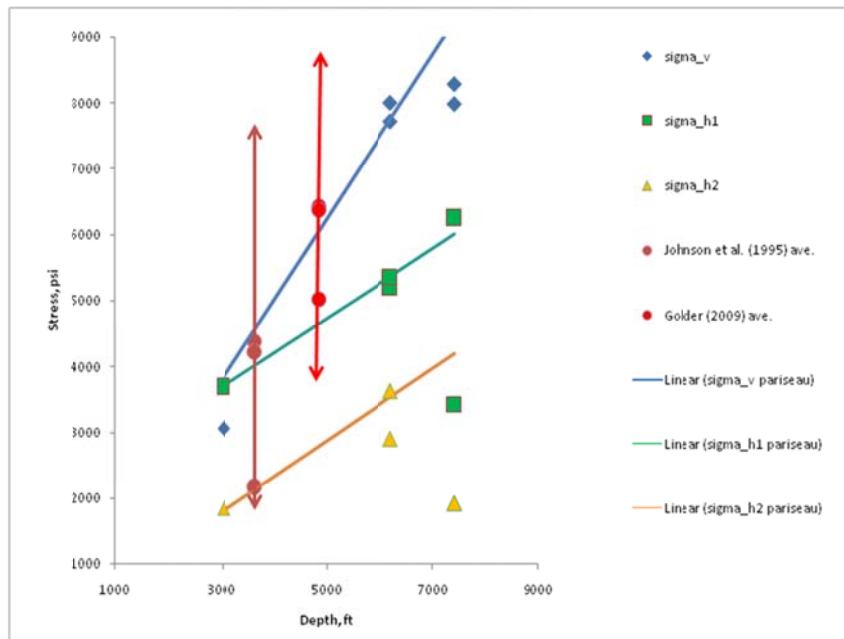
Figure 5.2. Legacy and recent stress magnitudes. The arrows at 3600 and 4850 ft (1097 and 1478 m) depth span the range of measured values while the symbols represent the averages for each principal stress.

As part of the DUSEL project, Golder Associates (2010) reported on eight CSIRO hollow inclusion (HI) cell stress measurements made in three different sub-horizontal holes along the 4850L West Access Drift. The measurements were made typically at a depth of approximately seven meters from the collar in sub-horizontal boreholes. Six of the measurements were in amphibolite and two were in a rhyolite dike. Stress values ranged from close to 62 MPa (9000 psi) for the largest stress and 24 MPa (3500 psi) for the smallest. The average maximum and average intermediate stresses were approximately equal at 43.4 MPa (6300 psi) and the average minimum stress was close to 34.5 MPa (5000 psi). The averages of the maximum and intermediate principal stresses lie close to Pariseau's σ_v regression line while the average of the least principal stress lies close to Pariseau's intermediate principal stress line. The lowest measured stress lies above Pariseau's minimum principal stress line. In average, the ratio of maximum-to-minimum principal stress is fairly low, about 1.3. In summary, as shown in Fig. 5.3, the eight measurements were highly variable in both direction and magnitude of horizontal stress in amphibolite, and apparently less variable in rhyolite intrusions, but this is based on only two measurements. Rock heterogeneity, proximity to the drift, or measurement difficulties are possible explanations for the results. Laboratory testing suggests that the amphibolite could be elastically variable at scales of centimeters (Mellegard et al., 2010). Taken as a whole the amphibolite measurements produce average values that are consistent with expectation based on overburden thickness, and the horizontal stresses are within ranges that are not surprising for their geologic setting. Nonetheless, the state of stress is highly uncertain based on these eight HI measurements.
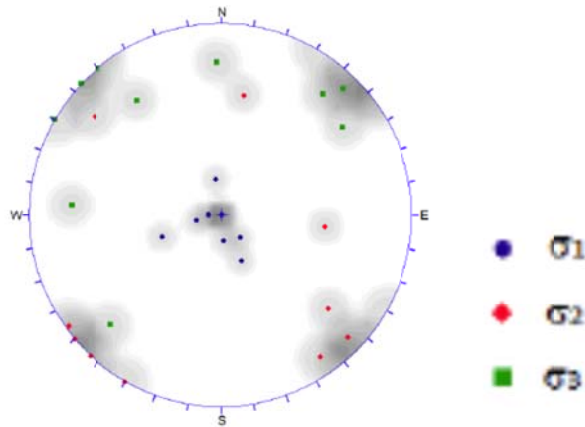
Figure 5.3. Historical and recent principal stress directions on a lower hemisphere projection (from Golder Assoc. 2010, Plate 2.20, p. 53).

5.3   Equipment

5.3.1   Wireline Hydraulic Fracturing System

We used a fast and continuous tool-tripping wireline hydraulic fracturing system for in situ stress measurements and fracture stimulation at kISMET. The wireline hydraulic fracturing system consists of two major downhole tool assemblies: a straddle packer assembly for fracture initiation and extension within the selected test zone, and an impression packer orienting tool assembly for fracture delineation (Fig. 5.4).

5.3.2   Straddle Packer

The wireline straddle packer assembly consists of three major components: (1) two inflatable packer elements; (2) a hydraulic fracturing interval spacer; and (3) a top adaptor for connecting a wireline and hydraulic lines. The packer element consists of a high-pressure inner tube and a braided or ribbed steel reinforced outer rubber cover. The straddle packer incorporates two separate mandrels with a rigid interval spacer. This arrangement enables the interval spacer to be flush with the packer elements, and prevents tensile failure by splitting of the interval spacer when very high pressures are required to fracture the test zone. The assembly is tripped in the borehole on a wireline operated by a hoist.

The top straddle packer adaptor accommodates one hydraulic line to both packers, two parallel hydraulic lines to the hydraulic fracturing interval, and a port to a downhole release valve (Figs. 5.4 and 5.5). We used the two parallel hydraulic lines for interval pressurization and monitoring. One line is connected to the pressure generator to supply fracturing fluid and pressure to the fracturing interval. The other parallel line is connected to the surface pressure transducer for monitoring the interval pressure without friction loss. The monitoring line accurately provides the interval pressure minus the hydrostatic head between the surface and the test zone.

After each test, the packers are deflated by releasing the packer pressure. The pressure relief valve is a normally-open valve consisting of a conically shaped piston and a spring acting against the piston. During tool tripping to the test depth, the normally-open relief valve allows the packers and all hydraulic lines to be filled with the water in the borehole. During packer inflation, fluid is partially blocked by the small venting holes drilled inside the piston, and pressure accumulates on the inlet side. The pressure differential thus created eventually closes the relief valve. When the pressure is dropped at the conclusion of a test by venting the pressure line on the surface, the spring will push the piston to its normally-open position and the pressure will be released to a level equal to the water head. This facilitates the deflation of packer elements. The fracturing tool can be reset at a different depth in the hole without retrieval.
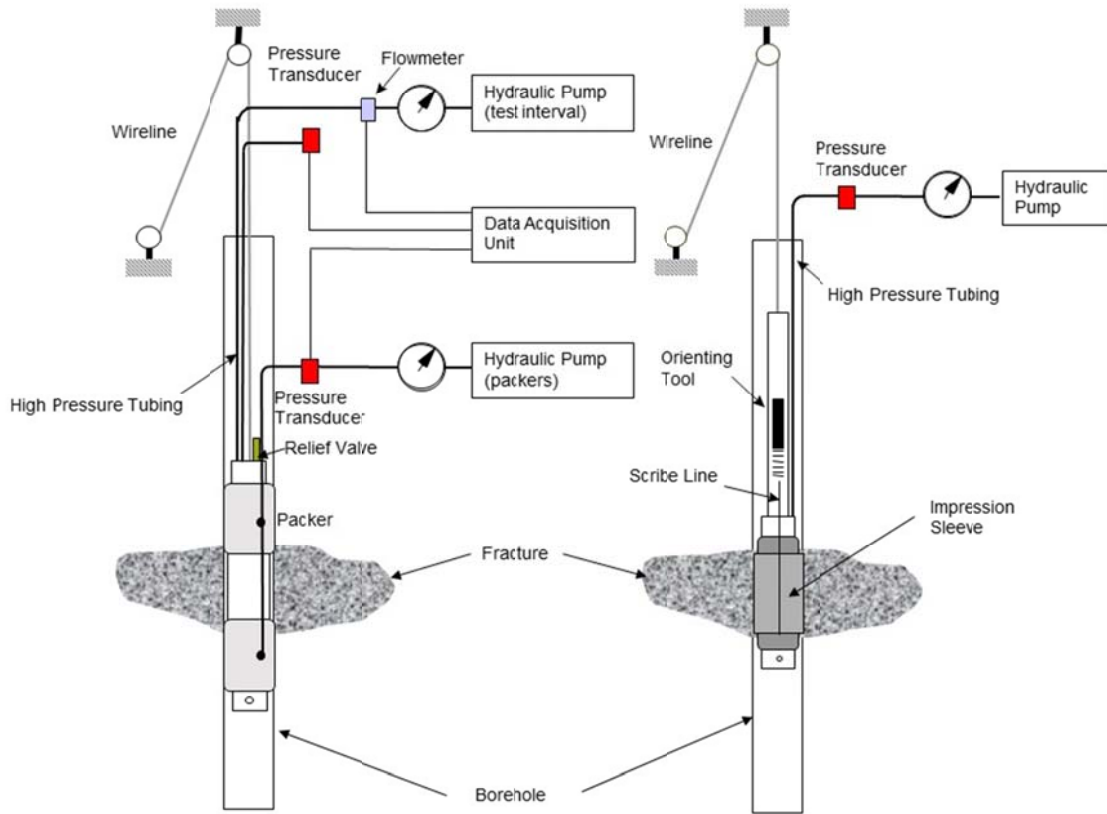
Figure 5.4. Wireline hydraulic fracturing system: Straddle packer for fracturing (left) and impression packer for fracture delineation.

Figure 5.5. Top adapter on the straddle packer assembly shows the interval and the packer pressure lines and the normally-open relief valve. The parallel interval pressure line connected to the surface pressure transducer is hidden behind the stem connected to a wireline.

5.3.3   Impression Packer

The wireline impression packer-orienting tool assembly is a downhole probe employed to delineate the hydraulic fracture on the borehole wall. It consists of an orienting tool that is lowered to the test zone attached to the impression packer. The simultaneous and continuous tripping of the tool assembly significantly reduces the time required for fracture delineation, as compared with the conventional drill-rod procedure.

Once the impression packer-orienting tool is set at the precise depth of a previously fractured interval, the impression packer is pressurized to ~15 MPa (2175 psi). The packer pressure is maintained for about 30 minutes to allow the soft impression sleeve to protrude into the opened hydraulic fracture. The orienting tool consists of a pitch/roll compensated compass/magnetometer, which sends the orientation of the reference line on the impression packer to the surface monitor in real time (Fig. 5.6).

Packer deflation is achieved by pressure-venting and activating the downhole relief valve as in the straddle packer (Fig. 5.4). After the retrieval of the impression packer, it is inspected for any traces of fractures. These are marked with an indelible marker, and traced with respect to the scribe line on a transparent plastic sheet wrapped around the packer for later detailed analysis.
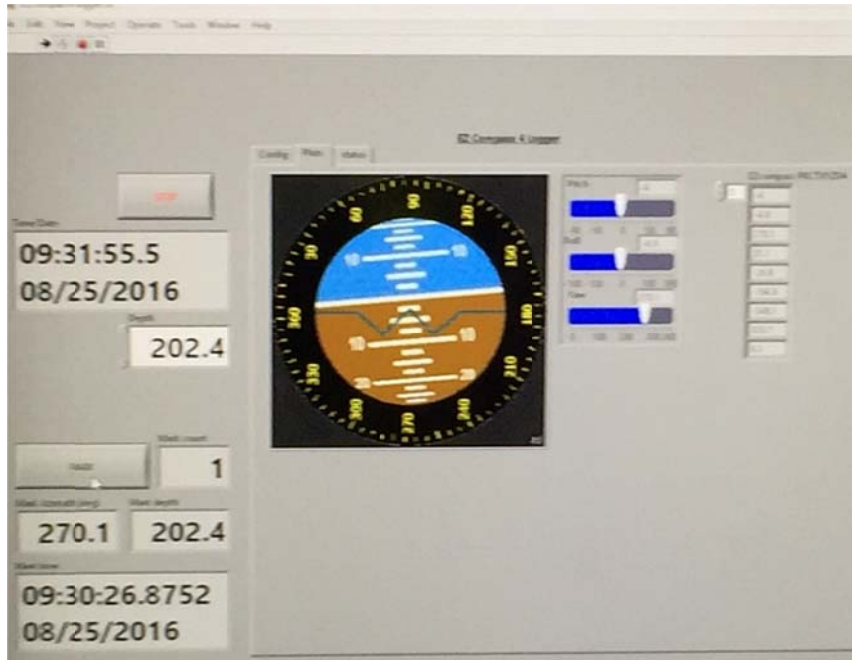
Figure 5.6. Real time transmission of compass/magnetometer information for the orientation of the impression packer.

5.3.4   Pressure Generator

In order to run hydraulic fracturing tests, hydraulic fluid pressure is generated by two pneumatic pumps (one for the packers and the other for the testing interval between the packers). This pumping system has one pressure transducer and a pressure gauge for the fracturing interval and another pressure transducer and a pressure gauge for the packers. A flow meter is also employed to monitor the flow of water into the test zone. Fig. 5.7 shows the schematic of the pressure generator system. The system is designed to be

intrinsically safe by using components with a pressure rating higher than the maximum pressure the pumps can generate.
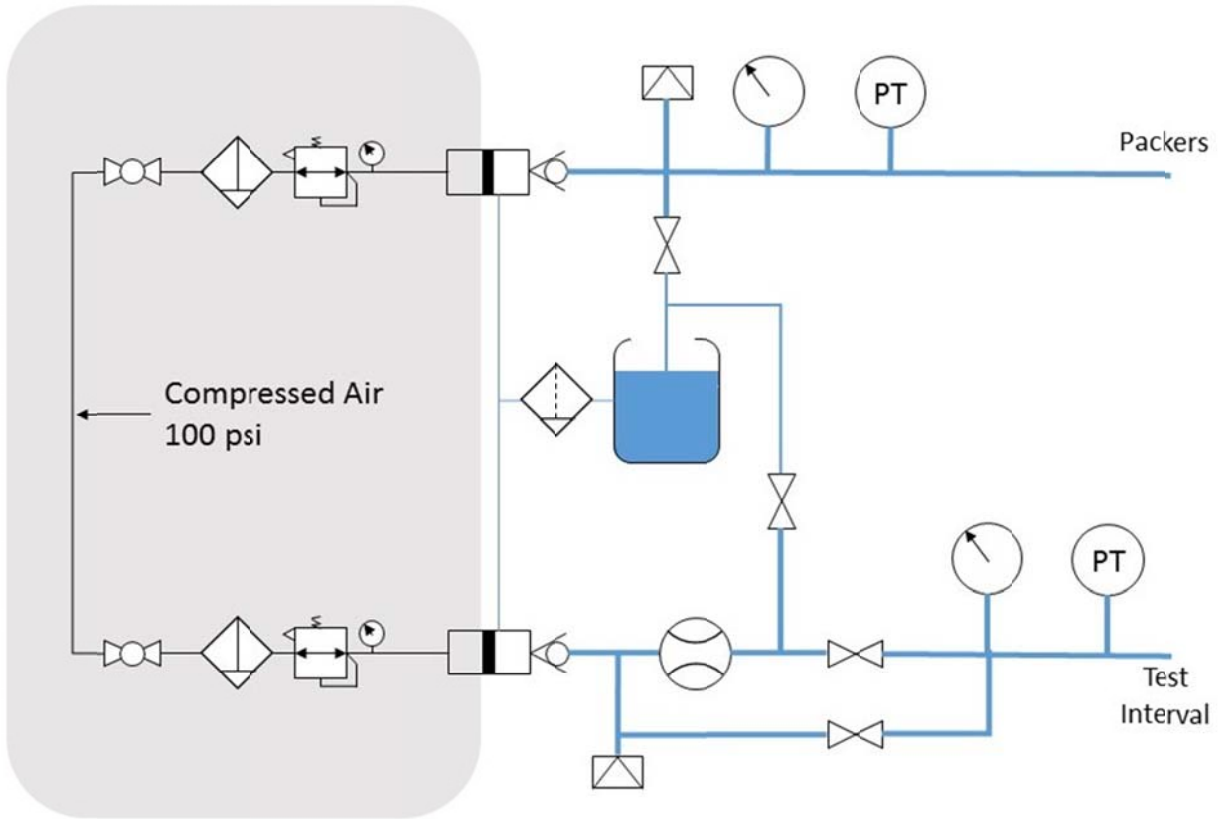
Figure 5.7. Schematic diagram of the pressure generator used for kISMET hydraulic fracturing and fracture stimulation.

5.3.5   Hydraulic Fracturing Digital Data Recording

The flow rate of the injection fluid into the fracturing test zone is monitored by a turbine flowmeter connected between the surface pump and the high-pressure tubing leading to the test zone. The packer and test-interval pressures as well as the flow rate are recorded simultaneously in a portable computer using an analog-to-digital (A/D) converter and also in the integrated digital data logger at 10 samples/s for each channel. Digitally recording data allows for statistical discrete data analysis for analyzing shut-in and fracture reopening pressures. A schematic diagram for the digital data recording system and a photograph are shown in Figs. 5.4 and 5.8, respectively.

Figure 5.8. Pressure generators and digital data recorders used for hydraulic fracturing and fracture stimulation at SURF.

5.4   Hydraulic Fracturing Program and Procedures

5.4.1   Stress Measurement Procedures

To perform a hydraulic fracturing stress measurement, two inflatable rubber packers hydraulically isolate a 0.75-meter section of a borehole using high pressure to seal against the borehole wall. Hydraulic fluid (water) is pumped at a low flow rate into the packed-off interval, gradually raising the pressure on the borehole wall until a fracture is initiated in the rock, indicated by a drop of the interval pressure. Pumping is stopped by closing the valves of the supply-side compressed air as shown in Fig. 5.4, allowing the interval pressure to decay. Several minutes into the shut-in phase, the pressure is released and allowed to return to ambient conditions. The pressure cycle is repeated three times maintaining a similar flowrate, although the second and third repetitions sustain pumping for one to two minutes to extend the fracture. Key pressure values used in the computation of the in situ stresses are picked from the pressure–time record. The repeated cycles provide redundant readings of the key pressures. The interval pressure is released and the flowback from the interval returns to the surface. Fig. 5.9 shows a typical pressure-flow rate-time plot from one of our hydraulic fracturing tests at kISMET.
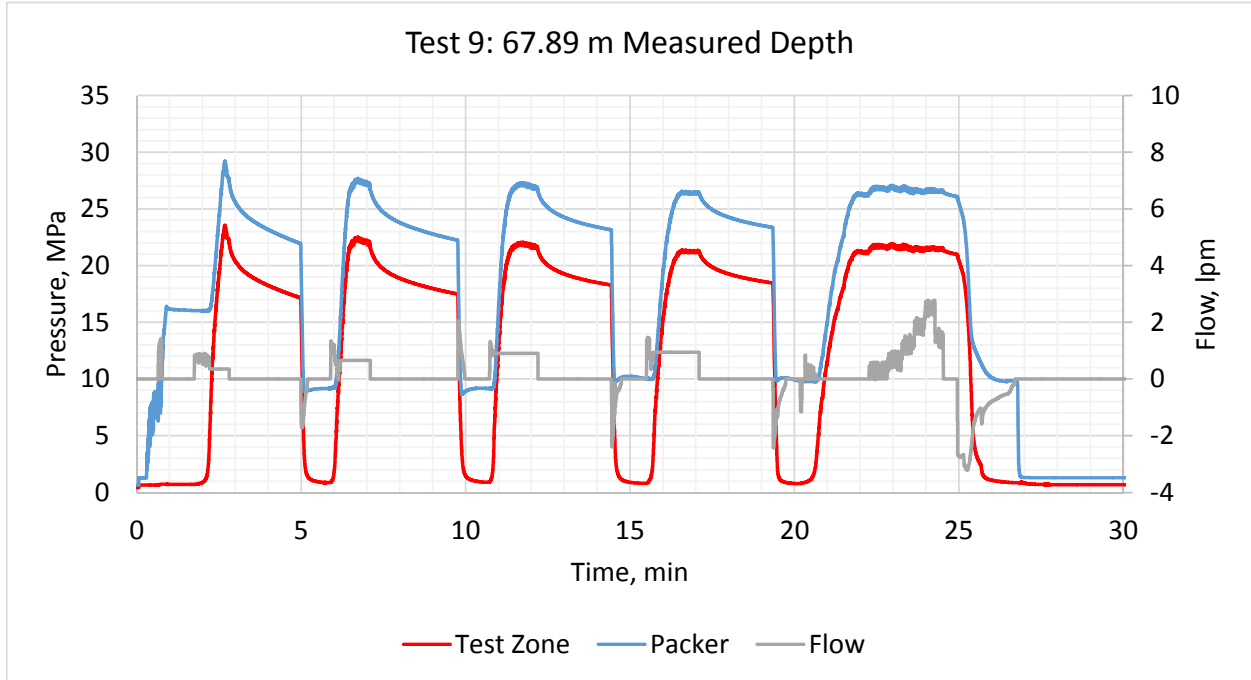
Figure 5.9. Pressure-time and flow rate-time plot obtained in Test #9 in kISMET-003.

The testing program was originally planned to include five hydraulic fracturing stress measurements at depths between 60 and 100 m (197 and 328 ft) in borehole kISMET-003, the central stimulation hole for the experiment. The upper limit of 60 meters was to provide a 20-m buffer between stress measurement zones and the main stimulation zone at 40.3 meters. The straddle packer assembly had a 0.75-m interval between the packers, and the packers themselves had 0.9-m sealing lengths. The goal of zone selection was to find 3-m long sections with 1-m of rock free of natural fractures with 1-m buffer zones above and below that were free of anything that could compromise the packer seal.

Test zones were selected based on inspection of the core. With the high rock quality, it was possible to find zones that were free of open and healed natural fractures with a minimum of quartz or calcite veins. Where possible the selection favored rock with less distinct foliation to reduce the likelihood that fractures would preferentially be controlled by the rock anisotropy.

The original target was to have five test zones with approximately equal spacing and a 20-m buffer zone to the main stimulation horizon. The buffer zone was based on predictions of fracture sizes in which fluid injection of 4 liters for a stress measurement would produce a fracture with a 3.4 m radius and an injection of approximately 30 liters for the main stimulation would produce a fracture with about an 8-m radius (see Chapters 4 and 7).

After the deepest original test zone at 95.2 m was found to have an anomalously high shut in pressure, two tests were added at 97.3 m and 89.4 m to better define the bounds of the possibly higher stressed rock.

After completing the fracturing in the seven test zones, the access to the borehole below approximately 72 m (236 ft) was lost due to a stuck impression packer. This prevented access to the deep parts of borehole kISMET-003 to obtain fracture orientations for Tests 1 through 6. In order to obtain data for five intervals as planned, including fracture orientations, three tests plus the stimulation interval test were carried out above 72 m in addition to Test 7. The list of test zones appears in Table 5.1 and Figure 5.10.

Table 5.1. Measured pressure values used for stress interpretation.

Test	Depth		Measured Depth		Cycle 1	Cycle 2	Cycle 3	Cycle 4		Step Test
					Breakdown Pressure, P_b	Reopening Pressure, P_r	Shut in Pressure, P_{dpdt}			Jacking Pressure, P_j
	m	feet	m	feet	MPa	MPa	MPa			MPa
Stimulation, Test 11	1519	4982	40.23	132	22.9	18.0	20.3	20.3	20.3	20.5
Test10	1532	5027	53.95	177	30.4	25.8	24.4	24.1	24.1	
Test7	1540	5052	61.57	202	29.5	23.3	23.5	23.9	23.9	
Test9	1546	5072	67.67	222	23.6	18.7	20.4	21.0	20.7	21.7
Test8	1548	5079	69.80	229	24.6	18.3	20.6	21.0	20.6	21.3
Test5	1552	5091	73.46	241	29.5	20.7	22.1	22.0	21.8	
Test4	1558	5112	79.86	252	26.3	20.4	20.0	19.9	20.0	
Test3	1563	5129	85.04	279	27.6	18.8	20.7	20.7	20.4	
Test6	1568	5143	89.31	293	26.9	19.7	23.1	22.7	23.1	
Test1	1573	5162	95.10	312	*32.7*		*29.9*	*29.0*		
Test2	1576	5169	97.23	319	*33.7*		*27.4*	*26.9*	*29.0*	
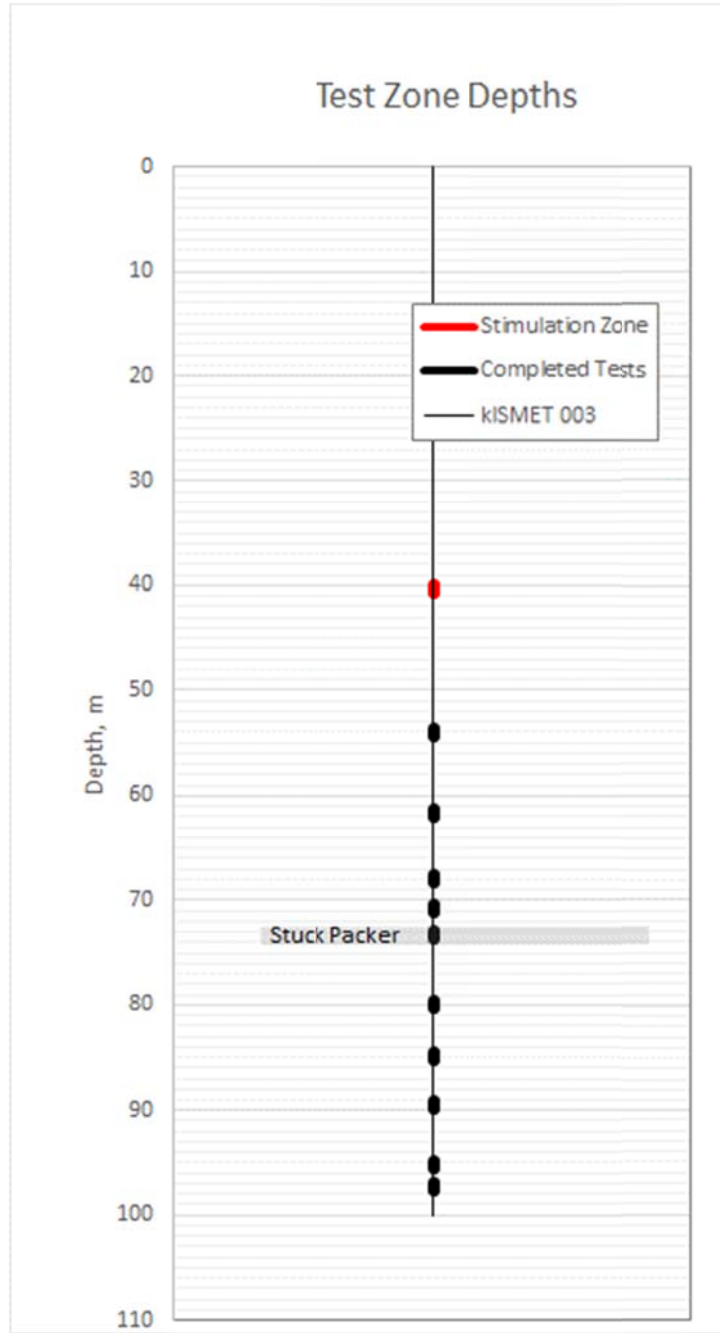
Figure 5.10. Test zone and stimulation zone depths. Bars represent the 0.75-m test interval lengths.

5.4.2   Fracture Stimulation Procedures

After all of the planned in situ hydraulic fracturing stress measurements were completed, the straddle packer was moved to a borehole depth of 40.2 m (1518.6 m below surface) for the stimulation test in conjunction with geophysical monitoring of the induced fracture. Continuous Active Source Seismic Monitoring (CASSM) was set up to run continuously, and Electric Resistivity Tomography (ERT) was triggered to capture the steady state of the constant Pressure-Flow rate (P-Q) period following initiation of a hydraulic fracture, during which time a relatively stable state with an open fracture was maintained. Low flow rates were used in order to maintain an open fracture as indicated by constant pressure.

Following initiation of a hydraulic fracture indicated by breakdown at 22.7 MPa (3291 psi), five stimulation cycles were conducted (Fig. 5.11). The first two cycles were conducted with a relatively low flow rate of 0.48 lpm, while the next three cycles used a relatively high flow rate of 0.63 lpm. For each cycle, the steady-state pressures were achieved at 20.1-20.3 MPa (2914-2943 psi). The steady state P-Q was maintained for approximately 15 minutes in order to finish one round of ERT data acquisition (CASSM run takes ~20 sec). The amount of fluid injected for each cycle was 7.2, 7.7, 6.0, 9.0, and 11.7 liters from the 1st to 5th stimulation cycles, respectively. The fracture stimulation tests were successfully conducted with continuous CASSM data and four sets of ERT data while the fracture was kept open.
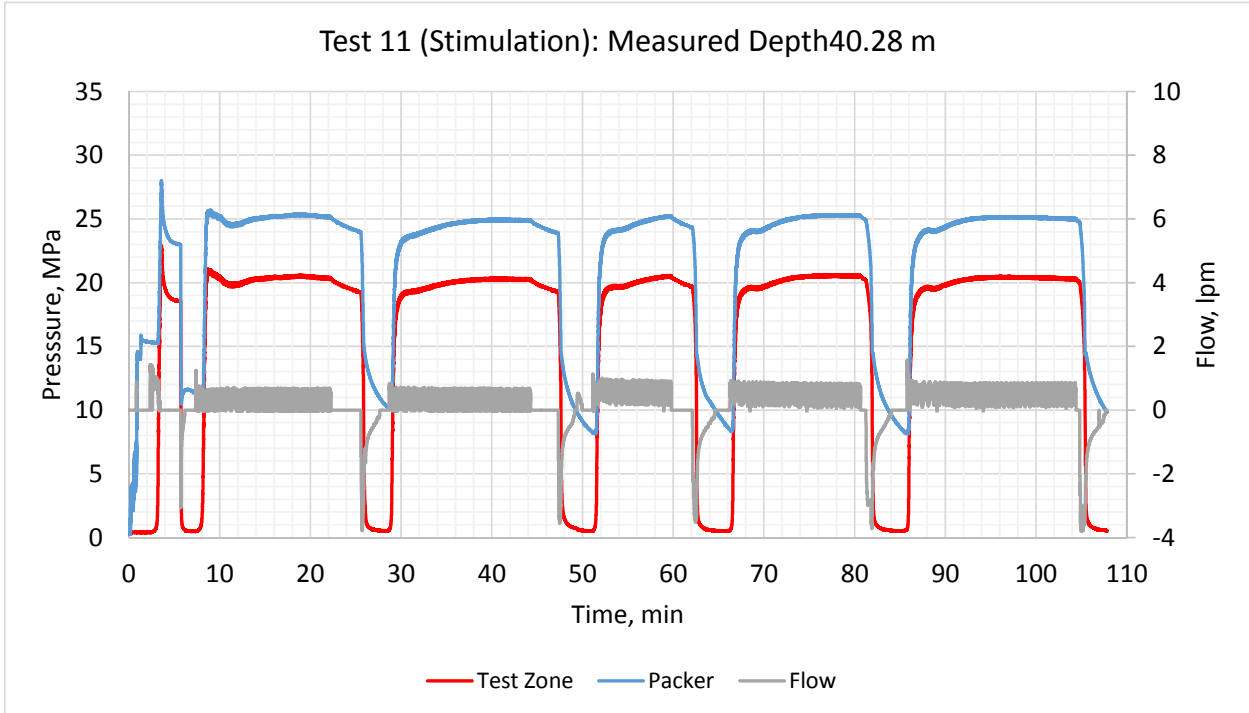
Figure 5.11. Pressure-flow rate-time plot obtained during the stimulation experiment in kISMET-003.

5.4.3   Fracture Delineation and Orientation

After completion of the first seven hydraulic fracturing tests in the deep part of borehole kISMET-003, we attempted to obtain oriented fracture impressions using the wireline impression packer with compass/magnetometer. The impression packer was lowered to the shallowest test depth (Test #7 at 61.6 m borehole depth (1540 m below surface)). The impression sleeve produced only short traces of a fracture. The traces were about 2 inches long and they were not mirrored on the other side of the packer. The incomplete trace was thought to be an effect of inflating the packer to only 15 MPa (2175 psi) while the shut in pressure of that test appeared to be around 20 MPa (2900 psi). For the second impression test (Test #5 at 73.5 m (241 ft) borehole depth (1551.6 m (5090 ft) (below surface)), the packer inflation pressure was raised to 20 MPa (2900 psi) in an attempt to get a clear impression of the fracture. The pressure was declining slightly, and an attempt to bring the pressure back to the 20 MPa level resulted in an apparent failure of the packer element as indicated by complete loss of pressure in the packer. On attempting to retrieve the packer back to the surface, it became stuck in the hole after coming up only about 30 cm (12 in). We believe the impression packer element ruptured which resulted from inflating the impression sleeve excessively. Many attempts to retrieve the impression packer failed. Finally, we decided to retrieve the compass/magnetometer probe and hydraulic lines by shearing the safety pin located between the packer element and the downhole orienting probe, leaving the impression packer in

the borehole. Loss of access to depths below 72 m (236 ft) was disappointing, but we still had the five-spot pattern at ~50 m depth for the stimulation test and plenty of pristine borehole left for stress testing.

The acoustic borehole televiewer (BHTV) is a logging device that provides an oriented acoustic image of the borehole wall. A fracture intersecting the borehole appears as a dark signature on the images caused by low acoustic reflectivity (Fig. 5.12). The acoustic BHTV was the backup strategy to the impression packer to delineate and orient hydraulic fractures. Its results were successful compared with optical televiewer attempts, which could not distinguish the dark fractures from the surrounding dark rock (see also Section 6.4.2). There were two acoustic televiewer runs. The first run provided a pre-fracture image for Tests 8-11 over the interval above the stuck impression packer at approximately 72 m (Test 5). Because this run was performed after Test 7, and Test 7 lies above Test 5, the pre-fracturing image includes the hydraulic fracture generated for Test 7. A second run of the acoustic televiewer log picked up the images of the fractures for Tests 8 through the stimulation Test 11.
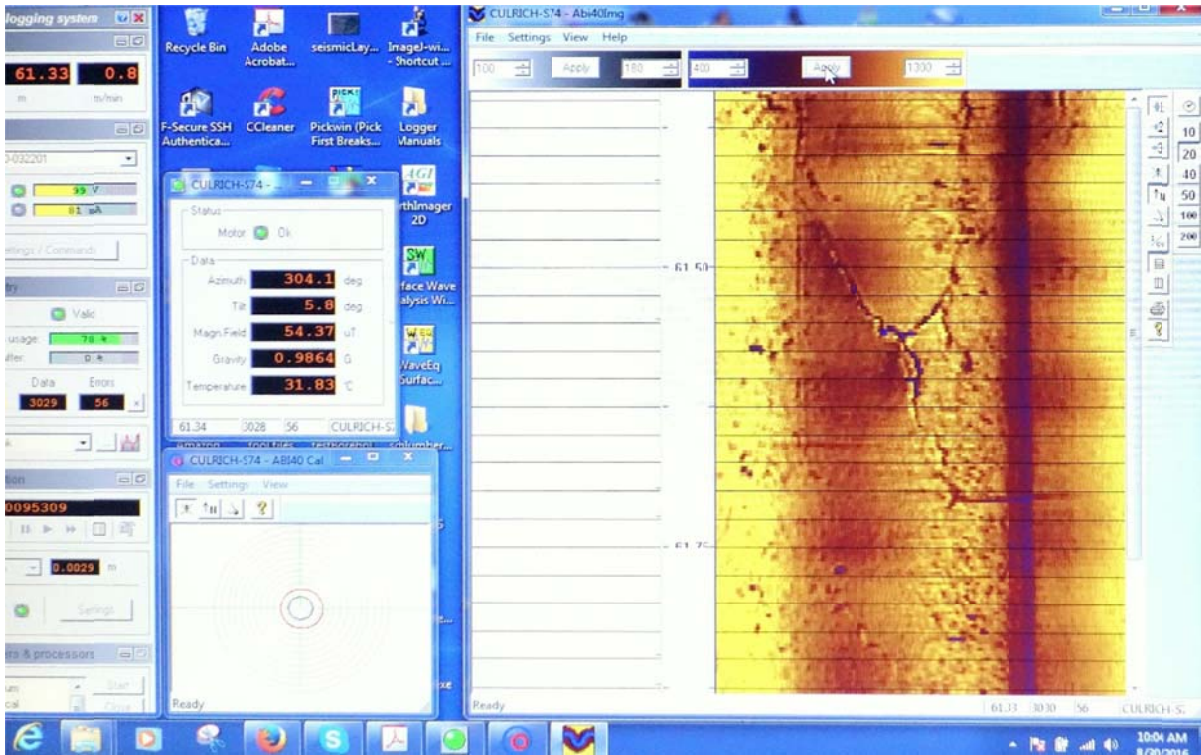
Figure 5.12. Realtime shot of the acoustic BHTV image for hydraulic fracture at Test#7 zone at   61.6 m depth in borehole kISMET-003.

5.5   Data Analysis and Results

5.5.1   Methodology

Hydraulic fracturing has become a standard method for determining the in situ state of stress in rock masses for use in engineering design, and is one of the few methods available for testing in deep boreholes (Haimson, 1978). Although numerous past measurements of in situ stress have been made at

SURF under all of its various names over the years, the present measurements are the first to be performed using hydraulic fracturing.

Hydraulic fracturing occurs when the fluid pressure in the isolated portion of the borehole reaches a critical level, called the breakdown pressure, P_b. At breakdown, the rock fractures in tension causing borehole fluid loss and a drop in pressure. Fig. 5.13 shows an idealized pressure-time record for a hydraulic fracturing stress measurement with the important pressures labeled. The inset shows the creation of the hydraulic fracture normal to the minimum horizontal stress, σ_{HMin}.

With continued injection, the pressure in the test zone stabilizes to a value that reflects the balance of keeping the fracture open, extending the fracture, and pressure and flow losses along the fracture length. The resistance to fracture extension decreases as the fracture grows, but the pumping pressure was only slightly greater than the stress normal to the fracture because of the low pumping rates used in these experiments.

The cessation of pumping is called "shut in," and the pressure after shut in, P_{si}, is taken as a measure of the stress normal to the fractures. For a vertical fracture in a vertical borehole, this is the minimum horizontal stress, σ_{HMin}. There are several measures of the shut-in pressure including the instantaneous shut-in pressure, P_{isip}, a small, sharp drop immediately on cessation of pumping, and the derivative shut-in pressure, P_{dpdt} (Hayashi and Haimson, 1991). P_{dpdt} has a basis in defining multiple flow periods from the end of fracture extension through fracture closure and is based on the widely used hydraulic fracturing analysis methods used in the oil industry (Nolte, 1986).

An additional widely used method of obtaining the stress normal to the fracture is the step test, or hydraulic jacking test (Doe and Korbin, 1987) shown in Fig. 5.13 and in the last injection cycle in Fig. 5.9. This method injects at variable pressures and rates to produce a pressure versus rate plot that indicates fracture opening. Step tests may use relatively large amounts of fluid especially in the higher pressure and flow steps. In the interests of limiting fracture size and the extension of stress-measurement hydraulic fractures into the main kISMET experiment volume at approximately 50 m (164 ft) depth in borehole kISMET-003, step tests were limited to only two stress measurements and those used relatively short step durations.

Shut-in pressure determination may have considerable uncertainty when the rock is permeable due to conductive fractures or appreciable rock matrix permeability, which create a rapid pressure fall off after shut in. Fortunately for these tests, the pressure decay after shut in is slow, and the range of shut-in pressures from different methods is not highly variable. Furthermore, because of the quality of the tests due partly to the low permeability of the rock, step tests were not essential to define the shut in pressure.
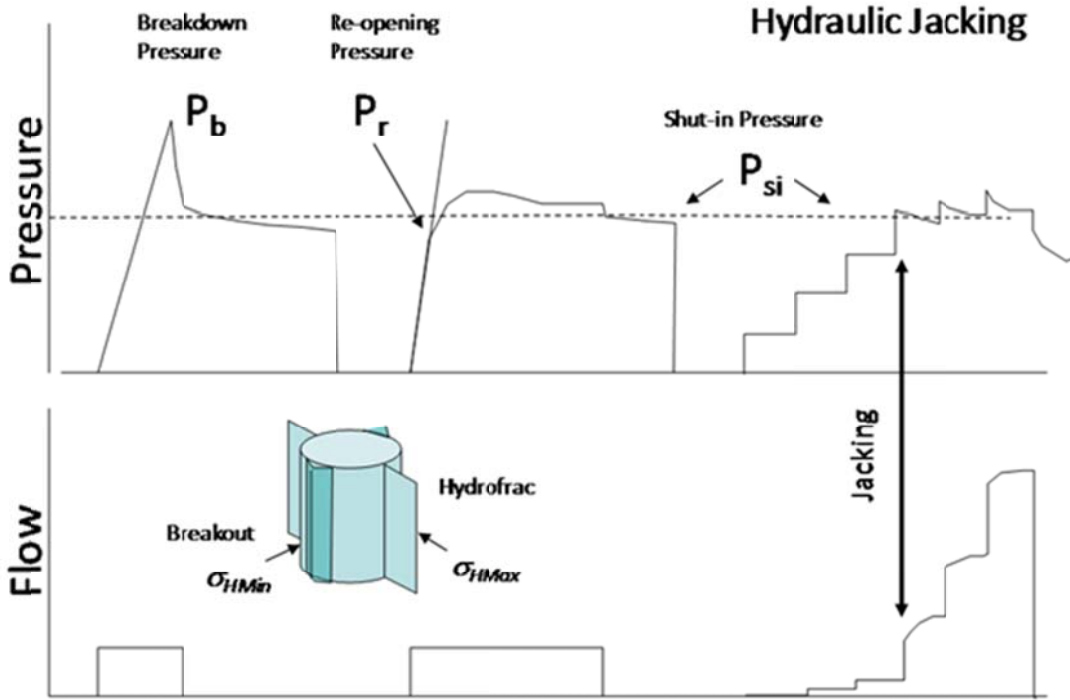
Figure 5.13. Idealized hydraulic fracturing pressure-time record. Inset shows location of triangular prismatic borehole breakouts relative to horizontal stress directions.

5.5.2   Minimum Horizontal Stress Results

The pressure and flow-rate data for all 11 tests are presented in Table 5.1. Overall, the test data quality is excellent with well-defined breakdown pressures and clear shut-in pressure signatures. The minimum horizontal stress values presented in Table 5.2 use the results from Tests 3 through 11, based on an average of the P_{dpdt} values for Cycles 3 and 4, which have sufficient injection volume to develop the fracture. The results of Tests 1 and 2 were anomalous and are discussed further in Section 5.5.4.

The minimum horizontal stress values for Tests 3-11 range from 20.0 to 24.1 MPa (2900 to 3494 psi), averaging 21.7 MPa (3146 psi) with a standard deviation of 1.6 MPa (232 psi). The values have a high level of consistency that is typical for hydraulic fracturing stress measurements in low-permeability, relatively uniform rock. The minimum horizontal stresses are 51% of the lithostatic stress with a standard deviation of 4%.

Table 5.2. Calculated in situ stress values.

Test	Depth	Measured Depth	Pore Pressure, P_0	Minimum Horizontal Stress, σ_{HMin}	Maximum Horizontal Stress, σ_{HMax}	Vertical Stess, σ_v	Ratio σ_{HMin}/σ_v	Ratio σ_{HMax}/σ_v
	m	m	MPa				Percent	
Stimulation, Test 11	1519	40	0.39	20.3	42.6	41.7	49%	102%
Test 10	1532	54	0.53	24.1	46.0	42.0	57%	109%
Test 7	1540	62	0.60	23.9	47.9	42.3	57%	113%
Test 9	1546	68	0.66	20.9	43.2	42.4	49%	102%
Test 8	1548	70	0.68	20.8	43.5	42.5	49%	102%
Test 5	1552	73	0.72	21.9	44.3	42.6	52%	104%
Test 4	1558	80	0.78	20.0	38.7	42.8	47%	91%
Test 3	1563	85	0.83	20.6	42.1	42.9	48%	98%
Test 6	1568	89	0.88	22.9	48.2	43.0	53%	112%
Test 1	1573	95	0.93	*29.5*		43.2	*68%*	
Test 2	1576	97	0.95	*27.8*		43.2	*64%*	
Average Test 3-11				21.7	44.1	42.5	51%	104%
St. Deviation				1.6	3.0		4%	7%

5.5.3   Maximum Horizontal Stress Results

The method of estimating maximum horizontal stress σ_{HMax} from the initial breakdown pressure, P_b, and reopening pressure, P_r, in subsequent repressurization cycles has been used in a large number of hydraulic fracturing measurements since it was introduced by Bredehoeft et al. (1976), quantified statistically by Lee and Haimson (1989), and codified as the ISRM Suggested Method by Haimson and Cornet (2003). The calculation of maximum horizontal stress is based on the presence of a stress concentration around the borehole that influences fracture initiation or fracture reopening. When based only on the first pressure cycle, the calculation of maximum horizontal stress requires knowledge of the rock tensile strength and appropriate pore pressure value by the equation

$$\sigma_{HMax} = 3\sigma_{HMin} - P_b - P_0 + T \qquad (5.2)$$

where T is the rock tensile strength and P_0 is the pore pressure. Laboratory testing of cores from the test intervals is ongoing and will be incorporated into a maximum stress analysis in the future, although the lack of information on the tensile strength scale effect, which is substantial in rock, may be problematic.

In Table 5.2, we show results of calculations of σ_{HMax} using the method of Lee and Haimson (1989). It is based on the difference between the breakdown pressure P_b achieved in the first pressure cycle, and the fracture reopening pressure P_r recorded in the second pressure cycle. In the first pressure cycle, P_b has to overcome both the minimum tangential stress at the borehole wall and the tensile strength of the intact rock, whereas P_r needs to just overcome the tangential stress. Because the fracture has already been created, the difference between the two pressures is equal to the tensile strength. Included in Table 5.1 are the first cycle breakdown pressures, P_b, and the second cycle reopening pressures, P_r. These values are used for calculating the maximum horizontal stress, σ_{HMax}, using the equation:

$$\sigma_{HMax} = 3\sigma_{HMin} - P_r - P_0 \qquad (5.3)$$

The maximum horizontal stress values range from 38.7 to 48.2 MPa with an average of 44.1 MPa. These values are close to the lithostatic pressure, or the calculated σ_v, averaging 104% of the vertical stress with

a standard deviation of 7%. While there is uncertainty in this estimate of σ_{HMax}, it appears that at this depth, the vertical stress and maximum horizontal stresses are similar in magnitude which may be indicative of the cross-over from a tendency for strike-slip faulting at shallow crustal depths to a tendency for normal faulting in the deep crust (Zoback et al., 2003).

Although the methods we have used are widely applied, they are based on several assumptions, such as linear, isotropic elasticity, or the interpretation of the variables, P_b and P_r. For example, some authors have pointed out that the reopening pressure includes effects of system compliance and that the fracture has not propagated far away from the stress concentration at the borehole (Rutqvist et al., 2000; Bunger et al., 2010). We have not analyzed these possible effects quantitatively, but we point out that our pressurization system was close to the hydraulic fracturing interval to minimize problems of system compliance and we used low flow rates to control fracture propagation. The uncertainty associated with the assumption of the Kirsch solution for stress distribution around a circular hole is more problematic given the anisotropy of the phyllite. An alternative approach using linear elastic fracture mechanics for the breakdown pressure will be pursued in future kISMET research.

5.5.4   Results of Tests 1 and 2

The results from Tests 1 and 2 were anomalous. They are reported in Tables 5.1 and 5.2, but are excluded from the stress averages for reasons discussed below. These tests, the deepest and farthest from the kISMET experimental volume at 50 m (164 ft) depth in borehole kISMET-003, yielded somewhat different pressure-time behaviors from the later tests. This was partly because these tests employed somewhat different protocols because they were being used to determine the optimal injection rates and durations for the rock. These two tests yielded peak/breakdown and shut in pressures that were notably higher compared with later tests. Specifically, Tests 1 and 2 have average shut in pressures of 28.3 MPa (4103 psi) for cycles 3 to 4, compared with 21.7 MPa (3146 psi) for Tests 3-11. The breakdown or peak pressures for Tests 1 and 2 average 33.2 MPa (4814 psi) compared with 26.8 MPa (3886) for Tests 3-11.

One speculation for the different behavior of Tests 1 and 2 is that these tests opened one or more pre-existing fractures that were not oriented normal to the minimum horizontal stress, thus producing shut in pressures that were higher compared with the later, shallower tests. Another speculation is that the stresses may be higher in the deeper portion of the borehole possibly due to greater rock stiffness. Resolving these and other possibilities will require access to the deeper portion of the borehole to obtain image logs of the fractures and full wave sonic logs to obtain elastic properties. Given the uncertainty for Tests 1 and 2, the associated shut-in pressures and minimum stress values are shown in italics in Table 5.1 and as shaded values in Fig. 5.14. As the main purpose of these stress measurements is to provide a stress state for interpreting the kISMET monitoring results, it is appropriate to exclude these anomalously higher results for that purpose because they are well outside the kISMET volume relevant to the stimulation experiment. Nevertheless, we are including these results because non-uniformity of stress could be a consideration in planning future kISMET-type experiments at this site.
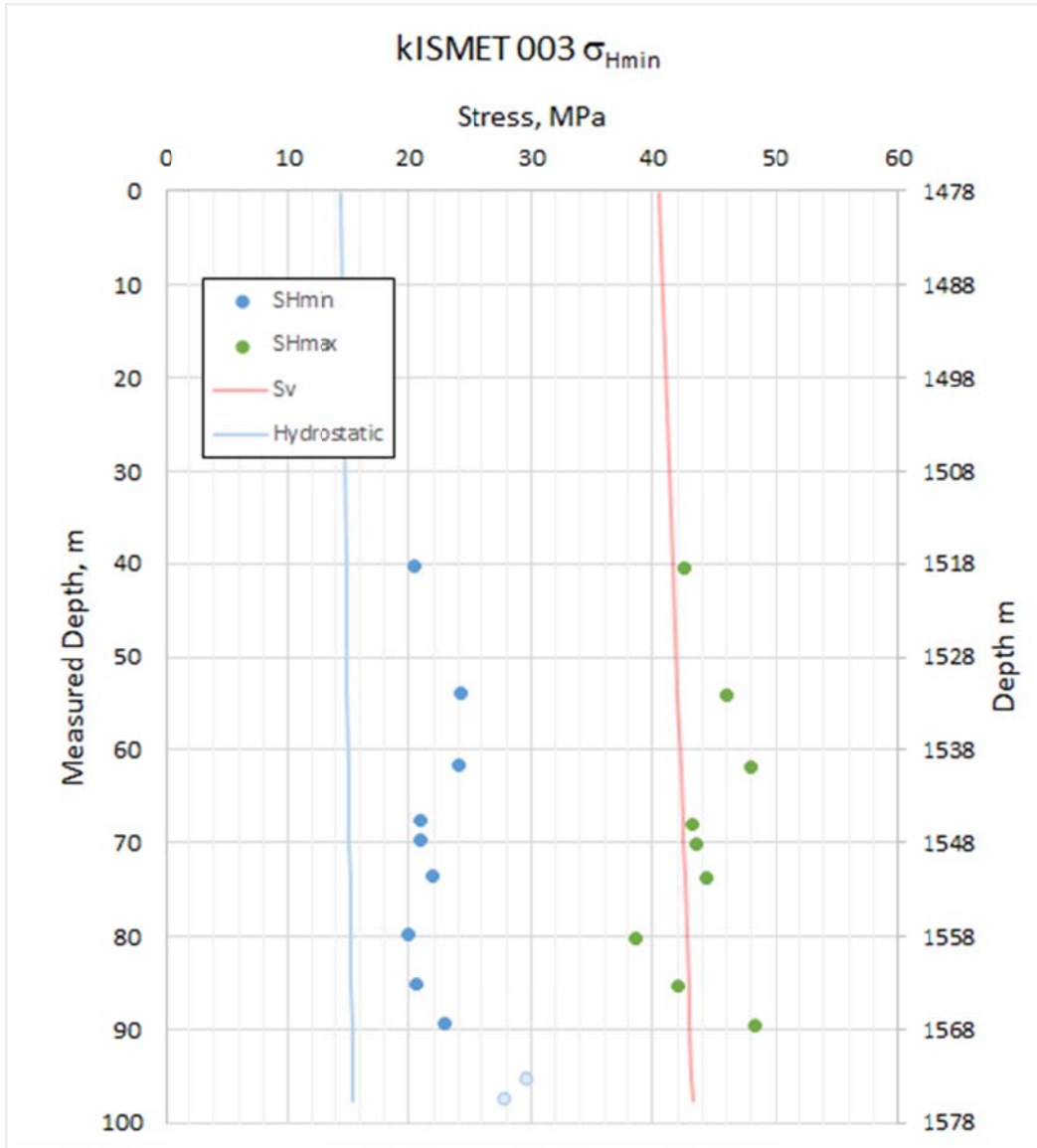
Figure 5.14. Minimum and maximum horizontal stresses versus depth in borehole measured and depth below surface. Vertical stress is based on a density of 2800 kg/m^3 and hydrostatic pressure is based on water column to the surface.

5.5.5   Orientation of Horizontal Stresses

A fundamental principle of hydraulic fracturing stress measurement is the alignment of the hydraulic fracture in the direction normal to the overall minimum principal stress. In the case where a vertical hydraulic fracture is created, that fracture is aligned with the direction of the maximum horizontal stress. The primary means of obtaining fracture orientation information was the acoustic televiewer log, which was run prior to Test 8 to provide a pre-fracturing image for Tests 8 to 11 as well as to obtain the fracture image for Test 7, which had already been performed. After completing the hydraulic fracturing, the acoustic televiewer log was rerun to pick up the locations and orientations of the generated fractures. Fig. 5.14 shows an example of acoustic televiewer log for the Test 11 stimulation zone. The figure shows the pre-fracture and post-fracture images along with a marked interpretation of the fracture image.

Included in Fig. 5.15 is the optical televiewer log for the same interval. The optical televiewer log was unable to detect the hydraulic fractures partly due to the lack of optical contrast between the fracture and the dark rock. What the optical image does show, however, is the orientation of the foliation, which is shown with overlain blue line. The comparison shows that the hydraulic fractures, while having a steep dip, are not being captured by the foliation and are therefore more likely to be representative of stress controls than on control by rock anisotropy.
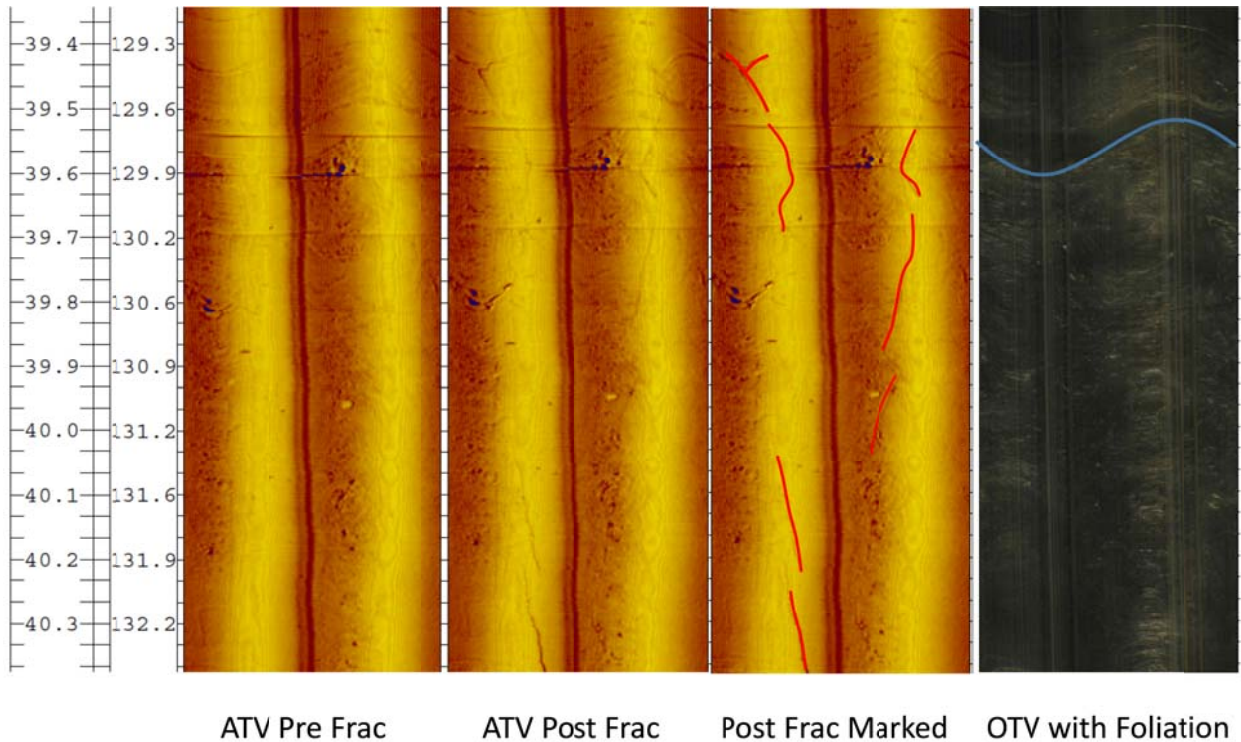
Figure 5.15. Acoustic televiewer logs for the Test 11 stimulation zone (40.23 m depth in borehole).

The analysis of the acoustic televiewer logs involved digitizing the fracture traces and importing them to an Excel spreadsheet, where they were fitted to sinusoidal traces of known orientation. The traces were all corrected for magnetic declination and represent orientations relative to true North. Fig. 5.16 shows the fitted orientations and the fracture traces. The orientations are given in strike and dip where the dip direction is 90° clockwise to the strike (right-hand rule). The fracture trace data are given in Table 5.3. The stimulation zone and Test 7 produced fracture images that have traces in the test zone as well as under the packer seats. Tests 8, 9, and 10 produced fracture traces that are only under the packer seats. The lack of traces in the test zone does not mean fractures were not generated as they may have closed. Also, traces under the packer seats are valid indicators of stress orientation.

Table 5.3. Fracture orientation data from acoustic televiewer logs.

	Test 7			Test 8		Test 9	Test 10	Test 11		
Depth, m	61.5	61.1	61.2	69.8	69.7	68.7	54.5	39.8	40.1	41.1
Strike	80	72	58	100	82	95	90	100	100	83
Dip Direction	170	162	148	186	172	185	180	190	190	173
Dip	80	82	77	67	72	85	65	85	85	83
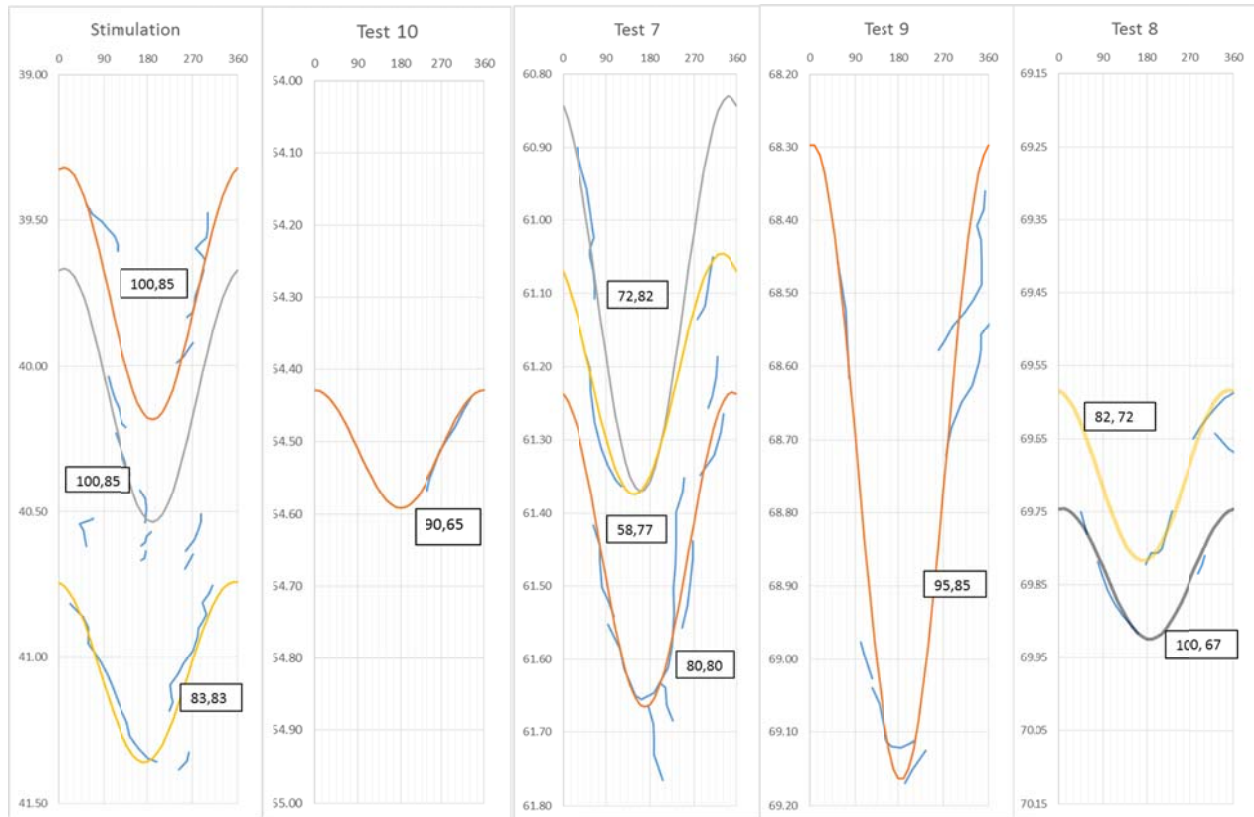
Figure 5.16. Interpreted fracture traces from acoustic televiewer logs. Orientations are strike and dip based on the right-hand rule (dip direction is 90 degrees clockwise of strike).

The quality and consistency of the fracture orientations mirror that of the shut-in pressures from the hydraulic fracturing. Overall the data set provides an excellent indicator of the maximum horizontal stress direction. Fig. 5.17 shows stereographic projections of the fracture planes and the fracture poles. The concentration of the poles fits a Fisher distribution with a 356° trend and 12° plunge to 95% confidence indicating fractures that are striking N86°E with a dip of 78° to the southeast. The fact that the fractures are not following foliation but have a non-vertical, though very steep, dip indicates that one of the principal stresses may be inclined slightly off vertical.

As discussed above, the strike of vertical to steeply dipping fractures created from a vertical hole is the direction of the maximum horizontal stress, which for these stress measurements may be taken as N86°E.
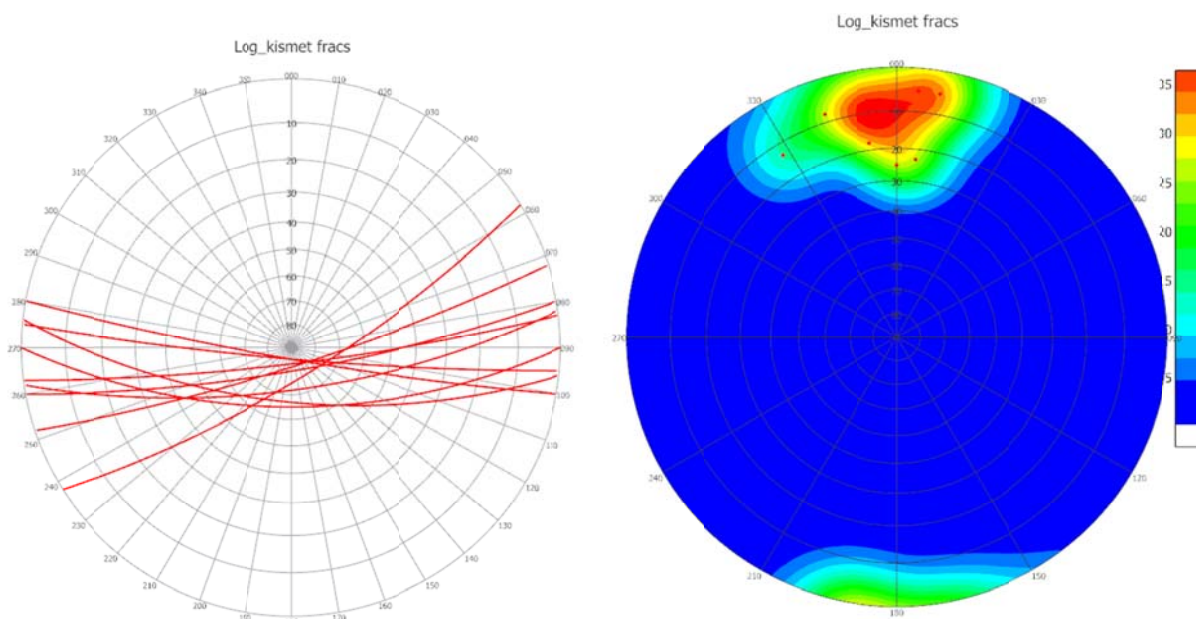
Figure 5.17. Stereographic projections of hydraulic fractures. Left: plane plot. Right: contoured pole plot.

5.6   In Situ Stresses at kISMET in Relation to the Regional State of Stress

In their review of stresses in the midcontinent, Zoback and Zoback (1989) concluded that the midcontinent is characterized by a relatively uniform compressive stress field with a σ_{Hmax} oriented NE to ENE. Since the publication of the 1989 paper, there has been at least one additional series of stress measurements in the northern Great Plains, specifically at Quimby, in northeast Iowa, where nine hydraulic fracturing stress measurements in Precambrian granite at depths between 500 m and 600 m confirmed the pervasiveness in the midcontinent of the NE to ENE σ_{Hmax} direction, and of the state of stress as being compressive in nature, yielding σ_{Hmin} = 11.7 (± 1.0) MPa (1696 psi); σ_{Hmax} = 18.0 (± 2.0) (2610 psi) MPa at N52°E, and calculated σ_v = 15.0 MPa (2175 psi) (Haimson and Lee, 1992).

The hydraulic fracturing measurements conducted as part of the kISMET project established the following average state of stress at 4850L in the West Access Drift, near the Davis Campus of SURF: σ_{Hmin} = 21.7 MPa (3146 psi); σ_{Hmax} = 44.1 MPa (6394 psi), acting at ENE to E; and calculated σ_v = 42.5 MPa (6162 psi). The horizontal principal stress directions are consistent with the general direction of the regional horizontal principal stresses (σ_{Hmax} trending NE to ENE); the average principal stress magnitudes of $\sigma_{Hmax} \approx \sigma_v \approx 2\sigma_{Hmin}$ are also in accord with the regional conditions. The local state of stress is typical of regions of high horizontal stresses, in which the relative magnitudes of the principal stresses vary from $\sigma_{Hmax} \geq \sigma_{Hmin} \geq \sigma_v$ at shallow depths, to $\sigma_{Hmax} \geq \sigma_v \geq \sigma_{Hmin}$ at intermediate depths, to $\sigma_v \geq \sigma_{Hmax} \geq \sigma_{Hmin}$ at great depths. At Quimby, the state of stress at 500-600 m depth is one in which $\sigma_{Hmax} \geq \sigma_v \geq \sigma_{Hmin}$; at 4850L in the West Access Drift, near the Davis Campus of SURF it is: $\sigma_v \approx \sigma_{Hmax} \geq \sigma_{Hmin}$ at a depth of 1550 m. At greater depths it is expected that the state of stress will evolve into $\sigma_v \geq \sigma_{Hmax} \geq \sigma_{Hmin}$.

6.   GEOPHYSICAL MONITORING AND ANALYSIS

Lead Authors: Yuxin Wu, Tim Johnson, Craig Ulrich, Bill Roggenthen, and Jonathan Ajo-Franklin

6.1   Introduction

Borehole logging and geophysical monitoring were conducted pre-, during, and post- stress tests and hydraulic stimulation at kISMET to assess fracture geometry and the potential use of geophysical methods for near-real time monitoring of fracture generation and propagation. Mt. Sopris borehole acoustic televiewer, optical televiewer and full waveform sonic logging were conducted focusing on the NQ (center, stimulation) borehole in the zone where we created the largest fracture (stimulation depth at 40 m (131 ft)) at the kISMET site. Electrical resistivity tomography (ERT) and Continuous Active Source Seismic Monitoring (CASSM) (Ajo-Franklin et al., 2011) were conducted in the monitoring wells (kISMET-001, 002, 004, and 005) during the extended stimulation tests at 40 m (131 ft) depth below the drift invert (floor). Passive seismic micro-earthquake (MEQ) monitoring was conducted during all of the stress test and stimulation events. We present here a summary of the results and interpretations as of the time of writing this report. Interpretation and analysis are in fact ongoing, future results from which will be presented at conferences and possibly in journal articles.

6.2   ERT

6.2.1   Overview

Cross-well ERT surveys were conducted in the monitoring wells using waterproof electrode array cables. ERT monitoring was carried out to provide information concerning the geologic structure, fabric, and heterogeneity of the host rock, and to assess the capability of ERT to image fractures during fracture stimulation. Two electrode cables with electrode spacing of 1.6 meters were used to collect crosswell imaging data separately between the kISMET-002 and kISMET-004 boreholes (referred to here as K2-K4 well pair), and between the kISMET-001 and kISMET-005 boreholes (referred to as the K1-K5 well pair). With electrodes deployed in the K2-K4 well pair, crosswell ERT data sets were collected before and after stimulation operations using a survey configuration design to optimize both spatial and temporal imaging resolution. With electrodes deployed in the K1-K5 well pair, crosswell ERT data sets were collected before, during and after stimulation operations.

ERT surveys have the potential to provide near-real time images of rock structure. We endeavored to test this possibility by sending collected data directly from the kISMET site via SURF's fast underground internet drop to PNNL where the data were inverted. With a 10-minute collection time and similar time for inversion at PNNL, the roundtrip collection-to-image time was around 20 minutes. We did not have time in the field to refine this workflow to demonstrate near-real time ERT, but this will be a priority in future ERT deployments.

Baseline, pre-stimulation data from both the K1-K5 and K2-K4 wellbore pairs were inverted simultaneously in 3D (e.g., Robinson et al., 2013), including explicit modeling of boreholes in true dimension with deviations, and explicit modeling of borehole fluid conductivity. The baseline images revealed steeply dipping electrical conductivity variations consistent with the host rock structure at the site, and the possible existence of high conductivity magnetite and/or sulfide minerals heterogeneously distributed in the host rock. These results have provided valuable information on the geologic structure between the cored and logged boreholes. Time-lapse images from both the K1-K5 and K2-K4 planes were not able to distinguish the induced fracture, likely due to the combined effects of a relatively small fracture zone, changes in borehole fluid conductivity during the imaging campaign, and the geometry of the imaging planes with respect to the fracture zone. Below we elaborate on the ERT methods and results for the kISMET project.

6.2.2   Borehole Configuration and ERT Computational Mesh

Host rocks at the kISMET site exhibit low electrical conductivity in comparison to the water in the borehole in which ERT electrodes are immersed. This contrast in conductivity causes the borehole fluid to act as a preferred flow channel for electrical current, which significantly influences ERT measurements. Failure to account for this effect in the ERT modeling would result in corresponding artifacts in the resulting images. In order to accommodate wellbore effects, each wellbore was modeled in true dimension using the borehole diameter and deviation logs collected after drilling (see Chapter 2 for discussion of deviation logging). The computational mesh we developed for ERT data inversion accounting for wellbore effects is shown in Fig. 6.1. The mesh is composed of unstructured tetrahedrons, enabling efficient incorporation of borehole geometry variations. The mesh is also refined around the electrodes within each borehole in order to improve modeling accuracy in the high potential gradient regions.

Fig. 6.1 shows the relative locations of the borehole and electrodes. Borehole K003 (aka K3), the stimulation well, deviates more than boreholes K2 and K4, and is slightly out of the K2-K4 plane at 40 m depth where the stimulation test was carried out. The K1 and K5 well pair were purposely deviated to form a plane perpendicular to K2-K4 around the K3 stimulation well. There were 29 electrodes deployed on each cable with 1.6-meter spacing between adjacent electrodes.
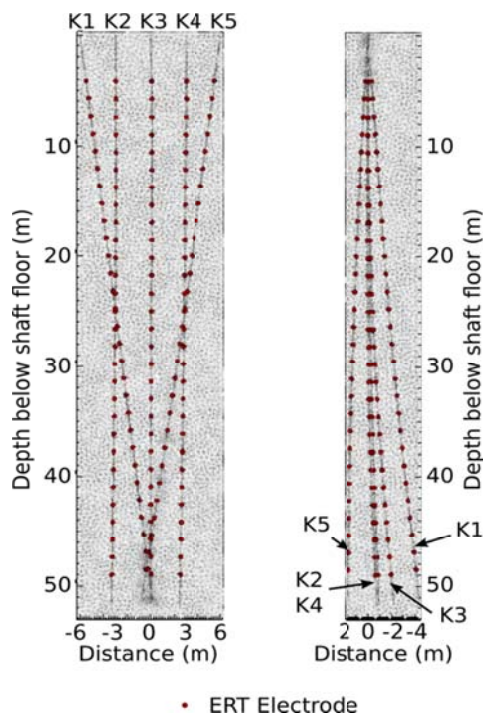

Figure 6.1. ERT computational mesh perpendicular to West Access Drift (left-hand figure) and parallel to the drift (right-hand figure) showing borehole and electrode locations in true dimension as derived from deviation logs. Note "shaft" should be "drift" in the axis labels.

6.2.3   Baseline ERT Imaging Constraints

Incorporation of the boreholes into the imaging mesh enables a number of constraints to be placed on the ERT images. These constraints remove the normal assumptions imposed on regularized inversions, such as a smoothly varying electrical conductivity. In particular, regularization constraints were removed across the borehole boundary, enabling the inversion to accommodate the actual sharp conductivity contrast that occurs across that boundary between the boreholes and the host rock. Within the boreholes, the starting model for the inversion was set to the assumed borehole fluid conductivity, but this starting model fluid conductivity was allowed to be modified by the inversion subject to being smoothly varying within the borehole. Fluid conductivities were allowed to vary because water samples collected from each well and analyzed after the stimulation revealed significantly different fluid conductivity between wells (from ~500 to >1000 µS/cm). Outside of the boreholes, the inversion used standard smoothing constraints for the baseline inversion.

6.2.4   Time-Lapse ERT Imaging Constraints

The objective of the time-lapse imaging was to identify the timing and location of changes in electrical conductivity caused by the fracturing and subsequent pressure-based stimulation events, thereby locating the fracture and determining fracture orientation, assuming there is sufficient resolution. Within the fracture zone, electrical conductivity is expected to increase, because the fluid-filled fracture provides a preferred pathway for electrical current when the fracture-fluid conductivity is larger than the host-rock conductivity. At all other locations, the conductivity should be equal to the baseline conductivity. This information was used to constrain the inversion to find a solution that (1) varied smoothly in space and time from baseline conditions, with preference for no change over time, and (2) was everywhere equal to or greater than baseline conditions. Given these constraints, the inversion changes the conductivity distribution from baseline conditions only if required to fit the data to the same degree as the baseline inversion data misfit.

6.2.5   Datasets and Results

Crosswell ERT data sets were collected in the K2-K4 plane before and after stimulation. To test for effects of interference between the ML-CASSM (See Section 6.5.1) and ERT data collection systems, ERT electrodes were co-deployed with the ML-CASSM system, and each system was run concurrently. Comparison of the ERT data sets collected with and without ML-CASSM displayed significant differences, and inversion of the ERT collected with ML-CASSM did not converge. This suggests the ERT data were contaminated when co-deployed with ML-CASSM system. For this reason, the ML-CASSM system was deployed in the K2-K4 plane, and the ERT system was deployed in the K1-K5 plane for time-lapse data acquisition during stimulation when simultaneous collection of both types of data was required.

The optimized survey collected during fracture simulation required approximately 10 minutes to execute, which provided the opportunity for a 10-minute time-resolution. Two baseline crosswell ERT data sets were collected in the K1-K5 well pair just prior to stimulation operations. One survey was collected before the initial fracturing event, and four surveys were collected during the five subsequent stimulation events. During each stimulation event, pressure within the packed-off zone was raised to approximately 2800 psi (19.3 MPa), which presumably sustained an open fracture aperture and cross-section for current flow, thereby increasing electrical conductivity of the fracture.

Each electrode deployment provided the opportunity to collect induced polarization data, and to analyze the utility of induced polarization inversion given the kISMET configuration of boreholes and electrodes. Several induced polarization surveys were collected in both the K2-K4 and K1-K5 planes. Visual inspection of the raw data revealed high levels of contamination in the phase measurements, likely due to

inductive coupling within the electrode cables. For this reason, no induced polarization inversions were attempted.

The baseline inversion image of electrical conductivity is shown in Fig. 6.2. The left-hand-side image shows the K2-K4 plane. The center and right-hand-side images show different views of the K1-K5 "plane," which twists around borehole K3. The conductivity shows steeply dipping structures spanning two orders of magnitude from 0.0001 S/m (10,000 ohm-m) to 0.01 S/m (100 ohm-m), with a periodicity in the vertical direction of approximately 4 m (13 ft). Inspection of repeat data sets and inversion results suggested noise levels (i.e., standard deviations) of approximately 10% of the observed transfer resistance in the K1-K5 plane and 5% of the observed transfer resistance in the K2-K4 plane. Based on these standard deviations, the histogram of weighted observed vs. simulated residuals is shown in Fig. 6.3.

The residual error for each measurement is defined as the difference between the simulated measurement and the observed measurement, divided by the standard deviation assigned to that measurement. Here the simulated measurement is the measurement computed given the conductivity distribution when the inversion has converged. If the data are appropriately weighted, then the normalized chi-squared value of the residual errors will be equal to unity. A histogram of the residual errors is shown in Fig. 6.3, which corresponds to a chi-squared value of 6.9. This indicates that the actual data noise is larger than the 10% and 5% specified for the K1-K5 and K2-K4 planes respectively. In this context, data noise is the combined contribution of random noise, deterministic noise, and any inaccuracies in the forward model. Given the specified noise levels, a chi-squared value of 6.9 at convergence is marginal, and suggests significant room for improvement and enhanced sensitivity of the ERT data to fracture if the source of noise can be addressed. Measures were taken to eliminate modeling inaccuracies as well as possible given competing objectives, but there are reasonable measures that can be taken in the future to significantly improve fidelity of the ERT data. For example, electrodes can be installed on the outside of a PVC casing that is grouted into the monitoring boreholes. This would isolate the two systems and enable each borehole to be used simultaneously for ML-CASSM and ERT monitoring.
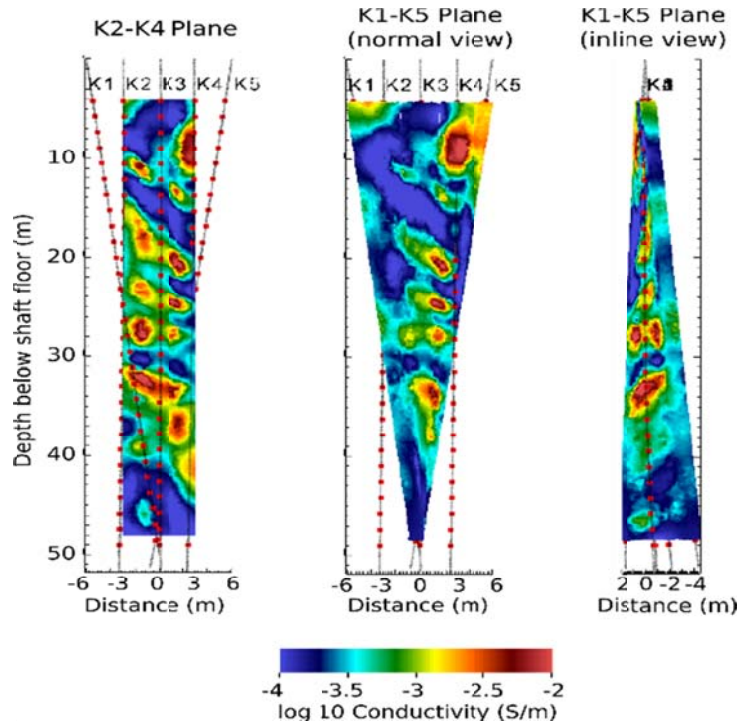
Figure 6.2. Baseline ERT inversion results. (Left-hand side), Bulk conductivity in the K2-K4 plane; (Center), Bulk conductivity in the K1-K5 "plane;" (Right-hand side), Bulk conductivity in the K1-K5 "plane" as viewed along the K2-K3-K4 plane from K1 to K5.
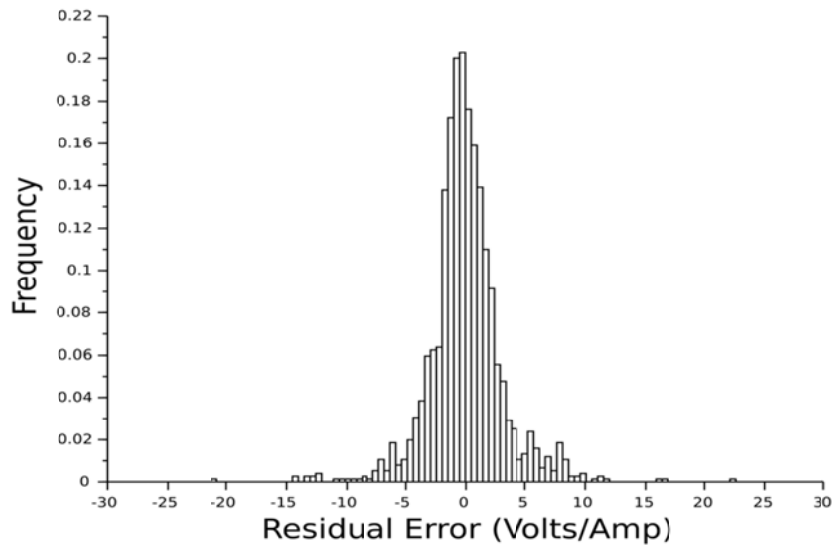
Figure 6.3. Weighted residual error histogram of baseline inversion data from the K1-K5 and K2-K4 planes corresponding to a normalized chi-squared value of 6.9.

In order for the fracture to be detected via time-lapse ERT monitoring during stimulation, fracture-induced changes in ERT measurement must exceed the data misfit residuals of the baseline inversion. The

six data sets collected in the K1-K5 plane during simulation were highly repeatable from baseline through to final stimulation, indicating that the ERT data were insensitive to the fracturing and stimulation events. Corresponding inversions revealed that each data set collected during fracturing and stimulation was adequately fit by the baseline inversion conductivity distribution, again indicating the absence of fracture signatures in the ERT data that were outside of the noise envelope.

6.2.6   ERT Conclusions and Future Directions

While baseline geological structures were revealed by the ERT survey with consistency across K2-K4 and K1-K5 planes, the fracture stimulation events did not create detectable changes in the electrical resistivity signatures. A few possible reasons should be explored in future efforts. For example, the post- stimulation ERT monitoring across the K2-K4 plane was collected after the release of the pressure in the packed-off zone, which would result in the closure of the fracture aperture and back flow of fracking fluid out of the fracture due to the high in situ stress. Such a process can effectively remove electrical conductivity changes associated with the fracture due to the lack of residual fluid within the fracture, resulting in minimal changes in the post-fracture electrical conductivity when compared to the baseline data. Meanwhile, while the data across the K1-K5 plane were collected during the stimulation events when the injection pressure was sustained and, presumably, the fracture aperture kept open, it is later revealed from the borehole logging data (discussed below) that K1-K5 plane is roughly 45-90 degrees out of plane with the fracture plane, resulting in less impact on electrical conductivity signatures from the fracture in this direction.

The ERT results suggest a few recommendations in order to enhance the possibility of fracture detection through mapping of electrical conductivity anomalies created by the fractures. First, the electrical conductivity between the fracture and the host rock needs to be enhanced. This can be achieved via the injection of a contrast agent/proppant/fluid with enhanced electrical conductivity that can leave a residue in the fracture even after fracture closes to ensure a sustained and maximized conductivity contrast. In addition, increase in the size of the fractures can help greatly to make fractures more detectable. We also note that more effective and targeted placement of the electrodes with respect to the fracture geometry could further enhance the chance of detection. This would include (1) for wells with casing, the placement of electrodes behind PVC casing to eliminate the large impact from borehole fluids, (2) use of higher electrode density in the targeted fracture zone, and (3) aligning the electrode arrays better with presumed fracture planes. When open hole deployment is the only option, a better control of borehole fluid conductivity and isolation of electrical noise from co-deployed equipment (e.g., CASSM) are needed to reduce noise level and possible electrical cross-talk. If casing is an option, PVC casing with ERT electrodes grouted into the annulus could be used with CASSM in the borehole for electrical isolation of the CASSM system from the ERT system.

6.3   Passive Seismic Monitoring

6.3.1   Induced Seismicity from Fracturing

A total of four locations were chosen to locate seismic detection instruments as part of the on-site data collected during the hydraulic fracturing experiment. The layout of the instrumentation is shown in Fig. 6.4. The recorders consisted of two 8-channel, 24-bit Kinemetrics Basalt seismic dataloggers, and the sensors were Episensor three-component accelerometers. Installation of each of the accelerometers located in the drift consisted of excavating through the drift ballast to bedrock, drilling 1.5 cm holes in which rebar was grouted, and pouring a concrete pier 20 cm in diameter. After the concrete cured, the accelerometers were bolted tightly to the pier. In addition to the accelerometers, a downhole geophone was installed in K2 at a depth of 20 m. All of the sensors were sampled at a rate of 1000 samples/sec.

The instrumentation measured the seismic signal in the drift near the injection borehole during the fracturing process. Coordination of time between the pump pressure and the seismic record was accomplished by striking a wooden block near accelerometer W, which also closed a circuit in the pump unit that was recorded as part of the pump digital data. This provided a means to correlate the seismic signal with the pump pressure signal.

Usable data were collected only from accelerometer W shown in Fig. 6.4. The response recorded from the vertical accelerometer channel during fracturing of the lowest fracture is shown in Fig. 6.5 and appears to correlate well with the pumping sequence. Fracturing performed at shallower depths does not appear to have as pronounced an effect and are less obvious on the seismic records. Preliminary analysis of the borehole geophone response did not produce data that exceeded the noise level. High acoustic noise resulted in low signal-to-noise and degraded the data substantially. Two of the accelerometer locations were positioned poorly with respect to the compressor and the fracture pumps because the seismic instrument sites were prepared prior to the determination of the final locations of fracture equipment. Drift space constraints and health-and-safety egress requirements limited the options for positioning of equipment during the fracturing and stimulation phases.
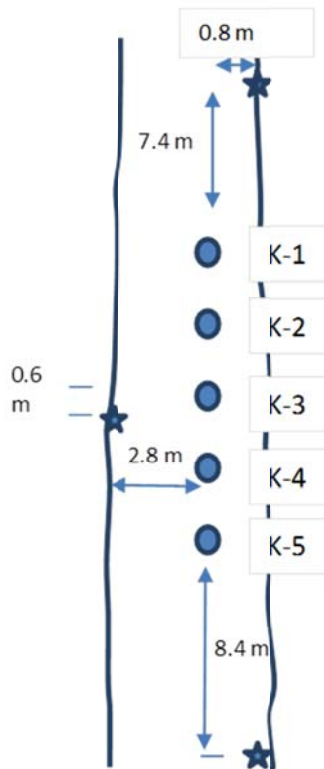
Figure 6.4. Arrangement of accelerometers (blue stars located in W, N, and S positions) with respect to the drift borehole geometry in the West Access Drift on the 4850L of SURF (Yates Shaft is toward the top of the figure). At this point only accelerometer (W) has produced usable data due to ambient noise in the drift. A geophone also was deployed in the K-2 borehole, where in this figure K-2, K-3, etc. = kISMET-002, kISMET-003, etc.
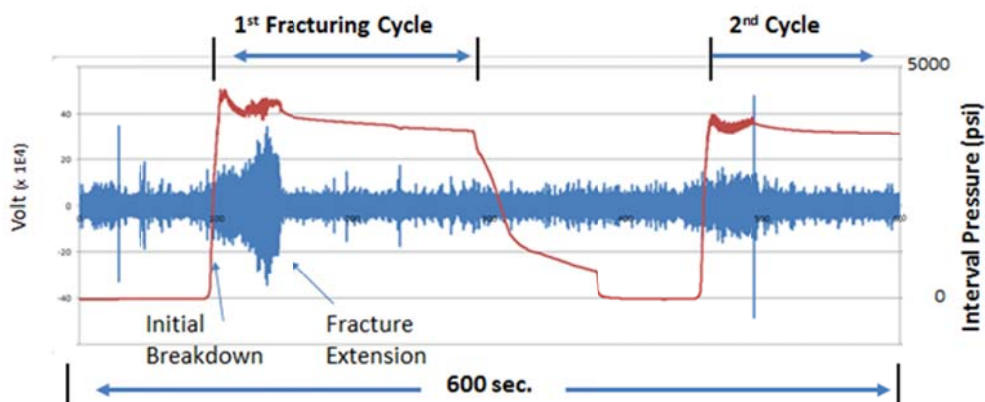
Figure 6.5. Seismic response detected by accelerometer W relative to fracturing pump pressure at a depth of 319 ft (97.25 m) from the borehole collar. The seismic data from the vertical channel were subjected to a bandpass filter between 290-310 Hz. The seismic response shows a good correlation with the pump pressure although seismic responses from fracturing at more shallow depths are not as well developed.

6.3.2   Summary of Passive Seismic Monitoring

Although recognizable response was recorded due to the fracturing, the amplitudes as shown in Fig. 6.5 were small. Experience from other accelerometer installations at SURF also suggests that the frequencies can be high, and the sampling rate of 1000 samples/sec probably under-represents the available frequencies that can be measured. It is apparent that accelerometers should include higher sampling rates as well as being grouted into boreholes to improve rock contact. This will remove the instrumentation from drift noises as well as provide better transmission from the surrounding rock. These steps also should allow the damaged zone in the wall adjacent to the drift to be avoided. This zone may alter the seismic velocity and may increase the attenuation in some instances. Although it was not possible to install accelerometers in boreholes for this small-scale experiment, emplacement of this type has been used to good effect in other parts of the SURF underground where accelerometers were emplaced in boreholes made with jackleg drills.

6.4   Borehole Logging

6.4.1   Overview of Tools and Deployment

Geophysical borehole logging is useful for characterizing lithology, texture, existing open and/or annealed fractures, borehole break-out, fracture-foliation orientation, and rock seismic velocities utilizing industry-standard borehole geophysics deploying deviation, acoustic- and optical-televiewer, and full waveform sonic tools:

Deviation Measurements: As reported in Chapter 2, borehole deviation was measured twice, once using a dedicated borehole deviation tool and a second time using the integrated deviation sensors on the optical televiewer. Sonde azimuth was estimated using a three-component (3C) flux-gate magnetometer while inclination was measured using a 3C accelerometer. Measurements were made every 10 cm from top-of-casing (TOC) to the bottom of each borehole (either 50 m or 100 m below grade surface).

Optical Televiewer Measurements: Borehole optical televiewer measurements were conducted for all five boreholes before stress and stimulation tests to provide information on pre-existing fractures,

textural variations, and other features of relevance prior to the fracture test. Post-stimulation optical logging was conducted only in the stimulation hole (kISMET-003) to help identify newly created fractures. Measurements were made every 2.9 cm from top-of-casing (TOC) to the bottom of each borehole (either 50 m (164 ft) or 100 m (328 ft) below the drift invert (floor)).

Acoustic Televiewer Measurements: Acoustic televiewer logs were focused on the stimulation borehole (kISMET-003) pre- and post-stimulation to help identify fractures. Measurements were made every 2.9 cm from top-of-casing (TOC) to the bottom of each borehole (either 50 m (164 ft) or 100 m (328 ft) below the drift invert (floor)). As discussed above, the acoustic televiewer was used as a backup tool for fracture identification and was proven to be very useful.

Full Waveform Sonic Measurements: Borehole full waveform sonic (FWS) measurements were made before stimulation events to help understand the stress heterogeneity of the host rock. It was conducted only in the stimulation well. Measurements were made every 0.2 m along the length of the boreholes at 15 kHz.

The borehole logging at kISMET was conducted using Mt. Sopris borehole logging tools in the kISMET-003 borehole before and after fracturing events to map induced fractures. Borehole logging was also carried out in the four monitoring boreholes for borehole and rock characterization.

6.4.2   Results

Prior to borehole logging, efforts to flush the boreholes of all suspended cuttings were made by inserting a hose attached to a pump to flood the well space. These efforts were successful as evidenced by optical televiewer imaging of fine scale foliations. Fig. 6.6 shows an example of the existing fracture and foliation features based on pre-hydraulic fracturing optical logs. The tadpole log on the right-hand side shows the direction of dip (degree coordinate of the location of the tadpole body) of the planar features that were selected to have greater than 80% confidence in the auto-picking module. Significant variability in rock foliation is apparent from the optical images, suggesting their potential impact on fracturing processes. No open fractures were identified from the optical logs of in kISMET-003. Optical images from the other boreholes were not processed at the time of the compilation of this report. The optical logs are useful for orienting the cores collected during drilling which are critical for the preparation and design of the laboratory experiments being performed at LBNL and Univ. of Wisconsin-Madison. Comparison of post-fracturing optical logs at the highest resolution did not result in the identification of the created fractures, possibly due to the small size of the fracture aperture and the overall dark color of the host rock.
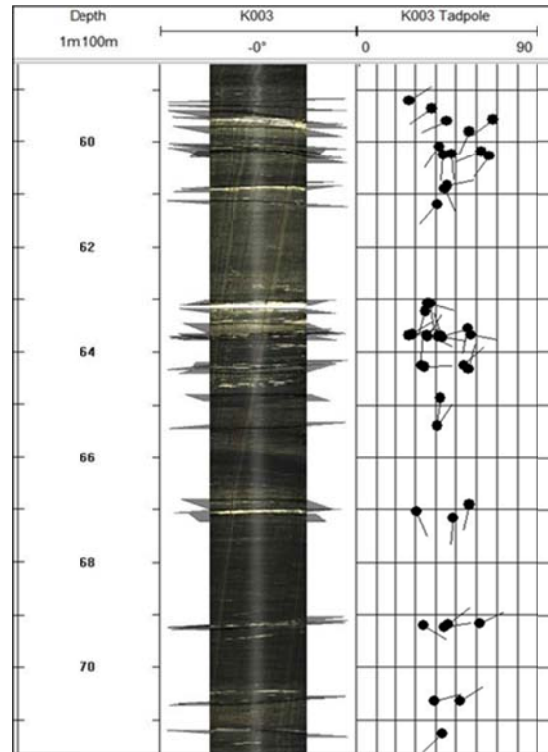
Figure 6.6. Portion of the kISMET-003 pre-test characterization log showing existing fracture and
foliation conditions. In the optical image attribute plane, the markers indicate the dip
directions of existing annealed fractures or foliations. The tadpole view on the right-hand side
gives the quantitative values for all picked features with a confidence interval greater than
80%. No open fractures were readily apparent.

Because optical logs could not be used to identify created fractures, acoustic televiewer logging was
conducted and successfully used to locate fractures created during the kISMET stress measurement and
stimulation tests. Fig. 6.7 shows a comparison between pre- and post-test acoustic logs along with the
post-stimulation optical logging results. Two selected intervals are shown in Fig. 6.7. At the 40 m depth
interval, clear images of produced fractures are observed in the central acoustic image (post fracture,
green dashed zones) compared to the same level in the pre-fracture image on the left-hand side. At the
next selected depth (60 m depth interval) another clear hydraulic fracture is observed. For depths greater
than ~60 m (197 ft), hydraulic fracturing occurred before the availability of the acoustic televiewer,
therefore no pre-fracture image is available. The induced fractures are not visible on the optical log shown
on the right-hand side of Fig. 6.7 likely due to the dark color of the rock. The fracture geometries
identified in the acoustic logs show a very consistent, near vertical plane extending in the east-west
direction (see Chapter 5 for discussion of stress orientation).
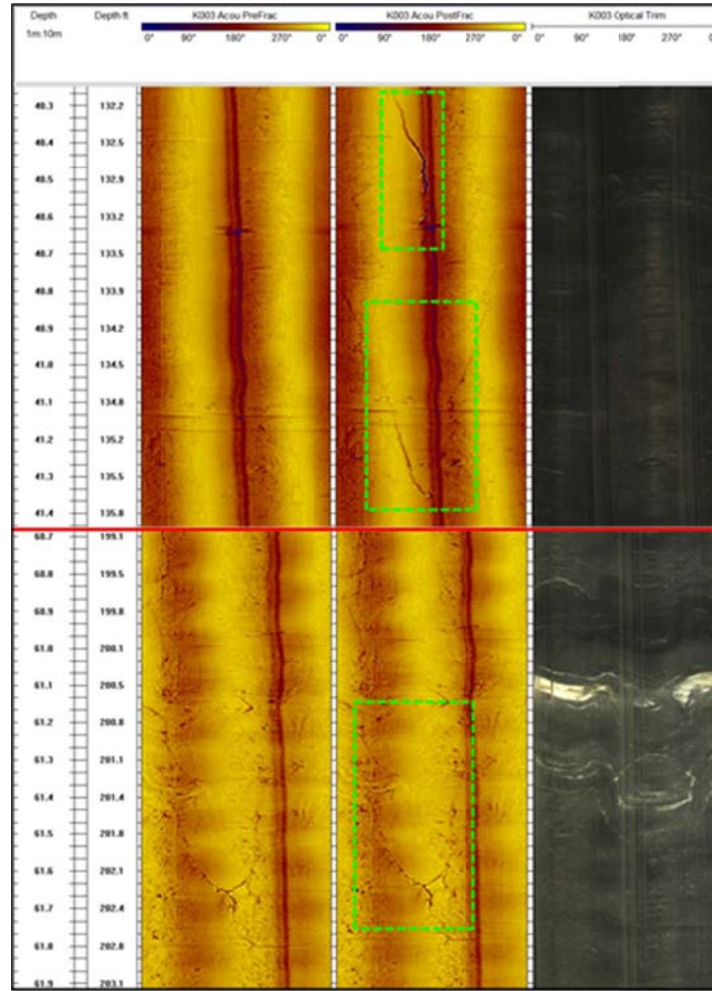
Figure 6.7. (a) Row of images above the red line show comparison of acoustic (pre- and post-fracture are left-hand side and center images, respectively) and optical televiewer logs for the ~40 m test zone defined by depth scale on the left-hand side. The induced fractures are outlined by the green dashed boxes in the acoustic televiewer post-fracture image (central image of top set). The fractures are not visible in the post-test optical log. (b) Row of images below the red line show two acoustic televiewer logs both of which are post-fracturing in the ~60 m test zone. The log shows the reproducibility of the acoustic image in detecting the hydraulic fracture. As in the prior interval, the fracture cannot be seen in the optical log due to the dark color of the rock.

Full Wave Form Sonic (FWS) logs were collected in kISMET-002, kISMET-003, and kISMET-004. FWS logs are useful mainly for providing both the P-wave (primary/compression wave) and the S-wave (shear wave) velocities. These were calculated from the arrival times in receivers using the three receivers of the tool, Rx1, Rx2, and Rx3. Fig. 6.8 shows the FWS log for kISMET-003.

The main value of having both P and S wave velocities is being able to calculate the dynamic elastic constants, Young's Modulus and Poisson's ratio. While these are usually slightly off the static values one obtains from compression or tension tests on cores, the FWS logs does show the range and scale of elastic variability. Elastic heterogeneity is one control on fracture propagation, as elastic contrasts can produce in situ stress contrasts. Portions of the rock with contrasting elastic properties may preferentially attract or divert a propagating fracture.

Figure 6.9 shows a preliminary assessment of the P and S velocities along with calculated Young's modulus and Poisson's ratio values from the stimulation hole kISMET-003. The dynamic Young's modulus values range from 56 to 86 GPa, which is not far off the static values (see Table 7.2). There is variability in properties on a scale of meters to tens of meters including a broad higher modulus section around 40 m, which is the stimulation zone depth.

Rock anisotropy may affect the FWS log results. As shown in the Fig. 3.4, laboratory measurements of velocity are strongly anisotropic and dependent on the orientation of the foliation. Future work will need to check if the variations in kISMET-003 of velocities and calculated properties may be related to variations in the foliation dip along the borehole.
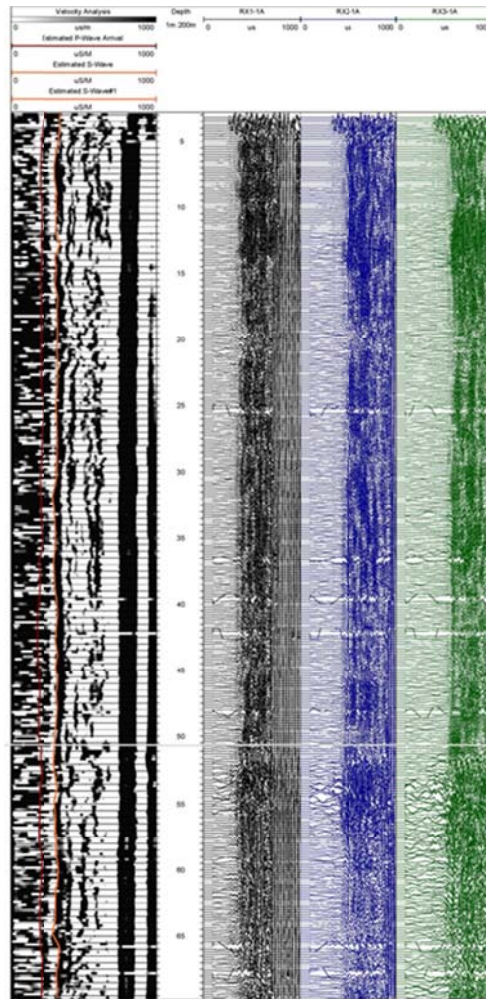
Figure 6.8. Full waveform sonic log for kISMET-003. Rx1 - Rx3 are the receivers in the sonic logging sonde with Rx3 being farther away from the source. The start of the wiggle traces shifts right from the left-hand side starting point for each receiver indicating a long wait time for the acoustic wave arrivals. The estimated P-wave (red line) and S-wave (yellow-orange line) arrival times are plotted on the Velocity Analysis curve (black and white) from which they were estimated. Those arrival times are then converted to a velocity.
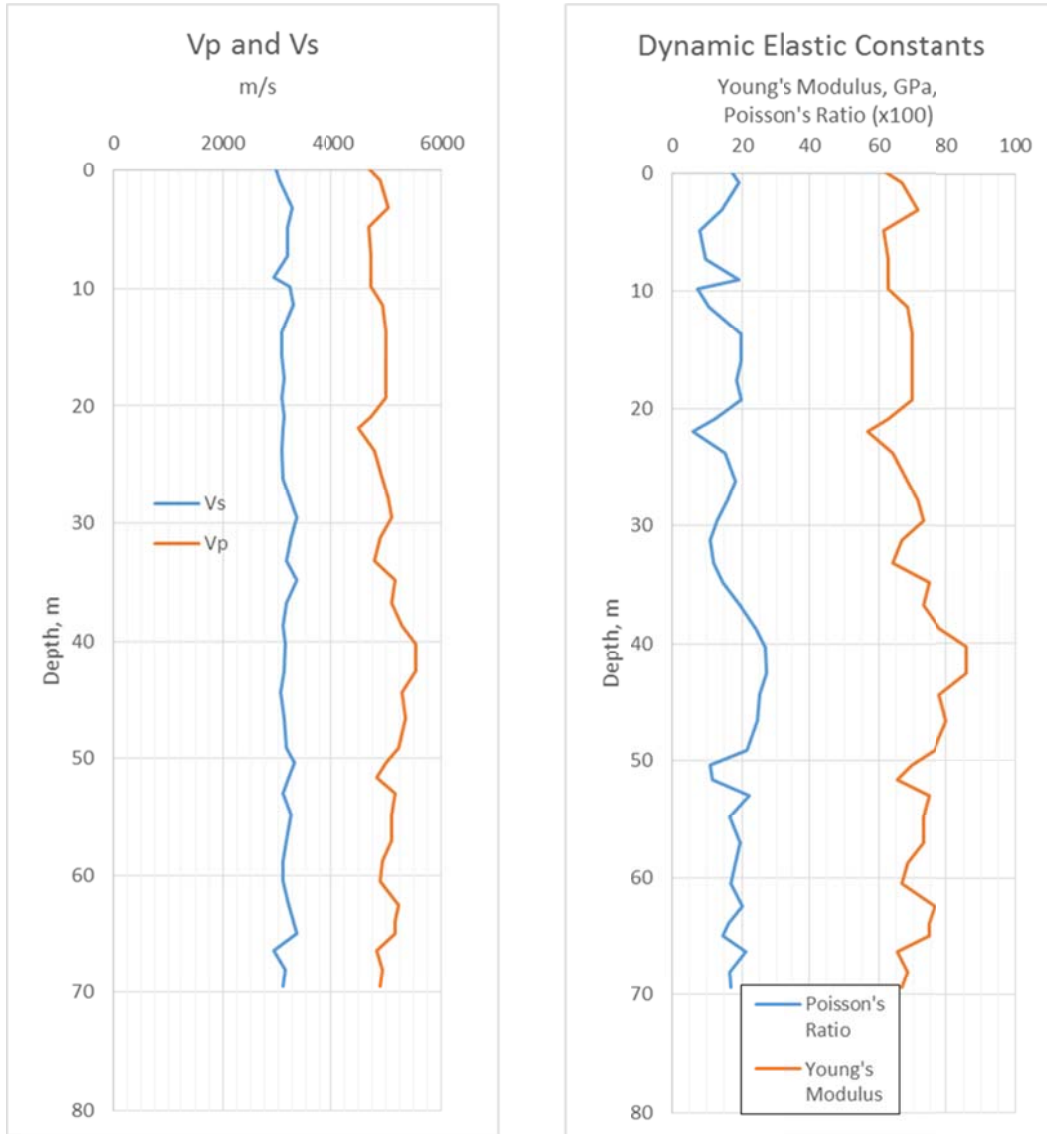
Figure 6.9. Preliminary full waveform sonic log for kISMET-003 with calculated dynamic elastic constants.

6.5   CASSM

Active source seismic characterization and monitoring was conducted during the experiment using ML-CASSM (Ajo-Franklin et al., 2011) deployed in the monitoring boreholes. Pre-fracturing crosswell seismic surveys were conducted across the K2-K4 plane by sequentially changing the position of the seismic sources and the 24-channel hydrophone arrays. A full-well seismic cross section was collected before the fracturing events. During the hydraulic stimulation of the depth interval at ~40 m (131 ft), CASSM monitoring was conducted across the K2-K4 plane, centering on the depth at ~40 m (131 ft) by positioning the hydrophone arrays. The analysis of the active source seismic data is in progress.

This page left intentionally blank.

7.   ANALYTICAL SOLUTIONS FOR ESTIMATING FRACTURE SIZE

Lead Author: Thomas Doe

7.1   Introduction

The kISMET hydraulic fracturing experiments allowed determination of the magnitude and orientation of the minimum and maximum horizontal stresses at the kISMET site. The experiments did not provide a direct measurement of fracture size. In this section, we describe the use of analytical solutions for assessing fracture size (Abé et al., 1976; Takahashi and Abé, 1987).

Two common conceptual models for hydraulic fractures are rectangular fractures, which grow into wings of constant height from a borehole (so-called biwings), and circular "penny" fractures. In a vertical borehole such as kISMET-003, rectangular fractures would also be vertical (Fig. 7.1). The rectangular fracture model is commonly applied in the oil and gas industry, where the geologic materials are usually (sub-) horizontally stratified, and the vertical growth of fractures is confined by layers with contrasting stresses and elastic properties. The main alternative to the rectangular fracture model is the circular fracture model where no such constraints on vertical fracture growth exist. Given the observation from acoustic logging that the kISMET fractures were not vertical but rather steeply dipping, and the fact that there are no apparent mechanical barriers to vertical fracture growth in the rock at the kISMET site, we assume the penny (circular) fracture conceptual model in our analysis.

Penny Fracture   Rectangular Fracture   kISMET 003 Fractures

Figure 7.1. Conceptual models of hydraulic fractures, and sketch of a few kISMET fractures (right-hand side).

7.2   Penny Fracture Model

Fracture mechanics models are well-suited for assessing hydraulic fracture growth. In such models, the internal fluid pressure of the injection is the primary driver for fracture growth. The criterion for fracture

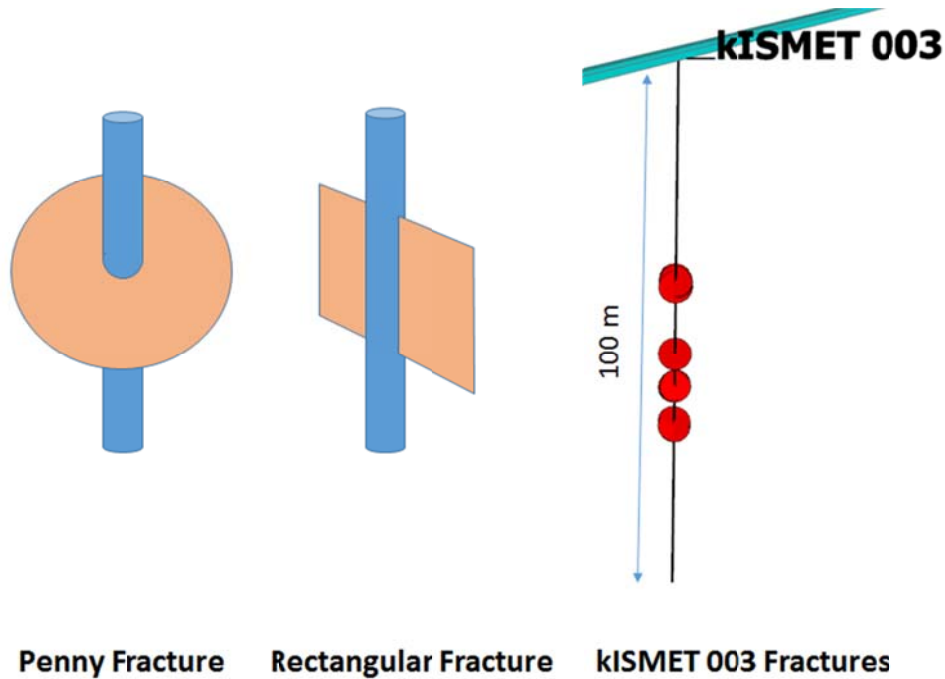extension is a balance between the stress intensity, which is the concentration of stress at the fracture tip, and fracture toughness, K_{IC}, which is the resistance of the material to fracture growth. The radius of growth for a circular fracture is a balance between the volume of fluid injected and the inflated volume of the fracture, minus the fluid volume that is lost into the permeable host rock or into pre-existing conductive fractures. The extent of the fracture will depend on this fluid balance as well as the modulus of elasticity, E, and the fracture toughness. Rocks with low modulus or large fracture toughness will produce shorter fractures with larger fracture apertures, e. On the other hand, stiffer rocks with large modulus values or smaller fracture toughness values will produce fractures with larger radius values but smaller apertures.

Takahashi and Abé (1987) provide the essential relationships of fracture radius and aperture to injected fluid volume:

$$R = \sqrt[5]{\left(\frac{Q_e D}{\pi^{3/2} K_{1C}}\right)^2} \tag{7.1}$$

$$D = \frac{3\pi E}{8\left(1 - v^2\right)\rho} \tag{7.2}$$

$$e_{max} = \frac{4\left(1 - v^2\right)}{E}\left(\frac{R}{\pi}\right)^{1/2} K_{1C} \tag{7.3}$$

where e_{max} is the aperture at the borehole wall, R is fracture radius, v is Poisson's ratio, and ρ is the fluid density. D is a lumped parameter and Q_e is the effective fluid mass injected (total injected mass minus leak off).

7.3   Fracture Radius Estimations for the kISMET Stimulation Test

7.3.1   Description of the Stimulation Test

The stimulation test was run at a depth of 40.28 m in borehole kISMET-003. The test included six pressurization cycles (Fig. 7.2). The first cycle was a standard stress measurement cycle of about three minutes to initiate the fracture. This cycle was followed by five fracture extension cycles with flow rates of approximately 0.5 liters per minute (lpm) and injection durations of 10 to 15 minutes followed by a brief shut in. Between each cycle the test zone pressure was bled to atmospheric pressure while measuring the flow rate. Each cycle achieved stable injection pressure of about 20 MPa. Fig. 7.2 shows the pressures and flow rates along with the cumulative flow of the entire test.

Table 7.1 gives the rates and volumes for the stimulation test by cycle. The total injection fluid volume was 41.8 liters. The volume from bleed-back periods from the five cycles totaled -13.8 liters leaving a net fluid injection volume of 28.1 liters. The measured fluid recovery was 34% of the total injection volume; however, the actual amount may be slightly greater due to flows that occurred below the resolution of the flowmeter.
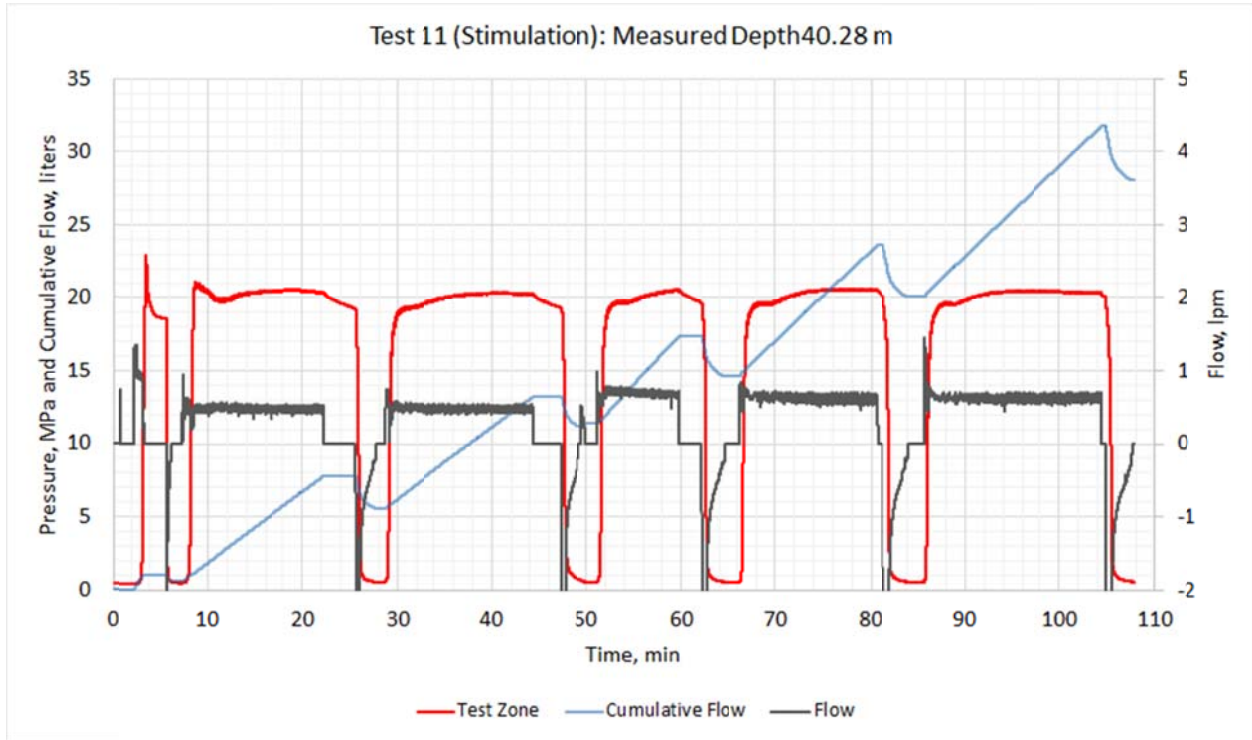
Figure 7.2. Pressure, flow, and cumulative flow for kISMET stimulation test.

Table 7.1. Rates and volumes for kISMET stimulation test (Test 11).

	Cumulative Time		Injection Duration	Cumulative Volume			Rate	Volumes	
	minutes			liters			l/m	liters	
	Start	End		Start	End	Bleed		Injected	Bleed Back
Cycle 1 Fracture	2.34	3.15	0.81	0.0	1.0	0.6	1.24	1.0	-0.4
Cycle 2 Stimulation	8.43	23.33	14.90	0.6	7.8	5.6	0.48	7.2	-2.2
Cycle 3 Stimulation	26.67	44.15	17.48	5.6	13.2	11.4	0.44	7.6	-1.8
Cycle 4 Stimulation	51.67	59.78	8.11	11.4	17.4	14.6	0.74	6.0	-2.8
Cycle 5 Stimulation	66.24	80.66	14.42	14.6	23.5	20.1	0.61	8.9	-3.4
Cycle 6 Stimulation	86.68	104.40	17.72	20.1	31.2	28.1	0.63	11.2	-3.2
Totals			73.44					41.8	-13.8
Net Injected								28.1	

7.3.2   Fracture Radius Calculations for Impermeable Rock

Low porosity igneous and metamorphic rocks are often assumed to be impermeable for the purposes of fracture design. In the following sections, we will use the Takahashi and Abé (1987) equations to estimate the fracture sizes that were produced in the kISMET stimulation for both the impermeable rock case (no leak-off) and the case of low-permeability rock (non-zero leak-off).

The fluid that is injected in a hydraulic fracture stimulation test goes into fracture propagation and into the rock itself as leak-off. Distinguishing between these components is very important for fracture radius estimation as the leaked-off fluid does not contribute fracture propagation. On the other hand, estimating the leak-off has practical significance for hydraulic fractures as it affects prediction of oil and gas flow from unconventional wells or the potential for injecting fluids or gases into rock for disposal.

For the impermeable rock case described in this subsection, we will assume that all of the injected water goes into fracture creation, i.e., the volume that is creating the fractures is the net volume of injected water minus the bleed back. For the penny crack calculations, we take the rock properties from the data compiled by Vigilante (2016) as shown in Table 7.2. The Young's modulus and Poisson's ratio are taken as averages for tests parallel and perpendicular to foliation or 71.4 GPa and 0.22 respectively. For fracture toughness, we are using a generic value from Atkinson and Meredith (1987) for hard rock of 1.0 MPa-m$^{1/2}$. Water density is taken as 1000 kg/m^3. These values contrast with those used in Section 4m which were $E = 41$ GPa and $v = 0.23$. The higher values of E used in this calculation result in larger fracture radius and smaller aperture at the borehole.

Table 7.2. Rock elastic properties for fracture size estimates

Property	Units	Hladysz and Erickson, 1984		RESPEC [*]	
		Homestake Formation	Poorman Formation	DUSEL Amphibolite	
E_1	GPa	87.5	93.1	E High	103
E_2		41.3	49.7	E Mean	89
E_3		62.1	94.5	E Low	69
$E_1 - E_2$ Average		64.4	71.4		
ν_{12}	-	0.18	0.15	ν High	0.25
ν_{23}		0.18	0.29	ν Mean	0.23
ν_{31}		0.19	0.22	ν Low	0.14
ν Average		0.18	0.22		0.21

  * Mellegard et al. (2010)

In Table 7.3 we show the results of the analytical radius calculations by stimulation cycle. The growth in fracture radius and area with injected volume appears in Fig. 7.3. The fracture initiation cycle was intentionally small in volume, and developed a fracture with a calculated radius of 2 m for the 1 liter of water injected. The analytical solutions suggest that the fracture expanded through stimulation Cycles 2 to 6 up to a radius of 7.9 m (26 ft), with relatively small radial growth in the last cycle. Fracture aperture values grow from 4.3×10^{-5} m to 8.5×10^{-5} m (0.043 mm to 0.085 mm) from Cycle 1 to Cycle 6.

Table 7.3. Fracture radius, area, and aperture calculations using equations of Takahashi and Abé (1987) for impermeable rock (Eqs. 7.1-7.3).

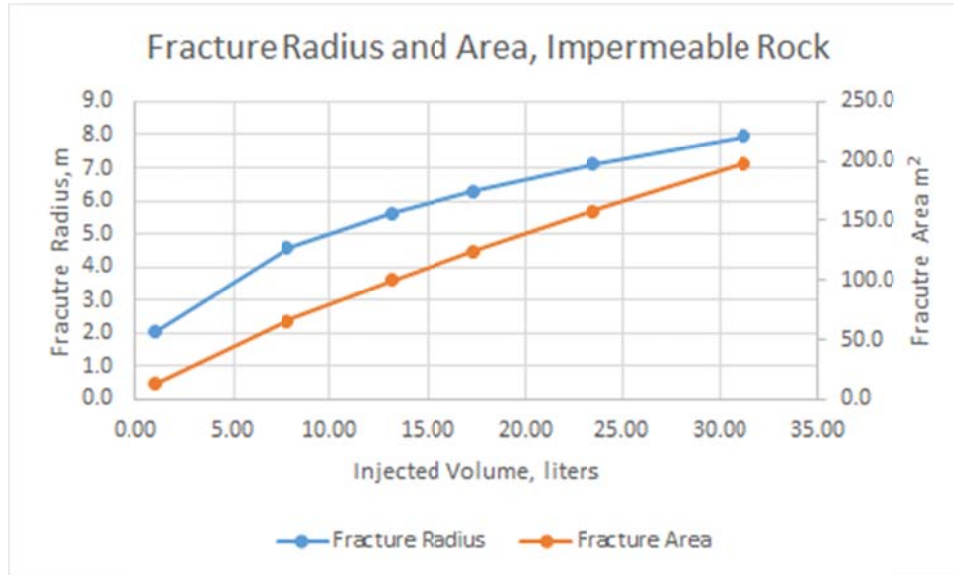| Cycle	Rate lpm	Duration min	Net Injected Volume liters	Radius m	Area m^2	Aperture at Borehole m	Fracture Propagation Resistance MPa
Cycle 1	1.2	0.81	1.01	2.0	12.7	4.27E-05	0.62
Cycle 2	0.5	14.90	7.80	4.6	65.4	6.42E-05	0.41
Cycle 3	0.4	17.48	13.20	5.6	99.6	7.14E-05	0.37
Cycle 4	0.7	8.11	17.40	6.3	124.3	7.54E-05	0.35
Cycle 5	0.6	14.42	23.50	7.1	158.1	8.01E-05	0.33
Cycle 6	0.6	17.72	31.20	7.9	198.3	8.48E-05	0.31

Figure 7.3. Fracture area and radius for impermeable rock.

7.3.3   Fracture Radius Calculations for Low-Permeability Rock

The Takahashi and Abé (1987) equations do not include a leak-off term, hence the consideration of leak-off into low-permeability rock described here requires using a bounding calculation. The bounding calculation uses two key assumptions. First, we assume that all fluid that was not recovered by the bleed-off disappeared as leak-off into the rock. Second, the leak off volume calculation assumes that the fracture was created instantaneously rather than incrementally.

The flow rate from a fracture face into the rock follows simple diffusion equation where the rate declines with the square root of fracture exposure time. In reality the exposure "clock" for each increment of fracture growth starts when its fracture face is exposed to flow, thus the flow rate to portions of the fracture close to the source will have decayed earlier than portions near the final fracture tip. Therefore the assumption that the fracture appears instantaneously is not accurate, but it serves to provide at least an order of magnitude indication of possible leak-off rates. For the first assumption, we assume that the bleed-off volumes for each cycle represent the fluid that created fracture growth.

Using the bleed-off volumes for calculating fracture radius gives somewhat lower radius values than the impermeable rock case as shown in Table 7.4 and Fig. 7.4. The radius values vary from 1.4 m in the initial stimulation to 5.7 m at the end of Cycle 6. Fracture area values vary from 6.4 m^2 in the first cycle to 103.2 m^2 after Cycle 6. The radius values are approximately 70% of the impermeable case, while the fracture surface areas are approximately 50% of the impermeable case. This comparison of area is sensible given that the impermeable case has a volume available for fracture growth of 28.1 liters compared with a volume available for fracture growth of 13.8 liters for the low permeability case.

Table 7.4. Fracture radius, area, and aperture calculations with leak-off into a low permeability rock.

Cycle	Volume	Cumulative Volume	Radius	Area	Aperture at Borehole
	liters		m	m^2	m
Cycle 1	0.43	0.43	1.4	6.4	3.60E-05
Cycle 2	2.23	2.66	3.0	27.7	5.18E-05
Cycle 3	1.81	4.47	3.7	41.9	5.75E-05
Cycle 4	2.76	7.23	4.4	61.6	6.33E-05
Cycle 5	3.39	10.62	5.2	83.7	6.83E-05
Cycle 6	3.17	13.79	5.7	103.2	7.20E-05
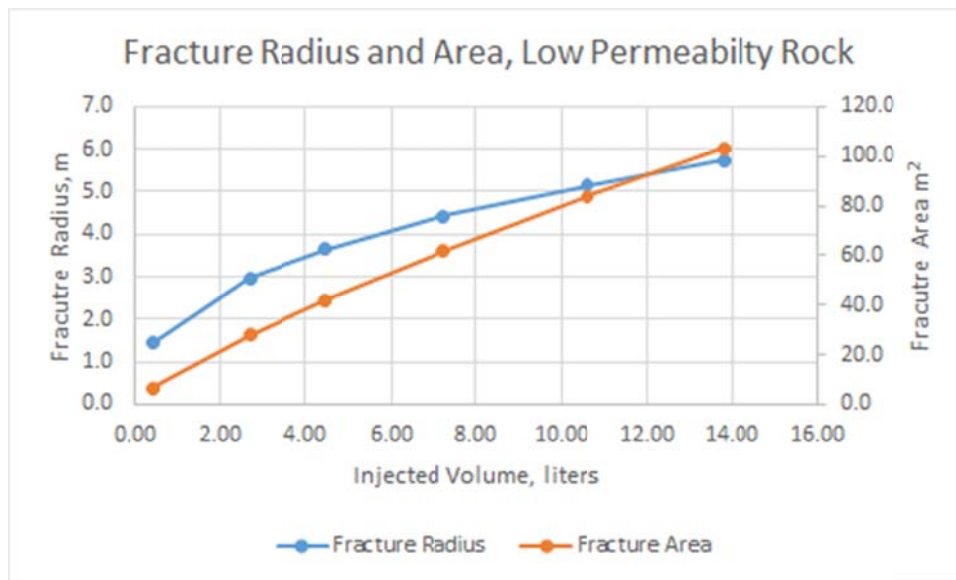
Figure 7.4. Fracture area and radius for low permeability rock.

Our assumption that the water not recovered in bleed-off flowed into the rock as leak-off can be checked, at least in an order-of-magnitude sense, using a simple linear diffusion model of flow from the fracture to the rock. For this we use Carslaw and Jaeger (1959, Ch.2, Eq. 11)

$$Q = 2\frac{KH}{\sqrt{\pi \eta t}}$$

(7.4)

where Q is flow rate per unit area, K is the hydraulic conductivity of the rock, H is the hydraulic head arising from the difference in pressure between the fracture volume and the initial pore pressure the rock, and η is the hydraulic diffusivity. For this calculation, we used a hydraulic conductivity of 1×10^{-12} m/s, which is equivalent to a permeability of 1×10^{-19} m^2. For diffusivity, we used 1×10^{-6} m^2/s. These are typical values for water in unfractured, low-permeability metamorphic and igneous rock (Song et al., 2004; Morrow et al.. 1994). The hydraulic head for these calculations is 1500 m, which is based on the head equivalent of the 20 MPa injection pressure and assumption of a 5 MPa pore pressure.

Table 7.5 presents the calculated leak off volumes as a function of time and fracture radius. The key number to note in Table 7.5 is the leak-off volume at 75 minutes for a 6 m-radius fracture. This corresponds to our fracture size calculation of 5.7 meters after 73.4 minutes of stimulation. This value from the leak-off calculation is 25.7 liters, which compares closely to the observed fluid loss of 28.1 liters if we assume the fluid that was not recovered entered the rock.

Table 7.5. Leak-off volumes for rock with 1×10^{-19} m^2 permeability and 1×10^{-6} m^2/s hydraulic diffusivity versus time and fracture area.

Time		Rate/m^2	Cumulative Volume	Fracture Radius, m				
				1	3	6	10	15
sec	min	m3/s	m3	Leak Off Volume, liters				
10	0.17	5.4E-07	1.1E-05	0.03	0.3	1.2	3.4	7.6
30	0.5	3.1E-07	1.9E-05	0.06	0.5	2.1	5.8	13.1
60	1	2.2E-07	2.6E-05	0.08	0.7	3.0	8.2	18.5
300	5	9.8E-08	5.9E-05	0.18	1.7	6.6	18.4	41.4
600	10	6.9E-08	8.3E-05	0.26	2.3	9.4	26.0	58.6
900	15	5.6E-08	1.0E-04	0.32	2.9	11.5	31.9	71.8
4500	75	2.5E-08	2.3E-04	0.71	6.4	25.7	71.3	160.5

One should not make too much of the close correspondence of the fracture radius and flow volume for this low-permeability case, as there is considerable uncertainty about the hydraulic properties of the rock. Nonetheless, the magnitude of the possible leak-off volumes may be a bit surprising in light of the polished low-permeability appearance of the core (e.g., see Figs. 2.13 and 2.14); however, it is a good illustration of how a large surface area and injection pressure can offset a low permeability to create significant flow rates over the fracture surface. This observation may be significant when considering the potential for storage and access to storage in rocks viewed to have very small permeability and porosity, e.g., CO_2 storage in fractured carbonate reservoirs (e.g., Zhou et al., 2017). This result further motivates our laboratory experimental program, which is planning to make permeability measurements on kISMET core.

7.3.4   Aperture and Propagation Resistance

The fracture aperture is not assumed but follows from the constraints of the combined effects of the elastic properties and fracture toughness. Takahashi and Abé (1987) provide analytical solutions for the aperture as a function of radius.

The form of a pressurized fracture is elliptical with radius as shown in Figure 7.5and is the aperture given by combining Takahashi and Abé's (1987) equations 7.3 and 7.6 to give

$$e(r) = \frac{4K_{1C}(1-v^2)}{E\sqrt{\pi}} \left(\frac{R^2 - r^2}{R} \right)^{1/2} \tag{7.5}$$

Where r is the radial distance within the fracture and R is the total fracture radius.
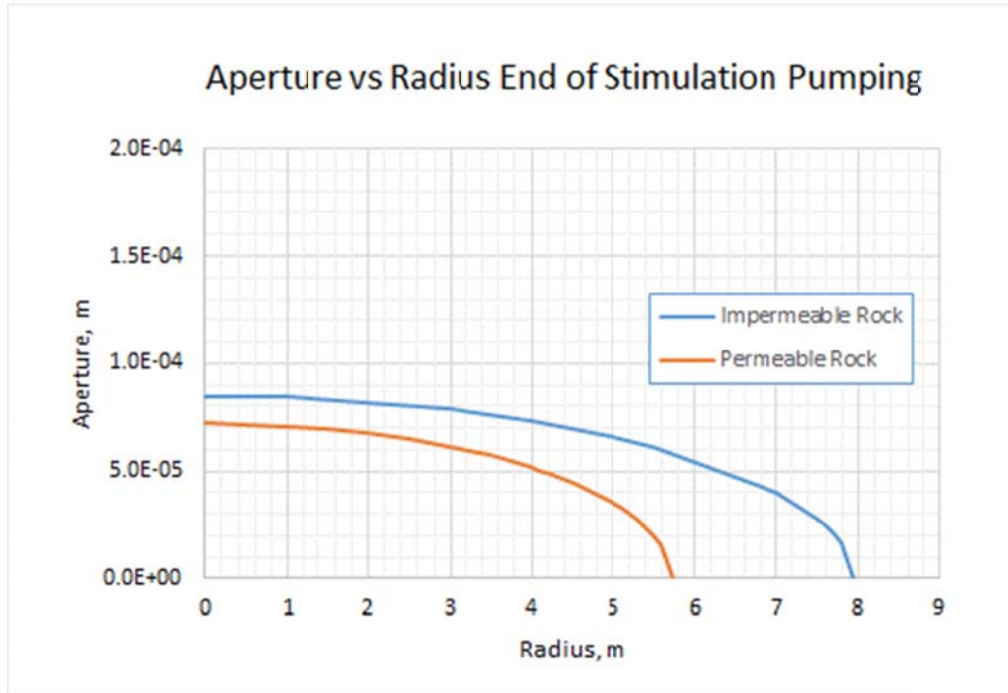
Figure 7.4. Aperture versus distance from borehole for impermeable and permeable cases.

The propagation resistance is the pressure required to extend that fracture once it has reached a given radius. Based on fracture mechanics, the effective tensile strength of the fracture comes from the balance stress intensity created by the pumping pressure in the fracture, p_{Pump} compared with σ_{HMin} against the fracture toughness of the rock. For case of a propagating hydraulic fracture the stress intensity increases as the fracture becomes larger because of the total load on the fracture face and is given by Takahashi and Abé (1987) as

$$p_{Pump} - \sigma_{Hmin} = \frac{K_{1C}}{2}\sqrt{\frac{\pi}{R}} \tag{7.6}$$

The propagation resistance for the end of each cycle in the stimulation experiment appears in Table 7.3 and Figure 7.5.

Figure 7.5. Propagation resistance versus radius

8.   SITE-WIDE STRESS ANALYSIS

Lead Author: Thomas Doe

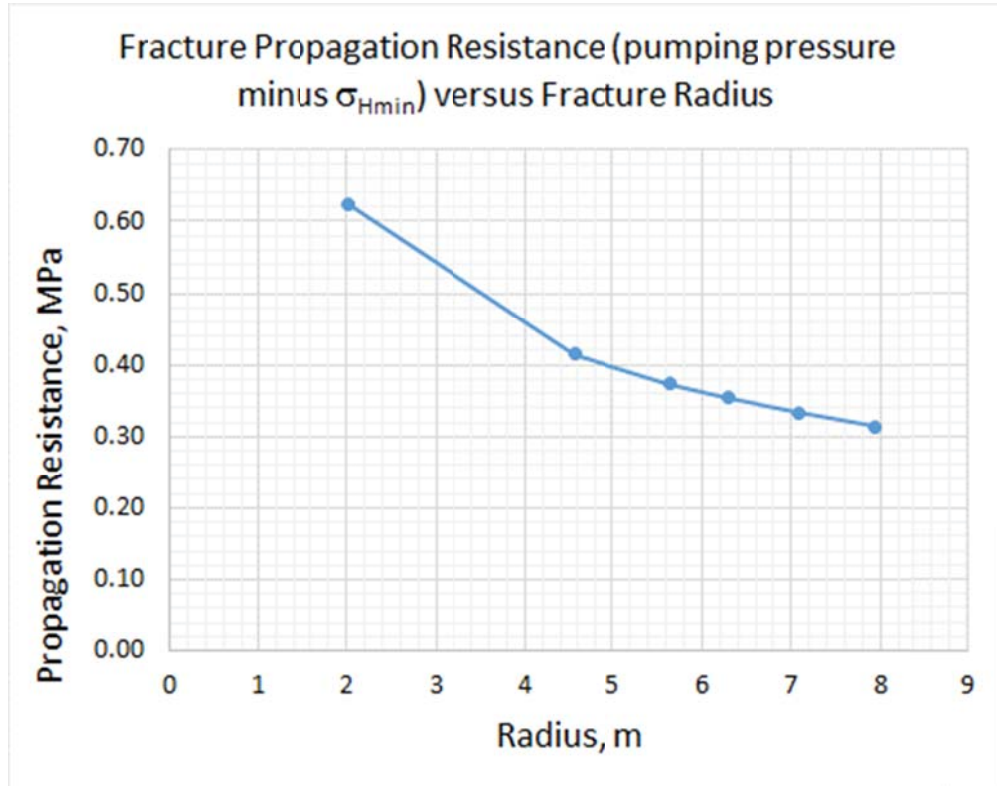## 8.1   Stress Indicators Near the kISMET Site

The kISMET site benefits from the extensive site characterization program that was carried out as part of the Deep Underground Science and Engineering Laboratory (DUSEL) program (Golder Assoc., 2010), which was exploring the use of the Homestake Mine for expanded physics experimentation, as well as potentially broadening the base of support to geoscience areas (e.g., Oldenburg et al., 2012).

All of the numerous methods for determining in situ stress, e.g., overcoring, hydraulic fracturing, and others, have potential shortcomings. For overcoring, the major challenges include the small scale of strain or deformation measurement as well as challenges in determining elastic properties, particularly when the rock is heterogeneous and anisotropic. The main challenge of hydraulic fracturing is the determination of the maximum horizontal stress because the stress concentration around the borehole and its interaction with micro-fractures and other flaws are difficult to assess.

Despite the challenges associated with any individual stress measurement method, the assessment of stress in a given site benefits from the integration of multiple measurement methods and stress indicators (Lucier et al., 2009). Among the most promising developments in this area is the integration of borehole breakouts and hydraulic fractures, which has become the standard for assessing in situ stress in oil and gas reservoirs (Zoback, 2007).

8.2   Borehole Breakouts

Borehole breakouts are stress-induced failures of borehole walls. They occur when the stresses acting on a borehole wall are great enough to produce shear or compressional failure. As shown in Fig. 5.12, borehole breakouts appear 90° from hydraulic fractures if both are present, as the hydraulic fractures occur in the direction where the borehole compression is the least, and breakouts occur where the compression is the greatest.

Borehole breakouts were noted in many of the sub-horizontal site characterization boreholes that were drilled for the DUSEL program. The exploration program ran image logs in all of the continuously-cored, sub-horizontal boreholes--optical in dry, updip holes and acoustic in water-filled, downdip holes— amounting to a total of 1640 m of borehole logging. The locations of the DUSEL boreholes are shown in Fig. 8.1.

Geologically, the DUSEL program focused on large cavern locations in the Yates Formation, which is an amphibolite. A swarm of Tertiary rhyolite dikes complicates the geomechanics of the DUSEL area. In contrast, the kISMET site was intentionally located in the Poorman Formation, which is dominantly phyllite and schist, weaker rocks than both the rhyolite and the amphibolite.

The image logs from the DUSEL boreholes showed widespread breakouts having variable intensities and orientations in different boreholes and different portions of boreholes (Fig. 8.1). Fig. 8.2 shows an example of an optical televiewer log of breakouts in DUSEL Borehole J. Some general observations and preliminary interpretations are:

- Breakouts are all in amphibolite or schist/phyllite, usually near rhyolite dikes, which do not contain breakouts.

- Overall orientation suggests the maximum principal stress is close to, but somewhat off, vertical.

- In the vicinity of the DUSEL large caverns, there may be a rotation of the breakouts indicating variable in situ stress regimes may be present.

Two DUSEL boreholes, Borehole J and Borehole D are particularly relevant to determining stresses at the kISMET site. Borehole J is the closest DUSEL borehole to the kISMET site at a distance of approximately 90 m. The borehole has a trend of 128° with an upward plunge of 2.4°. Unlike the other DUSEL boreholes, Borehole J is entirely in Poorman Formation phyllite and schist with cross-cutting rhyolite dikes. Other DUSEL boreholes are dominantly in Yates amphibolite. Borehole D is an approximately 400 m long borehole trending 204° with an upward inclination of 8.5°. While it is dominantly in the Yates Formation, it terminates in Poorman Formation near Borehole J. Despite being in similar rock, the intensity of breakout development is quite different between the two holes. Most of Borehole J, with the exception of the rhyolite sections, contains breakouts, while breakouts are infrequent in Borehole D, which differs in orientation by approximately 76°. Fig. 8.3 is a visualization of the kISMET area showing the hydraulic fractures and breakouts in Boreholes J and the end of Borehole D.

The Borehole J breakouts are sub-horizontal with a pole trending 210° and plunging 70° (Fig. 8.4). In contrast to the sub-horizontal Borehole J, there are no breakouts in the vertical kISMET boreholes. Assuming similar rock properties and stresses, this observation would suggest that the difference between the vertical and horizontal stresses in Borehole J is greater than the difference between the maximum and minimum horizontal stresses in kISMET-003. This implies that the vertical stress is the maximum principal stress. See also the discussion in Section 5.6.2.

The integrated interpretation of previous stress measurements (e.g., Vigilante, 2016), the hydraulic fracturing stress measurements for kISMET (this report), and stress indicators like borehole breakouts (the DUSEL reports) is a current kISMET activity carried out under a subcontract with Prof. Mark Zoback at Stanford University.
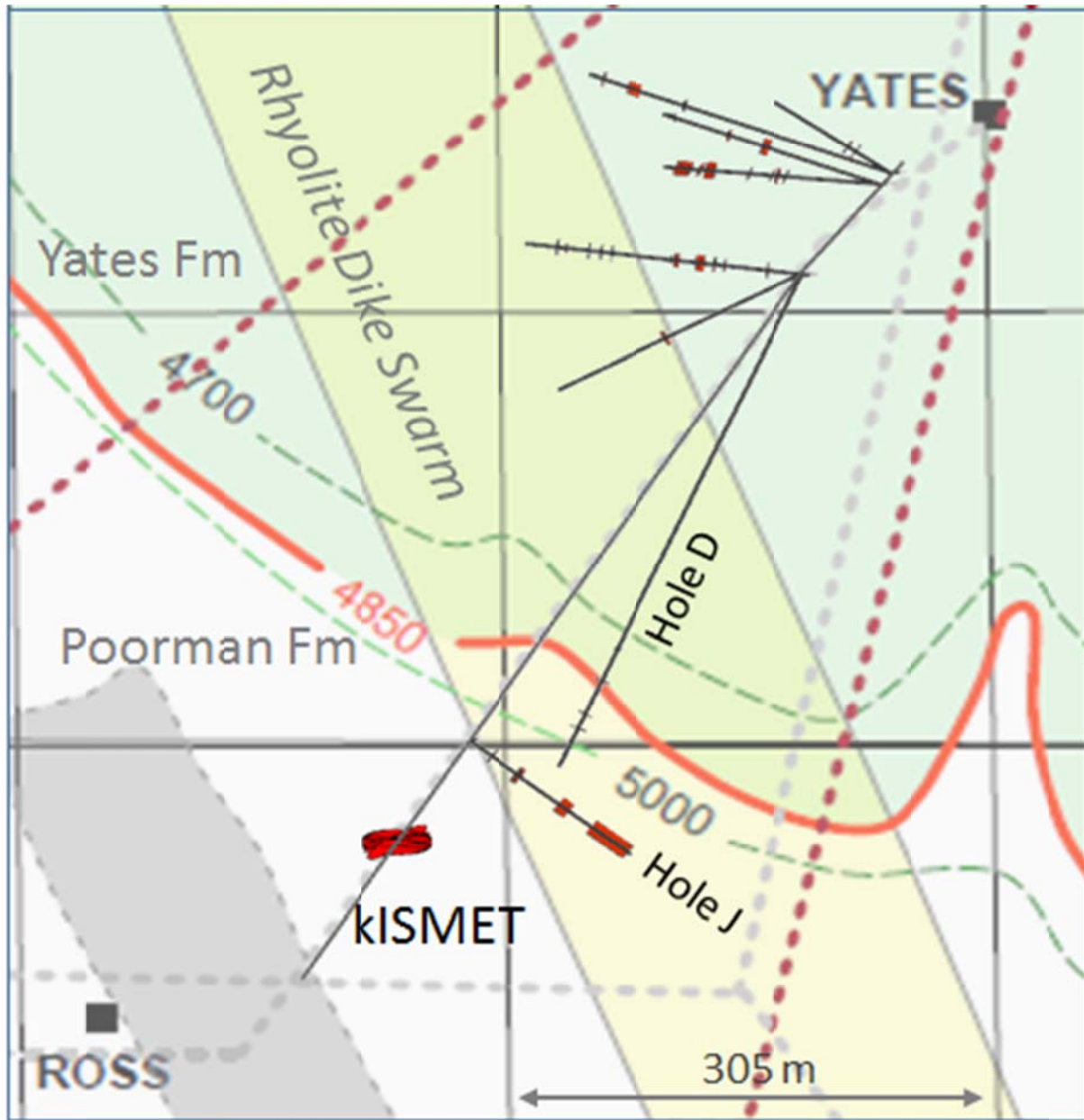
Figure 8.1. Geology of 4850L with DUSEL boreholes and locations of breakouts (red). Also shown are the kISMET site and the hydraulic fracture orientations from stress measurements.

Figure 8.2. Borehole breakouts in DUSEL hole J.

Figure 8.3. Visualization of hydraulic fractures and borehole breakouts. Rhyolite sections of borehole BH-3 are shown in white. For scale, borehole kISMET-003 is 100 m (328 ft) long. The end of Borehole D appears in the upper right (black terminating line subparallel to West Access Drift (aqua)).

Figure 8.4. Stereographic projection of poles to Borehole J breakouts

9.   CONCLUSIONS AND RESEARCH NEEDS

Lead Authors: Curt Oldenburg and Pat Dobson
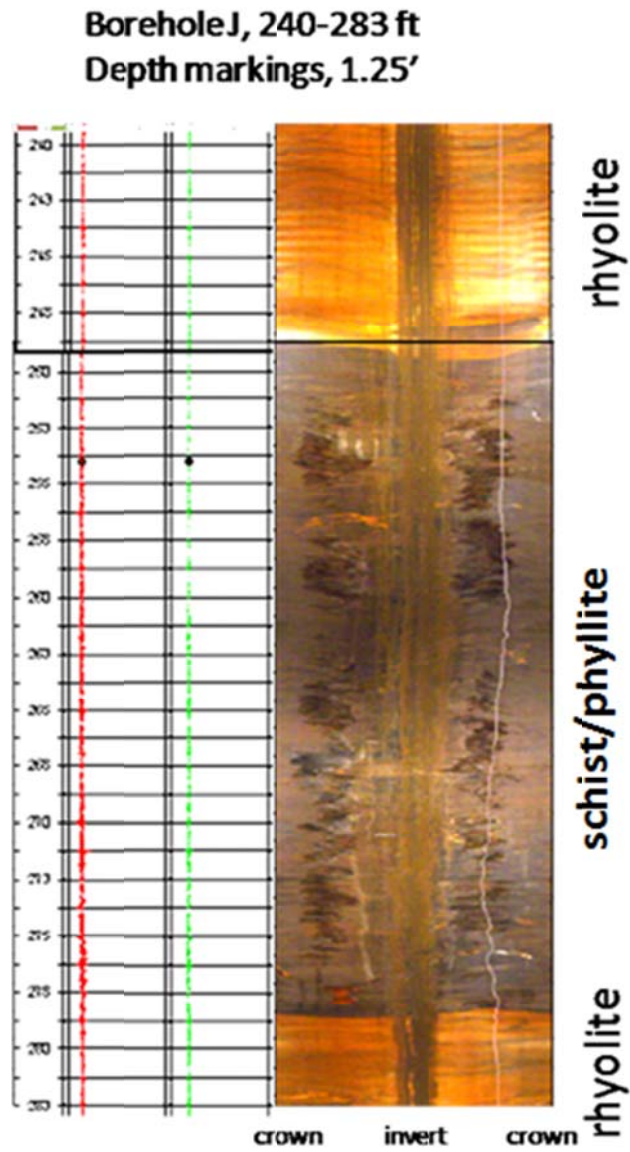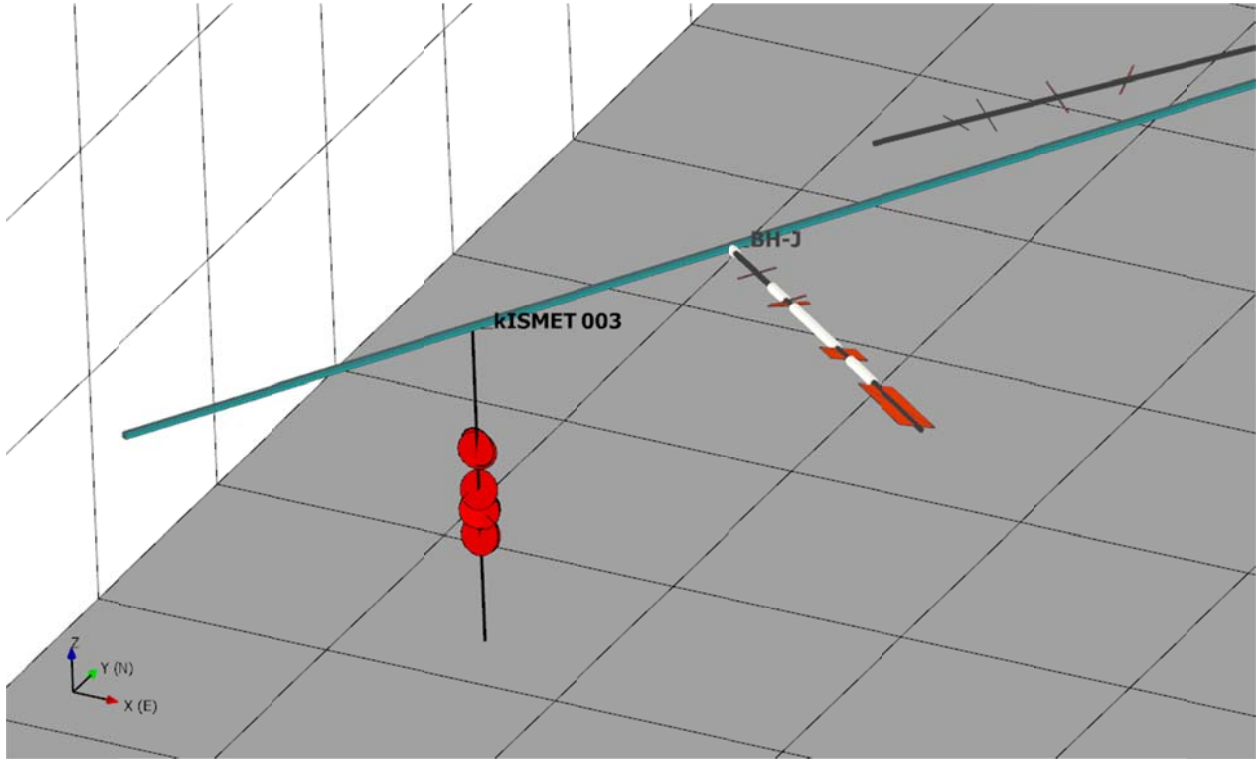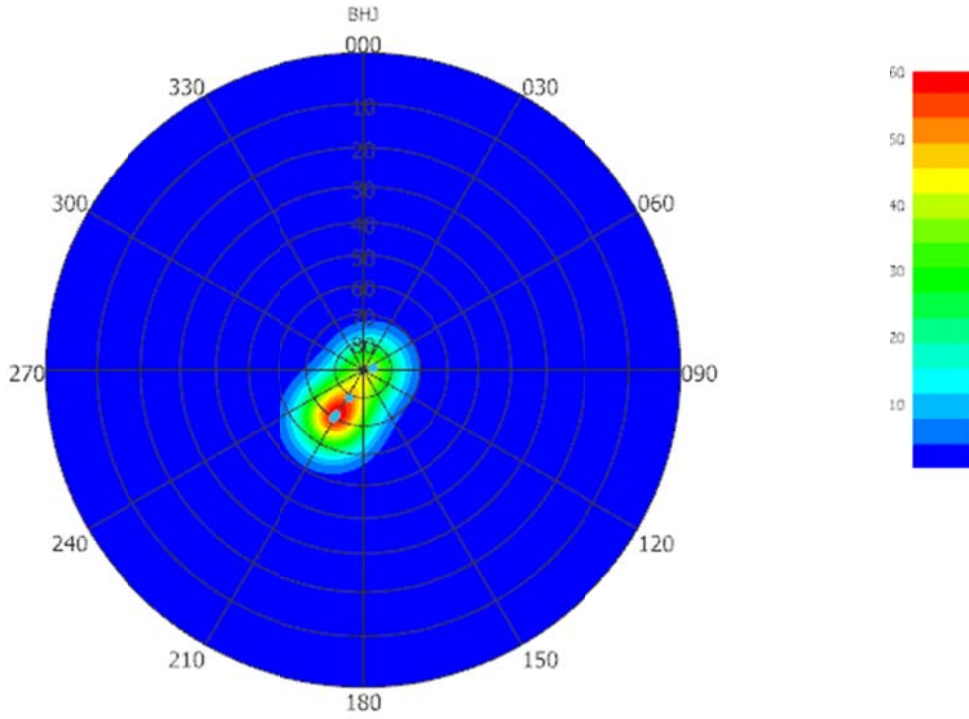
9.1   Conclusions

The kISMET team carried out a successful program of drilling and coring, and subsequent hydraulic fracturing for determining the stress field, understanding the effects of rock fabric on fracturing, and gaining experience in monitoring the fracturing process. The kISMET site was established in the West Access Drift of SURF on the 4850L. We drilled and cored five near-vertical boreholes in a line on 3 m (10 ft) spacing, deviating the two outermost boreholes to create a five-spot pattern around the test borehole centered in the test volume at a depth of ~1518 m (4980 ft). Laboratory measurements of core from the center test borehole showed P-wave velocity heterogeneity along each core indicate strong, fine-scale (~1 cm or smaller) changes in the mechanical properties of the rock, possibly due to the well-developed foliation. The load-displacement record suggests that the elastic stiffness is anisotropic, especially in samples from core where the rock appears stiffest when loaded parallel to the foliation. Tensile strength ranges between 3–7.5 MPa (435-1087 psi) and 5–12 MPa (725-1740 psi) depending on direction in the sample. Permeability measurements are planned, as are two types of laboratory hydraulic fracturing experiments to investigate the importance of rock fabric (anisotropy and heterogeneity) on near-borehole hydraulic fracture generation. Pre-fracturing numerical simulations with INL's FALCON code predicted fracture radius of 1.2 m (3.9 ft) for the planned fractures with a corresponding injection volume of 1.2 L, and negligible microseismicity. Field measurements of the stress field by hydraulic fracturing showed that the minimum horizontal stress at the kISMET site averages 21.7 MPa (3146 psi) pointing approximately N-S (356 degrees azimuth) and plunging slightly NNW at 12°. The vertical and horizontal maximum stress are similar in magnitude at 42-44 MPa for the depths of testing which averaged approximately 1530 m (5030 ft). Hydraulic fractures were remarkably uniform suggesting core-scale and larger rock fabric did not play a role in controlling fracture orientation. Monitoring using ERT and CASSM in the four monitoring boreholes, and passive seismic accelerometer-based measurements in the West Access Drift, were carried out during the long fracturing (stimulation) test. ERT was not able to detect the fracture created, while the accelerometers in the drift picked up the fracturing signal from the first (deepest) hydraulic-fracturing stress measurement. The CASSM data have not been analyzed yet. Analytical solutions suggest fracture radius of the generated fractures was more than 6 m (19.7 ft), depending on the unknown amount of leak-off. The kISMET results are consistent with large-scale mid-continent estimates of stress. Currently we are using the orientation of the stress field we determined to interpret large numbers of borehole breakouts recorded in nearby boreholes at SURF to generate a more complete picture of the stress field and its variations at SURF.

9.2   Research Needs

9.2.1   Characterization

The kISMET SubTER Sapling project was carried out on a small budget ($1.35M) over a very short period of time (~2 yrs). Over the course of the project, opportunities presented themselves for more boreholes, more monitoring points, more time to monitor, repeat experiments, etc. To keep to budget and schedule, we had to maintain a narrow focus on the project objectives. In this section, we discuss several additional experiments and expanded studies that could be carried out at the kISMET site as it has been developed to date.

First, although a 3D laser scan was carried out for the West Access Drift, acquisition of the data is not straightforward. Clearly, our future work at kISMET will budget for acquiring and using 3D laser scan data of the drift. Similarly, time and budget did not allow a detailed characterization of the structure (e.g.,

surface fractures) and lithology (including rock fabric and mineralogy) of the kISMET site in the vicinity of the drift. This information can be supplemented by petrographic descriptions and laboratory measurements of the core we have collected. Currently underway is a novel hyperspectral scanning procedure provided to us at no cost that will map minerals in a 15 ft (4.6 m) section of core. These studies will provide a definitive description of the phyllite that we have fractured and may help elucidate the variability in rock conductivity observed in the ERT scans.

9.2.2   Hydraulic Fracturing and Field Testing

Most of the hydraulic fracturing we carried out was for the purpose of determining the stress field. As such, the fractures did not have to be large, and in fact we wanted to avoid having fractures intersect the monitoring boreholes, which at some depths were within ~3 m (10 ft) or so of the test borehole. During the extended fracturing experiment (so-called stimulation test), we made a larger fracture possibly 6-8 m (10-26 ft) in radius. One obvious extension of kISMET testing that we would like to carry out is to keep propagating a fracture and observe the pressure and flow rate evolution, while monitoring it using CASSM and ERT (enhanced by use of saline fracturing fluid or conductive proppant).

We believe that kISMET fractures close following shut in. Future work at kISMET could inject proppant to prevent complete closure, and test permeability enhancement and sustainability by pressure-transient testing (e.g., push-pull hydrologic tests) following fracturing and propping.

Regarding CASSM sensitivity to detecting and characterizing induced fractures, which is an outstanding question because we have not yet processed the CASSM data, we note that we are working in another project on demonstrating theoretically that injections of CO_2 (or another gas) can be used to enhance active seismic and well-logging approaches to fault and fracture characterization (Oldenburg et al., 2016). This approach can be field-tested at kISMET (using air for reduced environmental concern) to validate our modeling predictions.

Our team responded to a FOA (No. 1445) with a research proposal that was not funded. We still view the proposed research as valuable for SubTER objectives. In this work we proposed to cross-validate the use of rock physics models combined with deformation observations, and geophysical monitoring for predicting, quantifying, and monitoring EGS heat exchanger development. This research would enhance the linkages between geophysically predicted heat exchanger development and actual hydraulic/thermal performance. The kISMET project has characterized the in situ stress of a small volume, a cube roughly 3 meters on a side and 40-meters deep below the 4850L. Small-scale fluid- injection stimulations can be used to evaluate stress changes within the formation by monitoring the acoustic and electrical resistivity response from boreholes 3 meters away. The proposed work included the addition of four new monitoring boreholes and a new set of field experiments designed to measure and test fracture permeability and interfacial area available for heat transfer before and after a stimulation event. A sketch of the experiment is shown in Fig. 9.1. The new boreholes extend the horizontal dimension of the cube to 9 meters and the depth to 75 meters. In the proposed project, we would add tiltmeter and seismometer monitoring to CASSM and ERT in order to characterize the hydraulic and thermal transfer properties of this reservoir volume both before and after simulation. The stimulations will include fluid injection at different flow rates and pressures and will also include fluids that are both hotter and colder than the formation. Separately, the brine content of the fluid will be varied with time to provide a tracer to track fracture growth using ERT tomography. Both before and after the stimulation, hydraulic characterization will use a variety of methods, including borehole flow logging, step drawdown tests, and Oscillatory Hydraulic Tomography (OHT) (Cardiff et al., 2013). Thermal heat transfer will likewise be assessed through a series of dipole flow tests across produced fractured intervals, because a prime goal of this project is to create a relation between the fluid-rock heat transfer coefficient and fracture morphology (or equivalently surface area). This extension to kISMET would advance the knowledge and technology of EGS heat exchanger

development by providing the data necessary to tightly link geophysical observations with hydraulic and thermal reservoir modifications in the near-field of an injection borehole.
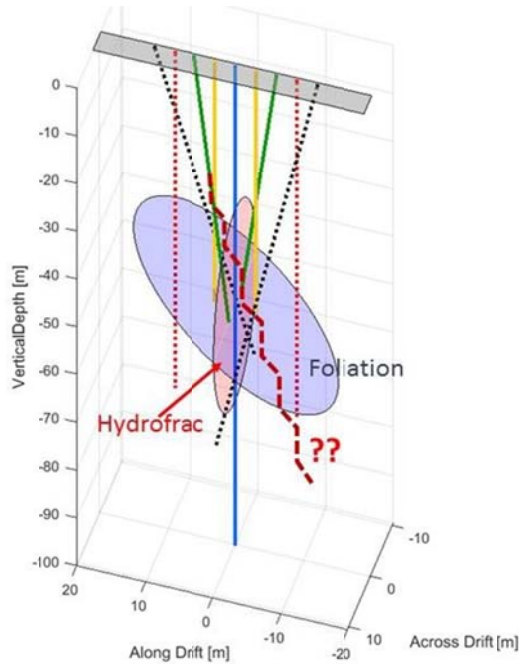

Figure 9.1. Sketch of four new boreholes (shown by dashed lines) proposed for kISMET to extend the test volume from 3 m cube to a 10 m cube.

9.2.3   Geophysical Monitoring

Before deploying CASSM and ERT again, we need to process the CASSM data and investigate through modeling and analysis the use of saline fracturing fluid or conductive tracers to enhance the ERT signal. Assuming feasibility is demonstrated by modeling, a repeat of the monitoring activity should be a priority and done in concert with testing to demonstrate near-real time ERT for adaptive control. This effort was shortchanged in the current kISMET sapling due to limited time in the field. Follow-on work needs to include testing ways to improve ERT. The kISMET ERT results suggest a few recommendations in order to enhance the possibility of fracture detection through mapping of electrical conductivity anomalies created by the fractures. First, the electrical conductivity between the fracture and the host rock needs to be enhanced. This can be achieved via the injection of a contrast agent/proppant/fluid with enhanced electrical conductivity that can leave a residue in the fracture even after fracture closes to ensure a sustained and maximized conductivity contrast. In addition, increase in the size of the fractures can help greatly to make fractures more detectable. We also note that more effective and targeted placement of the electrodes with respect to the fracture geometry could further enhance the chance of detection. This would include (1) for wells with casing, the placement of electrodes behind casing to eliminate the large impact from borehole fluids, (2) use of higher electrode density in the targeted fracture zone, and (3) aligning the electrode arrays better with presumed fracture planes. When open hole deployment is the only option, a better control of borehole fluid conductivity and isolation of electrical noise from co-deployed equipment (e.g., CASSM) are needed to reduce noise level and possible electrical cross-talk. If casing is an option, PVC casing with ERT electrodes grouted into the annulus could be used with CASSM in the borehole for electrical isolation of the CASSM system from the ERT system.

For better signal-to-noise in the passive seismic monitoring, we will test an alternative deployment in which accelerometers are placed in boreholes a few meters below the invert (floor). This will prevent much of the current noise in the drift from obscuring the fracturing signals.

9.2.4   Modeling Studies

The analytical and mechanistic modeling studies of hydraulic fracture initiation and growth for the kISMET project provided important guidance for designing stimulation experiments and monitoring plans, and to a large degree, also revealed the complexities of hydraulically propagating fractures in low-permeability crystalline rocks with heterogeneities spanning a wide range of scales. The predicted size (~1.2 m radius) of the initial opened crack from the pre-test simulations is very close to the size (~1.4 m radius) obtained from the post-test analytical calculations. We recommend follow-on modeling studies, in close integration with both laboratory and field experiments, with the ultimate goals of developing better understandings of underlying coupled physics governing fracturing processes in heterogeneous rocks, and developing 'robust' and 'high-fidelity' predictive models at various scales:

- Rigorous model calibrations using compression and tension tests of actual core samples from the site. We expect the models not only to reproduce the typical mechanical properties and pre/post-peak stress-strain behaviors, but also to reproduce realistic failure/fracturing patterns of rock samples that can be obtained directly or indirectly during experiments (e.g., high-resolution x-ray CT, acoustic emission, etc.). It is also worthy to use the fracture toughness (or fracture energy release rate) as the model calibration target too. The close integration between mechanistic modeling and laboratory core sample tests would enable us to better understand the effects of rock fabrics and anisotropy on fracture initiation and propagation under mechanics load.

- Close integration and comparison between laboratory-block hydraulic fracturing experiments and modeling approaches with various degrees of physics rigor. The samples of variable sizes would range from intact rocks and rocks with natural fractures from the site, to synthetically fabricated (e.g., 3D printing) brittle solids with various sizes of linear/planar defects (mimicking natural fractures with mineral fillings). Such tests with well-characterized block samples of different sizes of defects, in close integration with modeling, would significantly improve our fundamental understandings on how propagating fractures interact with natural fractures in low-permeability crystalline rocks and the dominant failure modes (tensile vs. shear) under given stress states, injection conditions (rate and viscosity), and characteristics of natural fractures (spacing, lengths, cohesive strength, residual permeability etc.).

- Perform post-test simulations for the actual kISMET stimulation test, using the re-calibrated model based on laboratory-test data, the new in situ stress measurements and exact injection history, and compare the simulated wellbore pressure with measured values. Another important task for post-test simulations is to compare the simulated fracturing process and spatial-temporal distributions of the seismic events and their statistics with the actual measurements during the stimulation. The close integration among the post-test simulations, field test and monitoring would allow us to better understand the limits and constraints of current predictive stimulation models, and more importantly, to what levels of details of rock heterogeneities and physics rigor of models would be needed in order to develop meaningful and robust stimulation models.

10. ACKNOWLEDGMENTS

This page left intentionally blank.

11. REFERENCES

Abé, H., Keer, L.M., and Mura, T. (1976). Growth rate of a penny-shaped crack in hydraulic fracturing of rocks, 2, J. Geophys. Res., 81(35), 6292–6298.

Ajo-Franklin, J., Daley, T., Butler-Veytia, B., Peterson, J., Wu, Y., Kelly, B., and Hubbard, S. (2011). Multi-level Continuous Active Source Seismic Monitoring (ML-CASSM): Mapping Shallow Hydrofracture Evolution at a TCE Contaminated Site. Society of Exploration Geophysics, 2011 SEG Annual Meeting, San Antonio, TX.

Atkinson, B. and Meredith, P. (1987). Experimental fracture mechanics data for rocks and minerals, in B. Atkinson ed, Fracture Mechanics of Rock, Academic Press, p. 477-526

Bredehoeft, J.D., Wolff, R.G., Keys, W.S., and Shuter, E. (1976). Hydraulic fracturing to determine the regional in situ stress field, Piceance Basin, Colorado. Geological Society of America Bulletin, 87(2), pp.250-258.

Bunger, P., Lakirouhani, A., and Detournay, E. (2010). Modelling the effect of injection system compressibility and viscous fluid flow on hydraulic fracture breakdown pressure, Rock Stress and Earthquakes (edited by F. Xie), CRC Press, pp. 59-67.

Caddey, S.W., Bachman, R.L., Campbell, T.J., Reid, R.R., and Otto, R.P. (1991). The Homestake Gold Mine: an early Proterozoic iron-formation-hosted gold deposit, Lawrence County, South Dakota. US Geological Survey Bulletin 1857-J, 67 pp.

Cardiff, M., Bakhos, T., Kitanidis, P.K., and Barrash, W. (2013). Aquifer heterogeneity characterization with oscillatory pumping: Sensitivity analysis and imaging potential. Water Resources Research, 49(9), pp.5395-5410.

Carslaw, H.S. and Jaeger, J.C. (1959). Conduction of heat in solids. Oxford: Clarendon Press, 1959, 2nd ed.

Carter, T.G., Otto, S.A., Carvalho, J.L., Popielak, R., Vardiman, D., and Hladysz, Z. (2011). Preliminary design of the 4850-level excavations at DUSEL Part 1 – Geological engineering evaluation of rock mass conditions. American Rock Mechanics Association, 45th US Rock Mechanics / Geomechanics Symposium, ARMA 11-482, 8 p.

Dahi-Taleghani, A. and Olson, J. (2011). Numerical Modeling of Multistranded-Hydraulic-Fracture Propagation: Accounting for the Interaction Between Induced and Natural Fractures. SPE J 16:575–581. doi: 10.2118/124884-PA

Doe, T.W. and Korbin, G. (1987). A comparison of hydraulic fracturing and hydraulic jacking stress measurements, Proceedings of the 28th US Rock Mechanics Symposium, Tucson Arizona., p. 283-290.

Dusseault, M.B. (2011). Geomechanical challenges in petroleum reservoir exploitation. KSCE Journal of Civil Engineering, 15(4), 669-678.

Ebenhack, J.F. (2013). Characterization of the hydrogeology and stress state in the vicinity of the Homestake Mine, Lead, SD. M.S. Thesis, Clemson University, 159 p.

Economides, M.J. and Nolte, K.G. (2000). Reservoir Stimulation, 3rd Edition. Wiley

Finsterle, S. and Persoff, P. (1997). Determining permeability of tight rock samples using inverse modeling. Water Resources Research, 33(8), 1803-1811. doi:10.1029/97wr01200

Gage, J.R., Wang, H.F., Fratta, D., and Turner, A.L. (2014). In situ measurements of rock mass deformability using fiber Bragg grating strain gauges. International Journal of Rock Mechanics and Mining Sciences, 71, 350-361.

Girard, J.M., McKibbin, R.W., Seymour, J.B., and Jones, F.M. (1997). Characterization of in situ stress conditions at depth – Homestake Mine, Lead, South Dakota. International Journal of Rock Mechanics and Mining Sciences, 34 (3-4), paper 104.

Golder Assoc. (2010). In situ Stress Measurement Deep Underground Science and Engineering Laboratory. Prepared for South Dakota School of Mines and Technology, January 8, 2010. Lakewood, CO: Golder.

Grant, M.A. and Garg, S.K. (2012). Recovery factor for EGS. In Proceedings of the 37th Workshop on Geothermal Reservoir Engineering, Stanford University, Stanford, California, USA (pp. 738-740).

Haimson, B.C. (1978). The hydraulic fracturing stress measurement method and recent results, Int. Jour. Rock Mech, v. 15, pp 167-176.

Haimson, B.C. and Cornet, F.H. (2003). ISRM Suggested Method for Rock Stress Estimation: Hydraulic Fracturing and Hydraulic Testing of Pre-Existing Fractures, Intl. J. Rock Mech. and Mining Sci., 40, 1011-1020.

Haimson, B.C. and Lee, M.Y. (1992). Hydraulic fracturing tests in the Quimby Granite, and the state of stress in the western midcontinent (abstract), Eos Tran& AGU, 73(43), Fall Meet. Suppl., 559, 1992.

Harms, J., Acernese, F., Barone, F., Bartos, I., Beker, M., van den Brand, J.F., Christensen, N., Coughlin, M., DeSalvo, R., Dorsher, S., Heise, J., Kandhasamy, S., Mandik, V., Márka, S., Mueller, G., Naticchioni, L., O'Keefe, T., Rabeling, D.S., Sajeva, A., Trancynger, T., and Wand, V. (2010). Characterization of the seismic environment at the Sanford Underground Laboratory, South Dakota. Classical and Quantum Gravity, 27, 22 p.

Hart, K., Trancynger, T.C., Roggenthen, W., and Heise, J. (2014). Distribution modeling in support of physics experiments at the Sanford Underground Research Facility (SURF). Proceedings of the South Dakota Academy of Science, 93, 33-41.

Hayashi, K. and Haimson, B. (1991). Characteristics of shot-in occurs in hydraulic fracturing stress measurements and determination of in situ minimum compressive stress, Journal of Geophysical Research, 96, 18,311-18,321

Hazzard, J.F. and Young, R.P. (2002). Moment tensors and micromechanical models. Tectonophysics 356:181–197. doi: 10.1016/S0040-1951(02)00384-0

Heise, J. (2015). The Sanford Underground Research Facility at Homestake, Journal of Physics: Conference Series. Vol. 606. No. 1, IOP Publishing.

Hladysz, Z. and Erickson, D.J. (1984). Mechanical Properties of Rocks From the Homestake Mine, prepared by Department of Mining Engineering, South Dakota School of Mines & Technology, Rapid City, SD, for the Homestake Mining Company, San Francisco, CA.

Huang, H. and Mattson, E. (2014). Physics-based Modeling of Hydraulic Fracture Propagation And Permeability Evolution of Fracture Network In Shale Gas Formation. In: 2014 ARMA 48th US Rock Mechanics/Geomechanics Symposium,Minneapolis, MN, 1-4 June 2014.

JASON Report, Subsurface Characterization Report, JSR-14-Task-013, Dan McMorrow (contact), September 15, 2014.

Lee, M.Y. and Haimson, B.C. (1989). Statistical evaluation of hydraulic fracturing stress measurement parameters, Int. J. Rock Mech. Min. Sci. & Geomech. Abstr., 26, no.6, 447-456.

Lucier, A.M., Zoback, M.D., Heesakkers, V., Reches, Z., and Murphy, S.K. (2009). Constraining the far-field in situ stress state near a deep South African gold mine, International Journal of Rock Mechanics, doi:10.1016/j.ijrmms.2008.09.005.

Mellegard, K.D., Loken, M.C., and Keffeler, E.R. (2010). Laboratory Testing of Amphibolite and Rhyolite from the 4850 Level of the DUSEL Facility. Prepared for South Dakota School of Mines and Technology, February 2010. (RESPEC Topical Report RSI-2100).

Morrow, C., Lockner, D., Hickman, S., Rusanov, M., and Röckel, T. (1994). Effects of lithology and depth on the permeability of core samples from the Kola and KTB drill holes, J. Geophys. Res., 99(B4), 7263–7274, doi: 10.1029/93JB03458.

Murdoch, L.C., Germanovich, L.N., Wang, H., Onstott., T.C., Elsworth, D., Stetler, L., and Boutt, D. (2012). Hydrogeology of the vicinity of Homestake mine, South Dakota, USA. Hydrogeology Journal, 20, 27-43.

Nasseri, M.H., Rao, K.S., and Ramamurthy, T. (1997). Failure mechanism in schistose rocks. International Journal of Rock Mechanics and Mining Sciences, 34(3), 219-e1.

Nolte, K.G. (1986). A general analysis of fracture pressure decline with application to three models, SPE Formation Evaluation, 1, p. 571-583

Oldenburg, C.M., Doughty, C., Peters, C.A., and Dobson, P.F. (2012). Simulations of long-column flow experiments related to geologic carbon sequestration: Effects of outer wall boundary condition on upward flow and formation of liquid CO_2, Greenhouse Gases: Sci. and Tech., 2(4), 279–303.

Oldenburg, C.M., Daley, T.M., Borgia, A., Zhang, R., Doughty, C., Ramakrishnan, T.S., Altundas, B. and Chugunov, N. (2016). Preliminary Simulations of Carbon Dioxide Injection and Geophysical Monitoring to Improve Imaging and Characterization of Faults and Fractures at EGS Sites, Stanford Geothermal Workshop, Stanford, CA, Feb. 22-24, 2016.

Pariseau, W.G. (1986). Research Study on Pillar Design for Vertical Crater Retreat (VCR) Mining (contract JO215043, Univ. of Utah). USBM OFR 44-86, NTIS PB86-210960, 232 pp.

Potyondy, D.O. and Cundall, P.A. (2004). A bonded-particle model for rock. Int J Rock Mech Min Sci 41:1329–1364. doi: 10.1016/j.ijrmms.2004.09.011

Rahn, P.H. (1994). Hydraulic fracturing a water well in the Precambrian rocks of the Black Hills. Proceedings of the South Dakota Academy of Science, 73, 205-210.

Robinson, J., Slater, L., Johnson, T., and Binley, A. (2013). Strategies for characterization of fractured rock using cross-borehole electrical tomography.The Leading Edge: 32, no. 7, 784–790.

Roggenthen, W.M. and Koch, C.D. (2013). Geophysical logging of DUSEL core and geotechnical applications. American Rock Mechanics Association, 47th US Rock Mechanics / Geomechanics Symposium, ARMA 13-493, 8 p.

Rummel, F. (1987). Fracture mechanics approach to hydraulic fracturing stress measurements. in Fracture Mechanics of Rock, ed. B. K. Atkinson, Academic Press, London, 217-240.

Rutqvist, J., Tsang, C., and Stephansson, O. (2000). Uncertainty in the maximum principal stress estimated from hydraulic fracturing measurements due to the presence of the induced fracture, Int. J. Rock Mech. Min. Sci. & Geomech. Abstr., 37, 107-120.

Song, I., Elphick, S.C., Main, I.G., Ngwenya, B.T., Odling, N.W., and Smyth, N.F. (2004). One-dimensional fluid diffusion induced by constant-rate flow injection: Theoretical analysis and application to the determination of fluid permeability and specific storage of a cored rock sample, J. Geophys. Res., 109, B05207, doi: 10.1029/2003JB002395

Suarez-Rivera, R., Burghardt, J., Stanchits, S., Edelman, E., and Surdi, A. (2013). Understanding the effect of rock fabric on fracture complexity for improving completion design and well performance. In IPTC 2013: International Petroleum Technology Conference.

Takahashi, H. and Abé, H. (1987). Fracture mechanics applied to hot, dry rock geothermal energy, in B. Atkinson ed, Fracture Mechanics of Rock, Academic Press, p 241-276

Vigilante, P. (2016). Critical Review of Laboratory Rock Properties and State of Stress in the Sanford Underground Research Laboratory (SURF).

Wang, H.F., Blair, S.C., Carson, S.R., Martel, S.J., and Tokunaga, T. (2007). Investigating coupled mechanical-hydrological behavior in a DUSEL. In: Rock Mechanics: Meeting Society's Challenges and Demands, Vol. 2 – Case Histories, E. Eberhardt, D. Stead, and T. Morrison, eds., Taylor and Francis, pp. 1115-1122.

Wang, H., Doe, T., and Zoback, M. (2012). "Stress heterogeneity at 1.5 km depth in the former Homestake Gold Mine, Lead, South Dakota," unpublished proposal.

Wang, Q. and Xing, L. (1999). Determination of fracture toughness KIC by using the flattened Brazilian disk specimen for rocks. Engineering Fracture Mechanics, 63, 193-201.

Warpinski, N.R., Mayerhofer, M.J., Vincent, M.C., Cipolla, C.L., and Lolon, E.P. (2009). Stimulating unconventional reservoirs: maximizing network growth while optimizing fracture conductivity. Journal of Canadian Petroleum Technology, 48(10), 39.

Wu, K., and Olson, J.E. (2013). Investigation of the Impact of Fracture Spacing and Fluid Properties for Interfering Simultaneously or Sequentially Generated Hydraulic Fractures. In: SPE 163821 Hydraulic Fracturing Technology Conference, Woodlands, Texas, USA, 6-8 February.

Xu, W., Thiercelin, M., Ganguly, U., et al. (2010). Wiremesh: A Novel Shale Fracturing Simulator Models. In: International Oil and Gas Conference and Exhibition in China, 8-10 June, Beijing.

Yew, C.H. (1997). Mechanics of Hydraulic Fracturing. Gulf Publishing Company, Houston, Texas

Zang, A., Oye, V., Jousset, P., Deichmann, N., Gritto, R., McGarr, A., Majer, E., & Bruhn, D. (2014) Analysis of induced seismicity in geothermal reservoirs – An overview. Geothermics, 52, 6-21.

Zhou, J., Huang, H., and Deo, M. (2015). A New Physics-Based Modeling of Multiple Non-Planar Hydraulic Fractures Propagation. In: URTeC 2170875. Unconventional Resources Technology Conference held in San Antonio, Texas, USA, 20-22 July.

Zhou, Q., Oldenburg, C.M., Spangler, L.H., and Birkholzer, J.T., Approximate Solutions for Diffusive Fracture-Matrix Transfer: Application, Water Resour. Res., submitted.

Zoback, M.L. and Zoback, M.D. (1989). Tectonic stress field of the continental United States, Geological Society of America Memoir 172, Chapter 24, 523-540.

Zoback, M.D., Barton, C.A., Brudy, M., Castillo, D.A., Finkbeiner, T., Grollimund, B.R., Moos, D.B., Peska, P., Ward, C.D., and Wiprut, D.J. (2003). Determination of stress orientation and magnitude in deep wells. International Journal of Rock Mechanics and Mining Sciences, 40(7), pp.1049-1076.

Zoback, M.D. (2007). Reservoir Geomechanics, Cambridge University Press 448 p.